# International Design Study for the Neutrino Factory

IDS-NF-017

## First progress report

*The IDS-NF collaboration*

**Abstract**

The International Design Study for the Neutrino Factory (the IDS-NF) collaboration has been established by the Neutrino Factory community to deliver a Reference Design Report (RDR) for the facility by 2012/13. This, the first progress report, summarises the status of the study in early 2010. The baseline design for the facility will provide $10^{21}$ muon decays per year from 25 GeV stored muon beams. The facility will serve two neutrino detectors; one situated at source-detector distance of between 3 000 km and 5 000 km, the second at 7 000–8 000 km. The work of the IDS-NF is carried out in three working groups: the Physics and Performance Evaluation Group; the Accelerator Working Group; and the Detector Working Group. The status of the work of each of these working groups is summarised in the report. In addition to developing the baseline configuration, the IDS-NF is active in exploring alternative configurations that may offer performance or cost advantages or may lower the technical risk of particular sub-systems. The Low Energy Neutrino Factory, in which a 4–5 GeV muon beam matched to a source-detector distance of $\sim$ 1500 km, which is discussed in the report, has emerged as a potentially attractive option should $\theta_{13}$ be large ($\sin^2 2\theta_{13} > 0.01$).

16$^{\text{th}}$ April 2010

S. Choubey, R. Gandhi, S. Goswami
*Harish-Chandra Research Institute, Chhatnag Road, Jhunsi, Allahabad, 211019, India*

J.S. Berg, J.C. Gallardo, H. Kirk, N. Simos, T. Tsang
*Brookhaven National Lab, P.O. Box 5000, Upton, NY 11973-5000, USA*

M. Ellis, P. Kyberd
*Brunel Universiry West London, Uxbridge, Middlesex UB8 3PH, UK*

M. Aiba, E. Benedetto, I. Efthymiopoulos, R. Garoby, K. Hanke, M. Martini, G. Prior
*European Organization for Nuclear Research, CERN CH-1211, Geneva 23, Switzerland*

T. Li, S. Pascoli
*Institute for Particle Physics Phenomenology, Department of Physics, University of Durham, Science Laboratories, South Rd, Durham, DH1 3LE, UK*

C. Walter
*Duke University, Department of Physics, Durham, NC 27706, USA*

A. Bross, S. Geer, J. Morfin, D. Neuffer, M. Popovic, C. Johnstone
*Fermilab, P.O. Box 500, Batavia, IL 60510-5011, US*

A. Blondel, F. Dufour
*University de Geneve, 24, Quai Ernest-Ansermet, 1211 Geneva 4, Suisse*

A. Laing, P. Soler
*Department of Physics and Astronomy, Kelvin Building, University of Glasgow, Glasgow G12 8QQ, Scotland, UK*

G. de Lellis
*Istituto Nazionale di Fisica Nucleare, Laboratorio Nazionale del Gran Sasso, Strada Statale 17/bis Km 18+910, I-67010 Assergi (L'Aquila), Italy*

F. Meot
*Laboratory for Subatomic Physics and Cosmology (LPSC), Universite Joseph Fourier (Grenoble 1), 53, ave. des Marthyrs, F-38026 Grenoble CEDEX, France*

J. Kopp, M. Lindner, T. Schwetz
*Max-Planck-Institut fr Kernphysik, PO Box 103980, 69029 Heidelberg, Germany*

T. Enqvist, P. Kuusiniemi
*CUPP, University of Oulu, Pyhäsalmi, Finland*

J. Peltoniemi
*Neutrinica Ltd, Oulu, Finland*

D. Kaplan
*Illinois Institute of Technology, 3300 South Federal Street, Chicago, IL 60616-3793, US*

A. Alekou, M. Apollonio, M. Aslaninejad, C. Bontoiu, P. Dornan, A. Kurup, K. Long, J. Pasternak, J. Pozimski
*Physics Deptartment, Blackett Laboratory, Imperial College London, Exhibition Road, London, SW7 2AZ, UK*

A. Bogacz
*Jefferson Laboratory, 12000 Jefferson Avenue, Newport News, VA 23606, US*

S. Bhattacharya, D. Majumdar
*Saha Inst. Nuclear Phys., Sector-I, Block-AF, bidhannagar, Kolkata 700064, India*

Y. Mori
*Kyoto University, Research Reactor Institute, 2,Asashiro-Nishi, Kumatori-cho, Sennan-gun, Osaka 590-0494 JAPAN*

R. Seviour
*Physics Department, Lancaster University, Lancaster, LA1 4YB, UK*

M. Zisman
*Lawrence Berkeley National Laboratory, 1 Cyclotron Road, Berkeley, CA 94720, US*

M. Mezzetto
*Lab Nazionali di Legnaro-INFN, Via Romea, 4, I-35020 Legnaro, Padova, Italy*

A. Donini, M. Maltoni, S. Rigolin
*Instituto de Fisica Teorica UAM/CSIC, Facultad de Ciencias C-XVI, Universidad Autonoma de Madrid, Cantoblanco, 28049 Madrid, Spain*

D. Stratakis
*University of Maryland, Dept. of Physics and Astronomy, Physics Building (Bldg. 082), College Park, MD 20742-4111, US*

C. Bromberg
*Michigan State University, 150 Administration Building, East Lansing, Michigan 48824, US*

M. Bonesini, P. Negri, S. Ragazzi
*Sezione INFN Milano Bicocca, Dipartimento di Fisica G. Occhialini, Piazza Scienza 3, 20126 Milano, Italy*

T. Hart
*The University of Mississippi, Department of Physics and Astronomy, 108 Lewis Hall, PO Box 1848, Oxford, Mississippi 38677-1848, US*

Y. Kudenko
*Inst. for Nuclear Research of Russian, Academy of Sciences, 7a, 60th October Anniversary prospect, Moscow 117312, Russia*

P. Gorbounov
*Institute of Theoretical and Experimental, Physics, B. Cheremushkinskaya ul. 25, RU-117218 Moscow, Russia*

N. Mondal
*Tata Inst. of Fundamental Research, School of Natural Sciences, Homi Bhabha Rd., Mumbai 400005, India*

M. Blennow, E. Fernandez-Martinez
*Max Planck Inst. fur Phys., Werner Heisenberg Inst. fur Phys., Fohringer Ring 6, D-80805 Munich, Germany*

R.J. Abrams, C.M. Ankenbrandt, M.A.C. Cummings, G. Flanagan, M/ Neubauer, R.P. Johnson, C.Y. Yoshikawa.
*Muons Incorporated, 552 N. Batavia Avenue, Batavia, IL 60510, US*

V. Palladino
*Universita di Napoli Federico II, Dipartimento di Scienze Fisiche, Complesso Universitario di Monte S. Angelo, via Cintia, I-80126 Napoli, Italy*

A. de Gouvea
*Northwestern University, Dept. of Physics and Astronomy, 2145 Sheridan Road, Evanston, Illinois 60208-3112 US*

Y. Kuno
*Osaka University, Graduate School / School of Science, 1-1 Machikaneyama-cho, Toyonaka, Osaka 560-0043, Japan Graduate School of Science, Department of Physics, Osaka University, Toyonaka, Osaka, Japan*

V. Blackmore, J. Cobb, W. Lau
*Particle Physics Departmenet, The Denys Wilkinson Building, Keble Road, Oxford, OX1 3RH, UK*

K. McDonald
*Princeton University, Princeton, NJ, 08544, US*

G. Hanson, P. Snopok
*Department of Physics and Astronomy, University of California, Riverside, CA 92521, US*

K. McFarland
*University of Rochester, Dept. of Physics and Astronomy, Bausch and Lomb Hall, P.O. Box 270171, 600 Wilson Boulevard, Rochester, NY 14627-0171 US*

L. Tortora
*Universita' degli Studi di "Roma Tr", Dipartimento di Fisica "Edoardo Amaldi", Istituto Nazionale di Fisica Nucleare, Via della Vasca Navale 84, 00146 Roma, Italy*

C. Andreopoulos, R. Bennett, S. Brooks, O. Caretta, T. Davenne, C. Densham, R. Edgecock, S. Gray, D. Kelliher, P. Loveridge, A. McFarland, S. Machida, C. Prior, G. Rees, C. Rogers
*STFC Rutherford Appleton Laboratory, Chilton, Didcot, Oxfordshire, OX11 0QX, UK*

C. Booth, G. Skoro, N. Spooner
*University of Sheffield, Dept. of Physics and Astronomy, Hicks Bldg., Sheffield S3 7RH, UK*

Y. Karadzhov, R. Tsenov
*Department of Atomic Physics, St. Kliment Ohridski University of Sofia, 5 James Bourchier Boulevard, BG-1164 Sofia, Bulgaria*

S. King
*School of Physics and Astronomy, University of Southampton, Highfield, Southampton, SO17 1BJ, UK*

C.Bobeth, M. Dracos, F. Osswald
*Institut de Recherches Subatomiques, 23 Rue du Loess, BP28-F67037, Strasbourg, France*

A. Cervera-Villanueva, P. Hernandez
*Instituto de Fisica Corpuscular (IFIC), Centro Mixto CSIC-UVEG, Edificio Investigacion Paterna, Apartado 22085, 46071 Valencia, Spain*

S.K. Argarwalla, P. Huber
*Virginia Polytechnic Inst. and State Univ., Physics Dept., Blacksburg, VA 24061-0435*

J. Back, P. Harrison, B. Morgan,
*Department of Physics, University of Warwick, Coventry, CV4 7AL, UK*

J.T. Sobczyk
*Institute of Theoretical Physics, University of Wroclaw, pl. M. Borna 9,50-204, Wroclaw, Poland*

D. Meloni, J. Tang, W. Winter
*Fakultät f¨r Physik und Astronomie, Am Hubland, 97074 Würzburg, Germany*

S. Menary
*128 Petrie Science and Engineering Building, York University, 4700 Keele St., Toronto, Ontario, M3J 1P3, Canada*

# Contents

**1 Introduction** **1**

**2 Physics and Performance Evaluation Group** **2**

2.1 Current status of global neutrino data . . . . . 3

2.2 The baseline Neutrino Factory . . . . . 6

2.2.1 Tau production in the disappearance channel . . . . . 6

2.2.2 Near detectors at the Neutrino Factory . . . . . 10

2.2.3 Physics case for tau detection at the intermediate baseline . . . . . 17

2.2.4 Impact of systematics and location of detectors . . . . . 25

2.3 Neutrino Factory in stages? . . . . . 26

2.3.1 Large $\boldsymbol{\theta_{13}}$ ($\theta_{13}$ discovered by next generation of experiments) . . . . . 27

2.3.2 Small $\boldsymbol{\theta_{13}}$ ($\theta_{13}$ not discovered by the next generation of experiments) . . . . . 27

2.4 LENF . . . . . 28

2.5 Theory of neutrino masses and mixings . . . . . 32

2.5.1 Connection to charged leptons flavour violation . . . . . 32

2.5.2 Summary of the NuFlavour 09 workshop . . . . . 34

**3 Accelerator Working Group** **40**

3.1 Overview . . . . . 40

3.2 Proton driver . . . . . 41

3.3 Target station . . . . . 42

3.3.1 Status . . . . . 42

3.3.2 Work in progress . . . . . 43

3.3.3 Alternative approaches . . . . . 43

3.4 Muon front end . . . . . 43

3.4.1 Baseline optimisation . . . . . 44

3.4.2 Alternative Technologies . . . . . 44

3.4.3 Other Options . . . 46
3.5 Muon acceleration . . . 46
3.5.1 Muon linac and RLAs . . . 46
3.5.2 Muon RLA complex . . . 46
3.5.3 Scaling FFAG as an alternative to the RLAs . . . 57
3.5.4 Muon Beam Acceleration . . . 57
3.5.5 Muon FFAG . . . 60
3.6 Storage Ring . . . 63
3.6.1 Optical Parameters and Working Point . . . 64
3.6.2 Particle Tracking and Dynamic Aperture . . . 65
3.6.3 Decay Rings Diagnostics . . . 66

**4 Detector Working Group** **70**
4.1 Overview . . . 70
4.2 Magnetised Iron Neutrino Detector . . . 71
4.2.1 Introduction . . . 71
4.2.2 MIND parameterisation and expected event yields . . . 72
4.2.3 Reconstruction tools . . . 73
4.2.4 Analysis tools and cuts . . . 76
4.2.5 Analysis Results . . . 79
4.2.6 Conclusions . . . 85
4.3 Totally Active Scintillator Detector . . . 86
4.4 Liquid Argon Detector . . . 91
4.4.1 Introduction . . . 91
4.4.2 Europe and Japan . . . 91
4.4.3 North America . . . 94
4.5 Near detector . . . 95
4.5.1 Beam simulation and flux measurement at the near detector . . . 95
4.5.2 Plans for 2010 . . . 97

# 1 Introduction

The phenomenon of neutrino oscillations has been established through measurements of electron neutrinos produced in the sun (solar neutrinos), neutrinos produced in the bombardment of the upper atmosphere by cosmic rays (atmospheric neutrinos), electron anti-neutrinos produced in nuclear reactors, and using beams of neutrinos produced by particle accelerators [1]. The matrix by which the neutrino mass basis is rotated into the neutrino flavour basis is usually parameterised in terms of three mixing angles ($\theta_{12}$, $\theta_{23}$, and $\theta_{13}$) and one phase parameter ($\delta$) [2]. If $\delta$ is non-zero, then CP violation will occur via the neutrino mixing matrix. Measurements of neutrino oscillations are not sensitive to the neutrino masses themselves, but may be used to determine the mass-squared differences $\Delta m^2_{31} = m^2_3 - m^2_1$ and $\Delta m^2_{21} = m^2_2 - m^2_1$. The challenge to the neutrino community is to measure all the mixing angles as precisely as possible, to determine the sign of $\Delta m^2_{31}$, to measure $\Delta m^2_{21}$ and $\Delta m^2_{31}$ precisely, and, by measuring $\delta$, to discover leptonic-CP violation if it occurs. Precision measurements of the parameters that govern neutrino oscillations are essential if a complete understanding of the nature of the neutrino is to be obtained. Since the ultimate theory must unify the treatment of quarks and leptons, the goal must be to measure the neutrino-mixing parameters with an uncertainty that matches the precision with which the quark-mixing parameters are known. Such measurements will either establish the minimal model outlined above or, by establishing parameter sets inconsistent with it, point to the existence of entirely new phenomena.

The Neutrino Factory, in which an intense, high-energy neutrino beam is produced from the decay of stored muon beams, has been proposed to serve a programme of precision measurements of neutrino oscillations [3]. The Neutrino Factory has been shown to out-perform second-generation super-beam and beta-beam facilities [4]. The International Design Study for the Neutrino Factory (the IDS-NF) [5] has been established by the Neutrino Factory community to deliver the Reference Design Report (RDR) for the facility, in time for the 2012/13 decision point identified by the Strategy Session of CERN Council [6]. The RDR will include [7]: the physics performance of the Neutrino Factory and the specification of each of the accelerator, diagnostic, and detector systems; the cost of the facility; and an estimate of the schedule for its implementation. The RDR will also include a discussion of the remaining technical uncertainties and an appropriate uncertainty-mitigation plan. As a step on the way, the IDS-NF collaboration will prepare an Interim Design Report (IDR) towards the end of 2010. The IDR marks the point at which the focus of the IDS-NF effort turns to the engineering studies required to deliver the RDR; it documents the baseline for the accelerator complex, the neutrino detectors, and the instrumentation systems.

The potential of muon accelerators for particle physics is outstanding, not only providing the tool of choice for the study of neutrino oscillations but also providing a means by which searches for cLFV of exquisite sensitivity can be made as well as a route to the energy frontier in lepton-antilepton collisions at the Muon Collider. The IDS-NF collaboration is conscious of this far-reaching programme and will seek to address the broad muon-physics case and to identify the synergies between the accelerator facilities required for the Neutrino Factory and

the Muon Collider in the IDR and the RDR.

The work of the IDS-NF is carried out in three working groups: the Physics and Performance Evaluation Group; the Accelerator Working Group; and the Detector Working Group. This, the first progress report of the IDS-NF, summarises the status of the work of each of the working groups early in 2010. At the time of writing, plans are being laid for the preparation of the IDR, including a first evaluation of teh cost of the IDS-NF baseline for the facility.

## 2 Physics and Performance Evaluation Group

The work performed by the Physics and Performance Evaluation Group (PPEG) is summarised in this section. One focus of the work has been to develop a better understanding of the strengths and limitations of the IDS-NF baseline setup. In this context a large effort went into providing supporting results and documentation for reviews of the IDS-NF baseline which have been carried out at the plenary IDS-NF meetings. In particular, the detection of the silver ($\tau$-apperance) channel is important in the search for non-standard interactions and in the efforts to establish whether the neutrino-mixing matrix is unitary. The PPEG group evaluated the effectiveness of the Magnetised Emulsion Cloud Chamber (MECC), which was included in the specification of the intermediate detector system. The results of this study (section 2.2.3) indicate that the statistical weight of the MECC as presently defined does not give a significant impact on the determination of the standard oscillation parameters. In order to maintain the capability of including a $\nu_\tau$-detector at the intermediate, and possibly the long, baseline, the IDR will carry the cost of sizing the cavern (or caverns) such that a $\nu$-detector can be implemented [8]. The PPEG also started to look into the requirements of the near-detector systems, how they can be used to reduce the systematic uncertaintiies, and their possible benefits for systematics, but also for their discovery potential new physics (see section 2.2.2). An interesting issue, which so far has been mentioned only in passing, is the effect of $\tau$-appearance and subsequent leptonic $\tau$-decays on precision studies of the $\nu_\mu$ disappearance channel. Interestingly, one of the main systematic uncertainties may stem from the $\nu_\tau$ charged-current cross section which is not very well known (see section 2.2.1). A Low Energy Neutrino Factory (LENF) has become an attractive option. New results on the physics performance for standard and non-standard physics were evaluated (see section 2.4) based on updated results on the performance of the Totally Active Scintillator Detector (TASD) which were provided by the Detector Working Group. A study of possible staging scenarios, in which the LENF was the first step in the development of the baseline Neutrino Factory complex was performed (see section 2.3).

The connection to charged-lepton flavour violations (cLFV) is obvious from both the experimental point of view (a Neutrino Factory will provide enormous muon fluxes) and from a theoretical point of view, since in many cases the physics which is responsible for neutrino masses also generates cLFV. The theory connection is explored in section 2.5.1. Furthermore, PPEG maintained and strengthened its interactions with the theory community by hosting a workshop, entitled NuFlavour 09, at the Cosener's House, Abingdon, UK [9]. This workshop was

a great success and helped us develop a better understanding of the role of neutrino physics in the wider context of particle physics. A summary of this workshop is provided in section 2.5.2.

## 2.1 Current status of global neutrino data

Neutrino physics has seen an unprecedented wealth of experimental data over the last decade. The global analysis of this data allows a rather surprising picture to be drawn in which two mixing angles are large, one of which may possibly be maximal, and the third being small; of the order of the Cabbibo angle or less. At the same time, the mass splittings between neutrinos show a less pronounced hierarchy than is observed in the quark sector. These unexpected differences between the neutrino and the quark sectors are one of the main motivations for new, precise experiments to measure neutrino oscillations. Before discussing these future experiments, we would like to present the status quo.

Thanks to the synergy amongst a variety of experiments involving solar and atmospheric neutrinos and 'man-made' neutrinos produced in nuclear power plants and using accelerators, we now have a relatively detailed picture of the parameters describing three–flavour neutrino oscillations. Table 1 summarises the results of two recent global fits to world neutrino data from [1] (recently updated arXiv version 3) and [10]. Details of another recent analysis can be found in [11, 12]. Both analyses considered here include the latest data release from the KamLAND reactor experiment [13] of a total exposure of 2881 ton·yr. Spectral information from KamLAND data leads to an accurate determination of $\Delta m^2_{21}$ with the remarkable precision of 8% at $3\sigma$, defined as $(x^{\rm upper} - x^{\rm lower})/(x^{\rm upper} + x^{\rm lower})$. KamLAND data also start to contribute to the lower bound on $\sin^2\theta_{12}$, whereas the upper bound is dominated by solar data. The data from the last phase of the Sudbury Neutrino Observatory (SNO), in which neutrons produced in the neutral current (NC) neutrino interaction with deuterium are detected principly by an array of $^3$He NC detectors (NCD) [14], as well as the recent joint re-analysis of data from SNO Phase I and Phase II (the pure $D_2O$ and salt phases) [15]. In this analysis, an effective electron kinetic energy threshold of 3.5 MeV has been used (Low Energy Threshold Analysis, LETA), and the determination of the total neutrino flux has been improved by about a factor two. These improvements have been possible mainly because the energy thresholds used in the previous analysis (5 MeV for the Phase I analysis and 5.5 MeV for Phase II) have been reduced resulting a NC event sample in the LETA that is increased by about 70%. Furthermore, energy resolution, background suppression, and systematic uncertainties have all been improved. Data from SNO are combined with the global data on solar neutrinos [16–18] including updates form Gallium experiments [19, 20] as well as results from Borexino [21] on $^7$Be neutrinos.

The MINOS experiment has reported results on $\nu_\mu$ disappearance at a baseline of 735 km based on a two-year exposure from the Fermilab NuMI beam corresponding to a total of $3.36 \times 10^{20}$ protons on target [23]. The data confirm the energy dependent disappearance of $\nu_\mu$, showing significantly fewer events than expected in the case of no oscillations in the energy range $\lesssim 6$ GeV, whereas the high energy part of the spectrum is consistent with the no-oscillation expectation. We combine the long-baseline accelerator data from MINOS and K2K [24] with atmospheric

| parameter | Ref. [1] best fit$\pm 1\sigma$ | Ref. [1] $3\sigma$ interval | Ref. [10] best fit$\pm 1\sigma$ | Ref. [10] $3\sigma$ interval |
|---|---|---|---|---|
| $\Delta m^2_{21}$ [$10^{-5}$ eV$^2$] | $7.59^{+0.23}_{-0.28}$ | 7.03–8.27 | $7.59 \pm 0.20$ | 6.90–8.20 |
| $\Delta m^2_{31}$ [$10^{-3}$ eV$^2$] | $\pm 2.40^{+0.12}_{-0.11}$ | $\pm$(2.07–2.75) | $-2.40 \pm 0.11$<br>$+2.51 \pm 0.12$ | $-$(2.03–2.79)<br>$+$(2.15–2.90) |
| $\sin^2\theta_{12}$ | $0.318^{+0.019}_{-0.016}$ | 0.27–0.38 | $0.319 \pm 0.016$ | 0.27–0.37 |
| $\sin^2\theta_{23}$ | $0.50^{+0.07}_{-0.06}$ | 0.36–0.67 | $0.45^{+0.09}_{-0.05}$ | 0.33–0.65 |
| $\sin^2\theta_{13}$ | $0.013^{+0.013}_{-0.009}$ | $\leq 0.053$ | $0.014^{+0.013}_{-0.011}$ | $\leq 0.052$ |

Table 1: Determination of three–neutrino oscillation parameters from data available early in 2010 [1, 10].

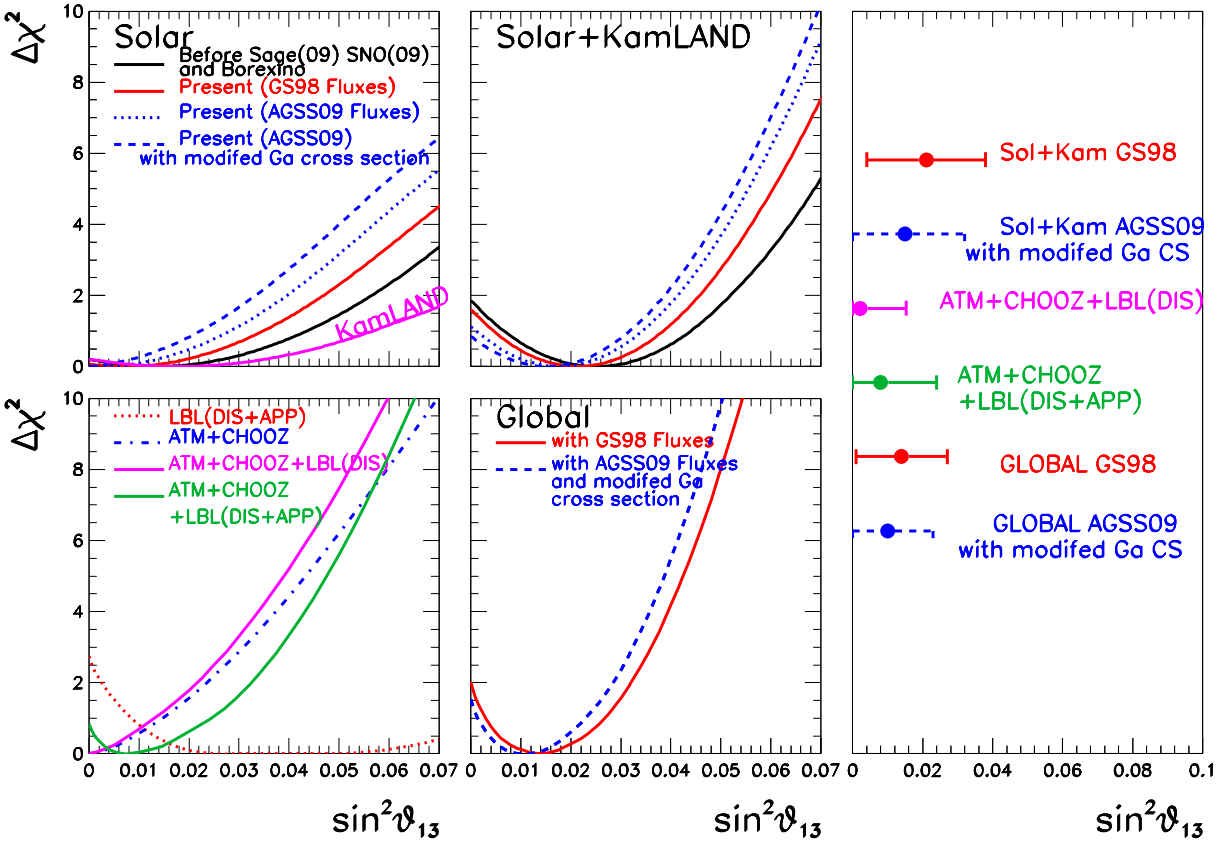


Figure 1: $\Delta\chi^2$ dependence on $\sin^2\theta_{13}$ from various data sets as labeled in the figure. The right panel shows $1\sigma$ ranges [10]. AGSS09 and GS98 refer to low and high metallicity solar models, respectively [22].

neutrino measurements from Super-Kamiokande [25]. The determination of $|\Delta m^2_{31}|$ is dominated by spectral data from the MINOS experiment, where the sign of $\Delta m^2_{31}$ (i.e., the neutrino mass hierarchy) is undetermined by present data. The measurement of the mixing angle $\theta_{23}$ is still largely dominated by atmospheric neutrino data from Super-Kamiokande with a best fit point close to maximal mixing. Small deviations from maximal mixing due to sub-leading three-flavour effects (not included in the analysis of [1, 26]) can be found in references [10, 27, 28], and can be compared with the results presented in table 1. A comparison of these subtle effects can be found in reference [29]. While an excess of sub-GeV $e$-like data provides an explanation for the deviations from maximality obtained in [10,27], these results are not statistically significant and are not confirmed by a recent analysis including $\Delta m^2_{12}$-effects by Super-Kamiokande [30].

The third mixing angle $\theta_{13}$ is of crucial importance for future oscillations experiments. Figure 1 summarises the information on $\theta_{13}$ from present data, which emerges from an interplay of different data sets. An important contribution to the bound comes, of course, from the CHOOZ reactor experiment [31] combined with the determination of $|\Delta m^2_{31}|$ from atmospheric and long-baseline experiments. Using this set of data, a possible hint for a non-zero $\theta_{13}$ from atmospheric data has been found in Refs. [27, 32]. The origin of such a hint has been investigated in some detail in reference [33], and more recently in [10, 12]. From these results one may conclude that the statistical relevance of the hint for non-zero $\theta_{13}$ from atmospheric data depends strongly on the details of the rate calculations and the $\chi^2$ analysis. Furthermore, the origin of the effect may be traced back to a small excess (at the $1\sigma$ level) in the multi-GeV $e$-like data sample in SK-I, which, however, is no longer present in the combined SK-I + SK-II data and is extremely weak in SK-I + SK-II + SK-III data. A very recent analysis (neglecting subleading $\Delta m^2_{21}$ effects) from the Super-Kamiokande collaboration finds no evidence of such a hint [30].

Another fragile indication of non-zero $\theta_{13}$ arises from the results of the MINOS experiment. In reference [34] a search for $\nu_\mu \to \nu_e$ transitions has been presented, based on a $3.14 \times 10^{20}$ protons-on-target exposure in the Fermilab NuMI beam. 35 events have been observed in the far detector with a background of $27 \pm 5(\text{stat}) \pm 2(\text{syst})$ events predicted by the measurements in the near detector. This corresponds to an excess of about $1.5\sigma$ which can be interpreted as a weak hint for $\nu_e$ appearance due to a non-zero $\theta_{13}$.

An important piece of information on $\theta_{13}$ comes from solar and KamLAND data. The relevant survival probabilities are given by:

$$P_{ee} \approx \begin{cases} \cos^4\theta_{13}\left(1 - \sin^2 2\theta_{12}\langle \sin^2\phi\rangle\right) & \text{solar, low energies / KamLAND} \\ \cos^4\theta_{13}\,\sin^2\theta_{12} & \text{solar, high energies}\,; \end{cases} \tag{1}$$

where $\phi = \Delta m^2_{21} L/4E$ and $\langle \sin^2\phi\rangle \approx 1/2$ for solar neutrinos. Equation (1) implies an anti-correlation of $\sin^2\theta_{13}$ and $\sin^2\theta_{12}$ for KamLAND and low energy solar neutrinos. In contrast, for the high energy part of the spectrum, which undergoes the adiabatic MSW conversion inside the sun and which is subject to the SNO CC/NC measurement, a positive correlation of $\sin^2\theta_{13}$ and $\sin^2\theta_{12}$ emerges. As discussed in [26, 35], this complementarity leads to a non-trivial constraint on $\theta_{13}$ and it allows the hint for a non-zero value of $\theta_{13}$ to be understood, which helps to

| Reference | best-fit and $1\sigma$ errors | significance |
|---|---|---|
| Schwetz *et al.* [1] (GS98) | $\sin^2\theta_{13} = 0.017^{+0.012}_{-0.011}$ | $1.7\sigma$ |
| Schwetz *et al.* [1] (AGSS09) | $\sin^2\theta_{13} = 0.013^{+0.013}_{-0.009}$ | $1.5\sigma$ |
| Gonzalez-Garcia *et al.* [10] (GS98) | $\sin^2\theta_{13} = 0.014^{+0.013}_{-0.011}$ | $1.3\sigma$ |
| Gonzalez-Garcia *et al.* [10] (AGSS09) | $\sin^2\theta_{13} = 0.010^{+0.013}_{-0.009}$ | $1.1\sigma$ |
| Fogli *et al.* [12] | $\sin^2\theta_{13} = 0.02 \pm 0.01$ | $2\sigma$ |

Table 2: Best-fit, $1\sigma$ range and statistical significance of the $\theta_{13} \neq 0$ hint from various global analyses. AGSS09 and GS98 refer to low and high metallicity solar models, respectively [22], which have been used in the fit of solar neutrino data.

reconcile the slightly different best fit points for $\theta_{12}$ as well as for $\Delta m^2_{21}$ for solar and KamLAND separately [28, 32, 35–37].

We found that the inclusion of the new solar data, and in particular of the SNO-LETA results tends to lower the statistical significance of $\theta_{13} \neq 0$ while the results from $\nu_e$ appearance from MINOS increases it. Within the context of the solar model with higher metallicities (GS98) and for the original Ga capture cross-section, we conclude that the significance of $\theta_{13} \neq 0$ from solar+KamLAND data is 79% ($\Delta\chi^2 = 1.6$) which increases to 84% ($\Delta\chi^2 = 2.0$) after inclusion of the atmospheric, CHOOZ and LBL data, and in particular of the results from $\nu_e$ appearance from MINOS. We also found that using the solar-neutrino fluxes required to fit the lower metallicity data (AGSS09) and/or the modified (lower) cross-section for neutrino capture in Ga lowers the best fit value of $\theta_{13}$ and its statistical significance. So, when using the AGSS09 fluxes and the lower Ga cross-section the significance of $\theta_{13} \neq 0$ from solar+KamLAND data is 70% ($\Delta\chi^2 = 1.1$) and 78% ($\Delta\chi^2 = 1.5$) when atmospheric, CHOOZ, and LBL data is included. These results are summarised in table 2.

### 2.2 The baseline Neutrino Factory

In this section we review work which has been done for the IDS-NF baseline Neutrino Factory [38], which has two source–detector baselines of 3 000–5 000 km and 6 000–8 000 km, two 50 kt Magnetised Iron Neutrino Detectors (MINDs) and a muon energy of 25 GeV. Given the fact that the current baseline is the result of many years of experimental and phenomenological research, some of the topics which follow deal with quite fine details. The overall conclusion is that the baseline is robust under the given technical constraints: beam luminosity of $10^{21}$ muon decays per year and the performance of the MIND detectors.

#### 2.2.1 Tau production in the disappearance channel

We address the little-studied issue of contamination of the golden, wrong-sign muon appearance, event sample from oscillations of muon or electron neutrinos (anti-neutrinos) into tau neutrinos (anti-neutrinos), which, through charged current (CC) interactions, result in tau leptons that

decay to muons. We focus on how this contribution alters the right-sign (RS) muon event sample and how it affects a precision measurement of $\theta_{23}$. In the case of the $\theta_{23}$ measurement, we have chosen to assume that $\theta_{23}$ is maximal and to consider the degree to which the contamination of the golden-event sample causes a deviation of $\nu_\mu \leftrightarrow \nu_\tau$ mixing from $\theta_{23} = \pi/4$. The measurement of a deviation from maximality is of significance in developing models for neutrino masses and mixings.

In spite of the suppression of the CC cross-section caused by the large mass of the tau, there is still a sizeable production rate above threshold ($E_\nu^{thr} \sim 3.4$ GeV) due to the high rate of $\nu_\mu \leftrightarrow \nu_\tau$ oscillations that are driven $\theta_{23}$ that is nearly maximal. The subsequent decay of the tau (with a branching ratio to muons of $\sim 17\%$) enhances the RS muon event rate, especially at small muon energies. This tau contribution alters the precision to which the mixing parameters can be determined. Neglect of the tau contribution will lead to an incorrect conclusion about the precision with which $\theta_{23}$ will be measured to be drawn.

We assume a basic muon storage ring configuration [38] with muon beam energy, $E_b = 25$ GeV and $5 \times 10^{20}$ useful decays per baseline, per year. The neutrino fluxes are integrated, assuming a gaussian angular divergence of the neutrino beam around the $z$-axis with standard deviation [4,39,40] $\sigma = 0.1/\gamma$, where $\gamma = E_b/m_\mu$, and then averaged over a small opening angle, $\theta' < 0.3\sigma$ or roughly 0.1 mr.

The muon (tau) neutrinos produce 'direct' muons (taus) in a 50 kTon iron detector such as the proposed INO/ICAL or MIND at a distance $L$ from the source, through CC quasi-elastic, resonant, or deep-inelastic interactions. The direct taus are forward peaked (see figure 2) and subsequently decay to produce muons, most of which are of low energy; see referenc [41] for details.

A 7% energy resolution and a 90% muon recontruction efficiency are assumed. Typical event rates, accumulated over five years at $L = 7400$ km (the 'magic' baseline) for oscillation parameters: $\Delta m^2 \equiv m_3^2 - (m_1^2 + m_2^2)/2 = 2.4 \times 10^{-3}$ eV$^2$; $\theta_{23} = 42^\circ$; $\theta_{13} = 1^\circ$; $\sin^2\theta_{12} = 0.304$; and $\Delta_{21} \equiv m_2^2 - m_1^2 = 7.65 \times 10^{-5}$ eV$^2$; are shown as a function of the observed lepton energy in figure 3.

It can be seen that there is a substantial contribution to the events from tau decay into muons. Since tau production in neutrino-nucleon interactions is extremely forward-peaked, one obvious way to remove the tau contribution is with an angular cut (a muon energy cut can also be contemplated). However, (see figure 4), the only cut effective in removing the tau contribution ($\theta_\mu > 25^\circ$) also removes the signal itself! A muon energy cut of $E > 10$–$15$ GeV, removes a substantial fraction of the tau contribution, but this cut will worsen the measured precision of the mixing parameters. In short, it is not feasible to cut out the tau contribution and still make a precision measurement, in this case, of the deviation of $\theta_{23}$ from maximality.

The $\theta_{23}$ dependent terms in $P_{\mu\mu}$ and $P_{\mu\tau}$ have opposite sign, hence the combination of muons from direct production and from tau decays marginally *decreases* the sensitivity of the event rate to this angle. The inclusion of muons from tau events also alters the uncertainties considerably. A near detector sensitive to muons measures the combination of flux times cross-section. This

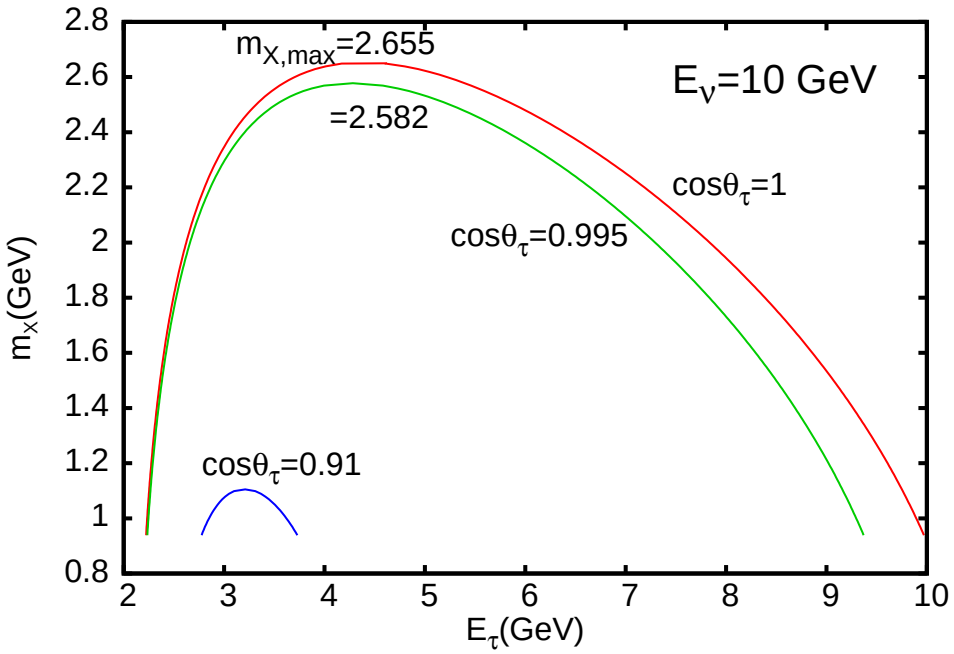


Figure 2: Kinematics of $\nu_\tau$–nucleon CC interactions. The allowed parabolas of constant $\cos\theta_\tau$ in the $m_X$-$E_\tau$ plane (shown for $E_\nu = 10$ GeV) are severely restricted for $\cos\theta_\tau$ away from 1. The ends of the parabolas (at $m_X = M$) give the limits of the tau energy; $m_X^2 = W^2 = (p+q)^2$, where $p$ ($q$) is the nucleon (intermediate boson) 4-momentum in the laboratory frame.

also appears in the RS event rate for direct muon production and is therefore well constrained. However, for tau production and decay, the RS event rate depends on a combination of the muon-neutrino flux and the tau-production cross section. The tau-production cross sections have larger uncertainties, since mass corrections are large. Furthermore, since these contributions result from oscillations, no near detector can help reduce the uncertainties. Hence, the overall uncertainties are much larger for the tau contribution than for direct muons.

Hence, in our numerical calculations we use an overall normalization error of 0.1% for direct muon-event sample and a modest 2% uncertainty is used for the total number (direct plus tau) muon events. The full sample, without charge identification is preferable due to the higher detection efficiency. We therefore add the events (RS+WS) from both $\mu^-$ and $\mu^+$ beams. We use typical input values of $(\Delta m^2, \theta_{23}, \theta_{13})$ to estimate how well the generated "data" can be fitted and calculate the resulting precision on the parameters. We keep the solar parameters fixed at the best-fit values of reference [1] and set $\delta_{CP}$ to zero. The best fits (and regions of confidence levels in parameter space) are obtained by first minimising the chi-squared first, with a pull corresponding to the normalization uncertainties specified above, and then minimising chi-squared over $\Delta m^2$ and $\theta_{23}$, keeping $\theta_{13}$ fixed.

Figure 5 shows the allowed $\Delta m^2$–$\theta_{23}$ parameter space at 99% CL for a typical set of inputs: $\Delta m^2, \theta_{23}, \theta_{13} = 2.4 \times 10^{-3}$ eV$^2$; 41.9°, 1°. The 99% CL contour is much more constrained using the direct muon sample than using the full (direct plus tau) sample. In particular, it is the $\Delta m^2$ values that are smaller than the input value that broaden the contour and limit the

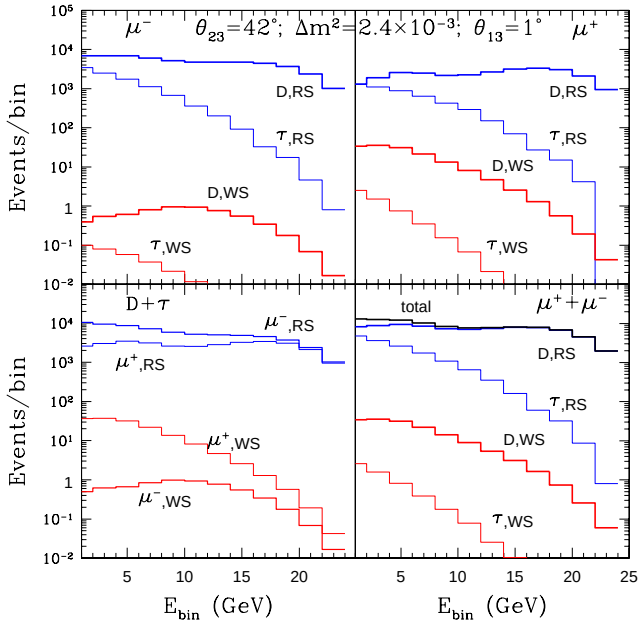


Figure 3: Muon event rates as a function of the observed muon energy. RS and WS events from $\mu^-$ and $\mu^+$ beams are shown in the upper panels. Contributions from direct muon production (denoted by $D$) and that of muons from tau decay (labeled as $\tau$) are shown separately. The left lower panel shows the sum $D+\tau$. Oscillation parameters are as given in text.

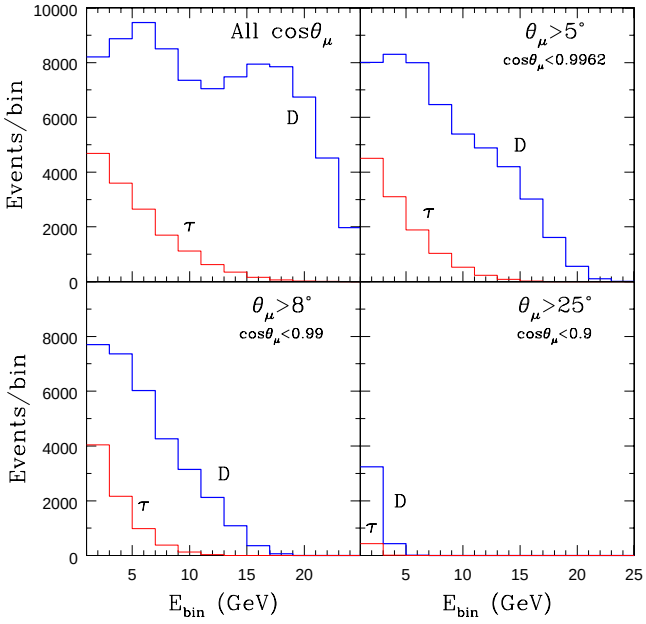


Figure 4: Effects of angular cuts on the tau contribution to muon events at neutrino factories. For details, see the text.

discrimination. The largest true value of $\theta_{23}$ that can be discriminated from maximal is shown in figure 6, as a function of $\Delta m^2$ again, for $\theta_{13} = 1°$. It is seen that tau contamination worsens the ability to discriminate $\theta_{23}$ from maximal, thus making this measurement harder than originally expected.

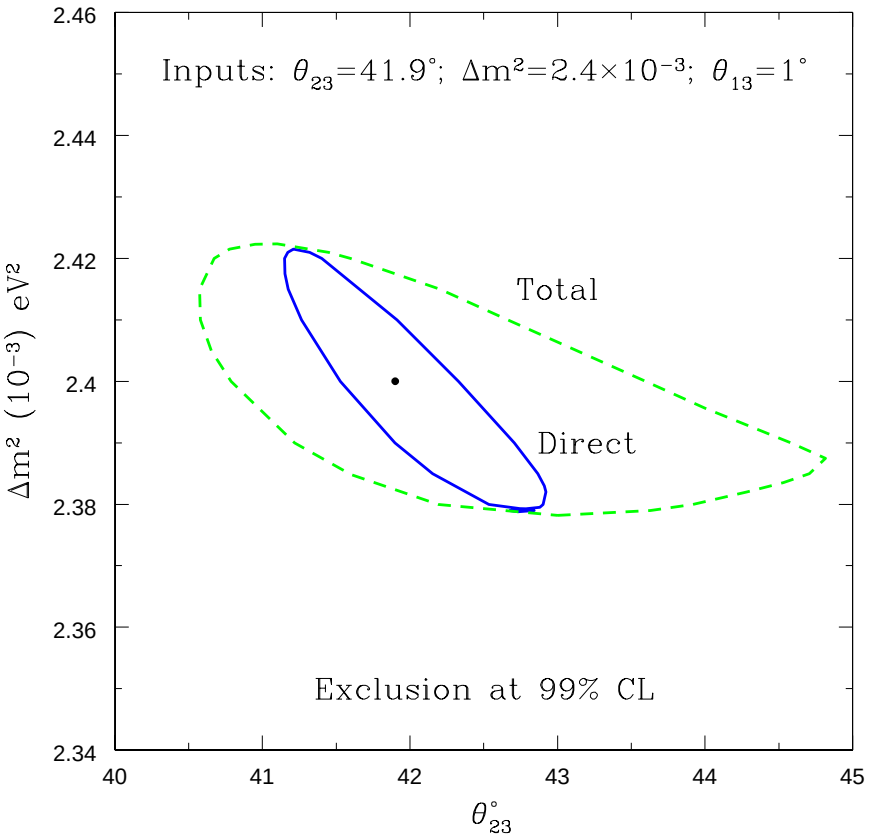


Figure 5: Allowed $\Delta m^2$-$\theta_{23}$ parameter space at 99% CL from CC muon events, directly produced (solid line) and with inclusion of those from tau decay (dashed line). See text for values of input parameters.

The oscillations of the muon or electron neutrinos (anti-neutrinos) to tau neutrinos (anti-neutrinos) results in tau leptons produced through CC interactions in the detector which, on leptonic decay, add to the right- as well as wrong-sign muon event samples. This tau contamination worsens the ability to discriminate against maximal $\nu_\mu \leftrightarrow \nu_\tau$ mixing. It is practically impossible to devise satisfactory cuts to remove this tau contamination. Uncertainties from this tau background must be brought under control before making precision parameter measurements at the Neutrino Factory.

### 2.2.2 Near detectors at the Neutrino Factory

The issue of near detectors has received little attention to date and, at present, there is no detailed design for a near detector from the Detector Working Group of the IDS-NF. Therefore,

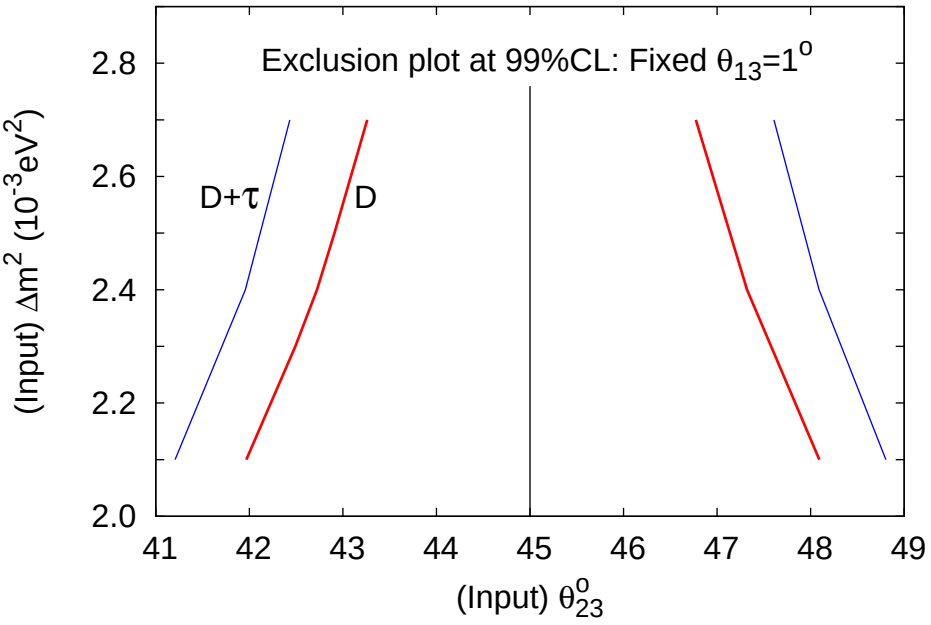


Figure 6: The largest (smallest) true value of $\theta_{23}$ in the first (second) octant that can be discriminated from $\theta_{23} = \pi/4$, as a function of $\Delta m^2$ are shown when only Direct ($D$) and total ($D + \tau$) events are considered; Here $\theta_{13}$ is fixed at $1^\circ$.

in this section the requirements for a useful suite of near detectors are outlined. Clearly, this topic requires further intense study in close collaboration with the Detector WG.

#### 2.2.2.1 Motivation

As far as the importance and requirements for near detectors at a Neutrino Factory are concerned, the key questions include:

- What is the potential of near detectors to reduce systematic uncertainties?
- When do we need a near detector for standard oscillation physics?
- What (minimal) characteristics do we require, such as technology, number, and sites? and
- What properties do near detectors need for new physics searches?

From these questions, two obstacles can be identified: first, one has to address which kind of systematics near detectors should be designed to reduce; and second, one has to address what kind of new physics near detectors should be optimised to search for. In the following, we split the discussion into standard oscillation physics and new physics searches.

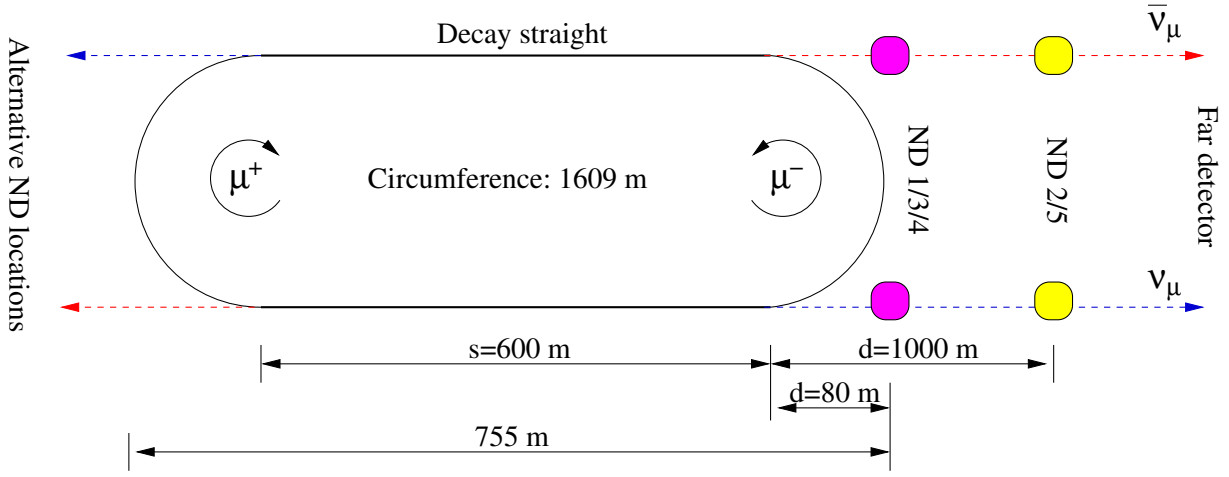


Figure 7: Geometry of the muon storage ring and possible near detector (ND) locations (not to scale). The baseline $L$ is the distance between production point and near detector, i.e., $d \leq L \leq d + s$. Figure taken from reference [42].

#### 2.2.2.2 Near detectors for standard oscillation physics

As illustrated in figure 7, (at least) two near detectors are required at the Neutrino Factory if the $\mu^-$ and $\mu^+$ circulate in different directions in the ring, unless the sense of rotation of the muon beam is reveresed from time to time. For the same reason, charge identification is, in principle, not required for the cross section measurements, since there are no wrong-sign muons produced by oscillations so close to the source. However, for background measurements (such as from charm decays), a magnetic field is necessary. It was demonstrated in reference [42] that the size, location, and geometry of the near detectors hardly matter for standard oscillation physics even in extreme cases of possible near detectors. Because of the high statistics in all energy bins of the near detectors, the physics potential is generally limited by the statistics in the far detector(s). However, note that rare interactions used for flux monitoring, such as inverse muon decays or elastic scattering, may require large enough detectors. A possible near detector design for a neutrino factory is, for instance, discussed in reference [43].

As far as the treatment of systematic uncertainties is concerned, the current IDS-NF baseline setup relies on uncorrelated (among all oscillation channels, detectors, and neutrinos-antineutrinos) signal and background normalisation errors. The near detector(s) is (are) treated implicitly, whereas a more realistic analysis of systematics uncertainties requires particular correlations. For example, the cross-section uncertainties are correlated among all channels and detectors measuring the same $\nu_\mu$ or $\bar{\nu}_\mu$ (inclusive) charged-current cross sections, but there may be a shape error, i.e., the errors may be uncorrelated among the energy bins. On the other hand, flux errors are correlated among all detectors and channels from the muon same decays in the same straight section and are correlated among different energy bins. In reference [42], the systematic uncertainties which are, in principle, reducible by the use of near detectors have been considered. Note that there may be other types of systematics, such as fiducial volume uncertainties, which have not yet been discussed. The refined treatment of systematic uncer-

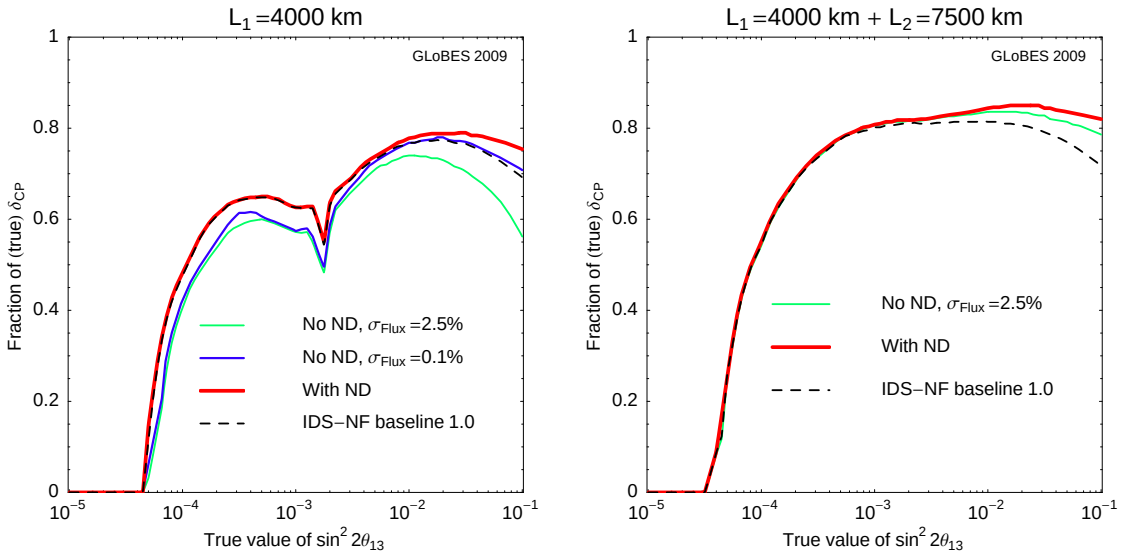


Figure 8: CP violation discovery reach as a function of true $\sin^2 2\theta_{13}$ and the fraction of (true) $\delta_{\rm CP}$ for one far detector (left) and two far detectors (right); $3\sigma$ CL. Figure taken from reference [42].

tainties is illustrated for the CP-violation discovery reach in figure 8. The figure also incudes the current IDS-NF parameterisation (dashed curves) for comparison. In the left panel, only one baseline is used. In this case, the near detectors turn out to be very important. In the right panel, the combination of two baselines is shown. The result, using the new systematics treatment, is already better than the previous one, even without the near detector, because the cross sections are fully correlated between the two detectors. This means that possible cross section errors cancel. The near detectors improve the result even further.

#### 2.2.2.3 Near detectors for new physics searches

In order to address the requirements for near detectors for new physics searches, one has to specify which type of new physics is under consideration. Here we show a number of examples to produce a list of detector requirements which should be as complete as possible. If the new physics originates from heavy mediators, which are integrated out, the new physics can be parameterized in the effective operator picture. The lowest possible effective operators affecting the production, propagation, or detection of neutrinos are dimension six operators, suppressed by $v^2/\Lambda^2$ by the new physics scale $\Lambda$ compared to the Standard Model Higgs vacuum expectation value, $v$. At tree level, they can be mediated by heavy neutral fermions, leading to a non-unitary (NU) mixing matrix after the re-diagonalization and re-normalization of the kinetic terms of the neutrinos (see, for example, reference [44] for a short summary), or by scalar or vector bosons, leading to so-called non-standard interactions (NSI; see, for example reference [45] for the terminology). A very different type of new physics is the oscillation into light sterile neutrinos, because it may lead to oscillation signatures. We consider near detectors for these three applications. In contrast to near detectors contributing to standard oscillation

measurements, near detectors optimised for the search for new physics must have as large a mass as possible. This is because the new physics sensitivity is in many cases limited by the statistics in the near detectors.

The most interesting non-standard interactions for near detectors may be $\epsilon^s_{e\tau}$ and $\epsilon^s_{\mu\tau}$, which replace an initial $\nu_e$ or $\nu_\mu$ in the beam by a $\nu_\tau$. Since these NSI lead to a zero-distance effect $\propto |\epsilon_{\alpha\tau}|^2$. As illustrated in reference [42], the sensitivity to these parameters can be significantly improved in the presence of $\nu_\tau$ near detectors. If the two effects need to be distinguished, charge identification is required. Assuming that this new physics effect originates from $d = 6$ NSI without charged lepton flavour violation, the bounds from the source effects directly relate to the bounds on the NSI matter effect $\epsilon^m_{\mu\tau}$ [46] (see also reference [47] for a model). In particular models, also other types of NSI at the source may be interesting, such as $\epsilon^s_{e\mu}$ from a Higgs triplet as type-II see-saw mediator [48]. This application relies on the excellent charge identification properties of the near detector(s). The above mentioned non-unitarity leads to a particular, fundamental correlation among source, matter, and detector effects. In this case, near detectors improve the measurements in a similar way [44]. Both the NSI and non-unitarity searches have in common that the near detector location only affects statistics, whereas there is no relevant oscillation effect close to the source.

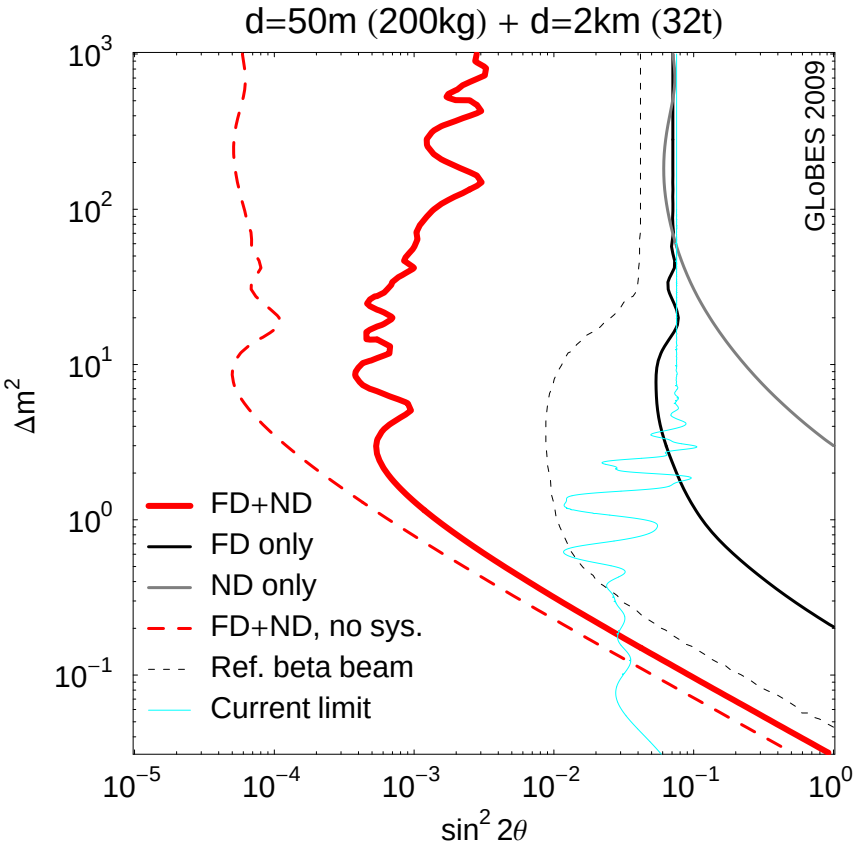


Figure 9: Exclusion limit in the $\sin^2 2\theta$-$\Delta m^2$ plane for $\nu_e$ disappearance into sterile neutrinos from the two detector setup discussed in the main text (thick solid curve, 90% CL, 2 d.o.f.). Figure taken from reference [49].

The search for sterile neutrinos is qualitatively different: the location of the near detectors affects the sensitive range in $\Delta m^2$. An interesting example is the disappearance of $\nu_e$ at short baselines, discussed in reference [49]. In this case, the oscillations have to be averaged over the decay straight, which leads to significant effects for near detectors very close to the source (or large $\Delta m^2$). In addition, the unknown cross section errors play the same role as the unknown fluxes in the two-detector reactor experiments, such as Double Chooz or Daya Bay. Therefore, a similar approach has been proposed in reference [49]: two sets of near detectors at different (short) baselines, which are sensitive to different $\Delta m^2$-ranges, are important for the systematics cancellation of the cross section errors. The result is illustrated in figure 9 for $d = 50\,\text{km}$ (ND) and $d = 2\,\text{km}$ (FD), where the thick curve shows the combined sensitivity. If only ND or FD is used (medium thin solid curves), the sensitivity is limited by the knowledge of the cross sections. Obviously, the current bound can be exceeded by two orders of magnitude.

#### 2.2.2.4 Synergy with superbeam near detectors

Recently, the possibility of a new near detector for tau neutrinos in the NuMI beam has been drawing some attention [50]. Such a detector might have a similar sensitivity to new physics searches as the Neutrino Factory near detectors. However, the two beams have different characteristics. At the Neutrino Factory, neutrinos are produced from muon decays, implying that both $\nu_\mu$ ($\bar\nu_\mu$) and $\bar\nu_e$ ($\nu_e$) are in the beam for $\mu^-$ ($\mu^+$) stored, 50% each. The origin of the neutrinos is typically determined by charge identification of the secondary particle in the detector. For tau neutrino detection, the origin can be $\bar\nu_e \to \bar\nu_\tau$ ($\nu_e \to \nu_\tau$) or $\nu_\mu \to \nu_\tau$ ($\bar\nu_\mu \to \bar\nu_\tau$) transitions. At the superbeam, the neutrinos are mainly produced through pion decays. Only $\nu_\mu$ ($\bar\nu_\mu$) are in the beam for $\pi^+$ ($\pi^-$) decays, with some contamination from other flavours and polarities. For tau neutrino detection, only $\nu_\mu \to \nu_\tau$ ($\bar\nu_\mu \to \bar\nu_\tau$) transitions are accessible with reasonable sensitivities. However, the absence of a significant amount of $\bar\nu_e$ ($\nu_e$) in the beam may, depending on the detector technology, also be an advantage with respect to the suppression of $\bar\nu_e$ ($\nu_e$) charm induced backgrounds. In summary, new physics searches at the Neutrino Factory and superbeam may be complementary if the new physics effect:

- Is only present in either muon decays or pion decays (such as leptonic versus hadronic source NSI); or
- Requires either low backgrounds (superbeam) or the $\bar\nu_e \to \bar\nu_\tau$ ($\nu_e \to \nu_\tau$) channel (Neutrino Factory).

Let us illustrate this complementarity with one example from reference [51]. This example tests if one can distinguish phenomenologically NU from NSI, which may be interpreted as distinguishing between fermions and bosons as heavy mediators of the non-standard effect, at least to leading order at $d = 6$ and tree level. We therefore refer to these effects at $d = 6$ as $\mathcal{O}^{\mathcal{F}}$ (NU) and $\mathcal{O}^{\mathcal{S}}$ (NSI), respectively. At the Neutrino Factory, the phenomenology of $\mathcal{O}^{\mathcal{F}}$ and $\mathcal{O}^{\mathcal{S}}$ is, however, very similar. Both effects can be parameterized in form of NSI. For $\mathcal{O}^{\mathcal{F}}$, particular correlations among source, propagation, and detection effects are present [52, 53]. For leptonic

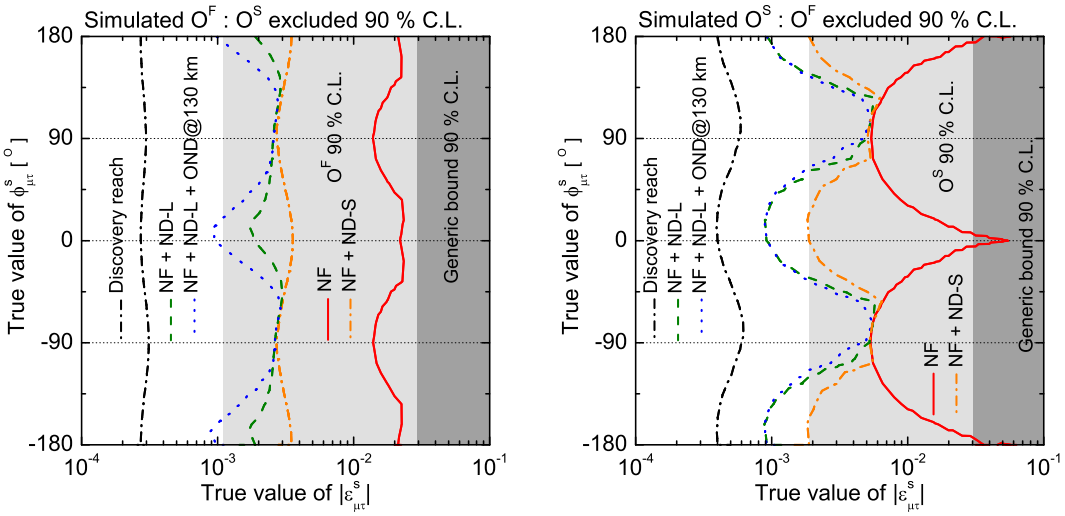


Figure 10: Regions in the ($|\varepsilon^s_{\mu\tau}|$-$\phi^s_{\mu\tau}$)-plane where the simulated $\epsilon^s_{\mu\tau}$ induced by one type of operator can be uniquely established, *i.e.*, the other type of operator is excluded at the 90% C.L. (regions on the right-hand side of the curves). Left panel: the simulated $\varepsilon^s_{\mu\tau}$ is induced by $\mathcal{O}^{\mathcal{F}}$ (non-unitarity) and fitted with $\mathcal{O}^{\mathcal{S}}$ (NSI from $d = 6$ operator). Right panel: the simulated $\varepsilon^s_{\mu\tau}$ is induced by $\mathcal{O}^{\mathcal{S}}$ and fitted with $\mathcal{O}^{\mathcal{F}}$. The different curves corresponds to the IDS-NF baseline setup (NF), an additional (small) silicon vertex-sized near detector (ND-S), an additional OPERA-like near detector at 1 km (ND-L), and an additional OPERA-like near detector at 130 km (OND@130 km). In both panel, the discovery reach is also displayed, and the current limits are shown as shaded regions. Figure taken from reference [51].

$\mathcal{O}^{\mathcal{S}}$, similar correlations are obtained for operators without charged lepton flavour violation [46]. Consider, for instance:

$$\varepsilon^m_{\mu\tau} = -(\varepsilon^s_{\mu\tau})^* \qquad \text{(NSI)}\,; \tag{2}$$

$$\varepsilon^m_{\mu\tau} = -\varepsilon^s_{\mu\tau} \qquad \text{(NU)}\,. \tag{3}$$

In this case, the two effects can be mostly distinguished by the absence of detection effects in the case of $\mathcal{O}^{\mathcal{S}}$. Alternatively, one could use a superbeam-based source, where equation 2 does not hold because of the neutrino production by pion decays. We illustrate the identification of the class of effect in figure 10. Obviously, the effects can be hardly distinguished with the Neutrino Factory alone beyond the current bounds. However, the discovery reach for the non-standard effects clearly exceeds the current bounds. A super-beam-based detector could disentangle the two effects in the region between the bounds and the discovery reach if it had a sensitivity significantly exceeding $10^{-3}$ in $|\epsilon^s_{\mu\tau}|$.

#### 2.2.2.5 Summary of requirements

The requirements/characteristics of near detectors at the Neutrino Factory can be summarised as follows: for standard oscillation physics, the exact location, size, and geometry of the detectors hardly matters because of the large statistics. Data for the $\nu_\mu$ and $\bar{\nu}_\mu$ cross sections are sufficient, because only these two are needed in the far detectors (for the high energy Neutrino Factory). If

the $\mu^+$ and $\mu^-$ circulate in the storage ring(s), two near detectors are needed unless the sense of direction of the muon beams are reversed from time to time. A magnetic field may be necessary for background measurements.

For nearly all new physics applications, the sizes (masses) of the near detectors are important. Since the size of the detector cannot be arbitrarily increased beyond the opening angle of the beam, the detectors should be as long as possible in order to capture a large portion of the on-axis flux. For new physics searches, all flavours should be measured, and charge identification is mandatory for many applications. For some purposes, such as the short baseline electron-neutrino disappearance, more than one set of near detectors may be required. In addition, for any light sterile neutrino-oscillation search, the baselines of the near detectors are very important. Energy resolution, on the other hand, is of secondary importance, since the energy resolution is, close to the source, limited by the extension of the decay straight. The sensitivity to new physics searches from heavy mediators should significantly exceed $10^{-3}$ in $|\epsilon^s|$ in order to improve the current bounds.

In conclusion, near detectors at the Neutrino Factory are important for both standard oscillation physics and new physics searches. From the physics point of view, however, the requirements, such as size and location, may be driven by new physics searches.

### 2.2.3 Physics case for tau detection at the intermediate baseline

The following section is derived from IDS-NF note 008 [54] and was prepared as part of a baseline change request. As a result of this request, a study was performed which demonstrated that the statistical weight of the MECC as presently defined does not give a significant impact on the determination of the standard oscillation parameters. The importance of tau detection meant that the possibility of including a $\nu_\tau$-detector at the intermediate, and possibly the long, baseline, will be retained [8]. We feel that we have successfully demonstrated how to carry such request through all steps of the procedure, although in future, we may want to speed up the process.

#### 2.2.3.1 Standard oscillation physics

The prime focus of the Neutrino Factory is to provide precision measurements or tight constraints on the three-flavour oscillation parameters. Many studies done in the context of the ISS [4, 55] show that the potential to achieve this is excellent if it is ensured that parameter correlations and degeneracies can be resolved. Any single rate measurement at some fixed baseline $L$ and neutrino energy $E$ is sensitive only to a *combination* of parameters. To measure all parameters separately, the following possibilities exist to resolve the correlations and degeneracies:

- **Use measurements at different energies:** This is difficult at the Neutrino Factory due to the limited width of the neutrino spectrum and the limited energy resolution of the MIND

detector. It has been shown that the energy resolution of MIND is not enough for a single detector located at the intermediate baseline to solve all of the degeneracies;

- **Perform measurements at two different baselines $L_1$ and $L_2$:** This is an extremely powerful possibility, which is the reason it is included in the current IDS-NF baseline setup. In particular, a measurement at the magic baseline [56] turns out to be very important. A detailed optimization study for $L_1$ and $L_2$ has been performed in [57], with the result that the combination $L_1 = 4\,000$ km, $L_2 = 7\,500$ km is optimal to study standard oscillation physics as well as non-standard neutrino interactions; and

- **Study different oscillation channels:** With MIND detectors, the golden ($\nu_e \to \nu_\mu$) and disappearance ($\nu_\mu \to \nu_\mu$) channels are available, while an inclusion of a $\nu_\tau$ detector could in addition provide a window on the silver ($\nu_e \to \nu_\tau$) and Discovery ($\nu_\mu \to \nu_\tau$) channels. Reference [57], however, shows that the combination of one MIND detector and one Emulsion Cloud Chamber (ECC) at the intermediate baseline is not as good as the combination of two MINDs at two baselines, mainly because of the very low statistics at the $\tau$-detector for $\theta_{13} \leq 2^\circ$. On the other hand, adding one ECC to the setup with two MINDs does not provide more than a marginal gain in sensitivity, independent of the neutrino energy and baseline. The reason is that the analytical expressions for the oscillation probabilities in the golden and silver channels are very similar (they differ only in the signs of certain terms and in the exchange $\sin\theta_{23} \leftrightarrow \cos\theta_{23}$ in several others), so that the silver channel could help only to resolve degeneracies. This, however, is already done by the combination of the two golden-channel detectors. We have also checked numerically that the inclusion of the discovery channel does not improve the sensitivity of the Neutrino Factory to standard three-flavour oscillations.

  In reference [58], the silver channel was studied to solve the octant degeneracy and as a tool to study deviations from maximality of the atmospheric angle $\theta_{23}$. A comprehensive study of alternatives to the silver channel for these tasks is lacking, see reference [59]. A likely outcome of such a study will be that alternatives are better than the silver channel. However, in the absence of such a study, we cannot draw a firm conclusion.

As for the standard three-family oscillations, we therefore believe that an ECC detector able to look for $\nu_e \to \nu_\tau$ and $\nu_\mu \to \nu_\tau$ channels will not improve significantly the performances of the baseline Neutrino Factory setup with two MINDs, due to the strong statistical limitations of the present detector design and to the relatively limited number of parameters to be measured.

#### 2.2.3.2 Non-standard oscillation physics

There are several interesting cases of new physics that can be studied through neutrino oscillation experiments. We will address here the potential of a detector capable of $\tau$-identification in searching for Non-Standard Interactions (NSI) or additional singlet fermions with some admixture with the three-family left-handed neutrinos, so-called "sterile neutrinos".

Non-standard interactions are effective four-fermion interactions which arise if neutrinos couple to new, heavy particles. This is similar to the Fermi theory of nuclear beta decay emerging as the low-energy fingerprint of the Standard Model weak interactions. NSI can affect the neutrino production and detection mechanisms if they are of the charged-current type, and neutrino propagation if they are of the neutral-current type. In the first case, the NSI can be parametrised as a small admixture of the "wrong flavour" $|\nu_\beta\rangle$ to a neutrino produced or detected in association with a charged lepton of flavour $\alpha$:

$$|\nu_\alpha^s\rangle = |\nu_\alpha\rangle + \sum_{\beta=e,\mu,\tau} \varepsilon_{\alpha\beta}^s |\nu_\beta\rangle\,; \qquad \text{e.g. } \pi^+ \xrightarrow{\varepsilon_{\mu e}^s} \mu^+\nu_e\,; \tag{4}$$

$$\langle\nu_\alpha^d| = \langle\nu_\alpha| + \sum_{\beta=e,\mu,\tau} \varepsilon_{\beta\alpha}^d \langle\nu_\beta|\,; \qquad \text{e.g. } \nu_\tau N \xrightarrow{\varepsilon_{\tau e}^d} e^- X\,. \tag{5}$$

The second case corresponds to a non-standard contribution to the MSW potential:

$$\tilde{V}_{\rm MSW} = \sqrt{2} G_F N_e \begin{pmatrix} 1+\varepsilon_{ee}^m & \varepsilon_{e\mu}^m & \varepsilon_{e\tau}^m \\ \varepsilon_{e\mu}^{m*} & \varepsilon_{\mu\mu}^m & \varepsilon_{\mu\tau}^m \\ \varepsilon_{e\tau}^{m*} & \varepsilon_{\mu\tau}^{m*} & \varepsilon_{\tau\tau}^m \end{pmatrix}\,. \tag{6}$$

In the above expressions, the parameters $\varepsilon_{\alpha\beta}^{s,d,m}$ give the strength of the NSI relative to standard weak interactions. A generic estimate is:

$$|\varepsilon_{\alpha\beta}^{s,d,m}| \sim \frac{M_{\rm W}^2}{M_{\rm NSI}^2}\,; \tag{7}$$

where $M_{\rm NSI}$ is the new physics scale at which the effective NSI operators are generated. The present, model-independent, bounds on the $\varepsilon_{\alpha\beta}^{s,d,m}$ are not very strong ($\mathcal{O}(0.1-1)$). However, these bounds are not likely to be saturated in specific models [46, 53]; at least if one follows the usual guidelines of model building: no fine-tuning, as few new particles as possible, new physics preferably at or above the TeV scale, *etc.* Indeed, if the estimate of equation 7 is taken at face value, with $M_{\rm NSI} \sim 1$ TeV, we expect $\varepsilon_{\alpha\beta}^{s,d,m} < 0.01$. It is important to keep in mind that, in any specific model, the phenomenological parameters $\varepsilon_{\alpha\beta}^{s,d,m}$ will in general not be independent.

Phenomenological models in which $N$ new singlet fermions are mixed with the three left-handed ones imply a straightforward generalisation of the PMNS matrix to a $(3+N)\times(3+N)$ unitary mixing matrix, that for the case of $N=1$ is:

$$U_{\rm PMNS} = \begin{pmatrix} U_{e1} & U_{e2} & U_{e3} & U_{e4} \\ U_{\mu 1} & U_{\mu 2} & U_{\mu 3} & U_{\mu 4} \\ U_{\tau 1} & U_{\tau 2} & U_{\tau 3} & U_{\tau 4} \\ U_{s1} & U_{s2} & U_{s3} & U_{s4} \end{pmatrix}\,. \tag{8}$$

Some of these elements are strongly constrained by non-observation at reactors and at the MiniBooNE experiment. On the other hand, models in which the mixing angles $\theta_{i4}$ between a new singlet fermion $\nu_s$ and the three active ones are all very small cannot be excluded. Notice that, both for NSI and sterile neutrino models, new CP-violating phases are present in addition to the standard three-family oscillation phase $\delta$.

#### 2.2.3.3 NSI in production and detection

NSI in production and detection imply non-unitarity of the PMNS matrix. Therefore, if some of the new parameters $\epsilon^{s,d}_{\alpha\beta}$ are non-vanishing, it is not enough to study the two channels available at the MIND detector (the $\nu_e \to \nu_\mu$ golden channel and the $\nu_\mu \to \nu_\mu$ disappearance channel) to measure all of the new parameters of the model. To search for non-unitarity of the leptonic mixing matrix, there are two options:

- Measure all the oscillation probabilities $P(\nu_\mu \to \nu_e)$, $P(\nu_\mu \to \nu_\mu)$, $P(\nu_\mu \to \nu_\tau)$ (or $P(\nu_e \to \nu_e)$, $P(\nu_e \to \nu_\mu)$, $P(\nu_e \to \nu_\tau)$, and check if they sum up to unity. A problem of this approach is that $\nu_e$ detection is very difficult in a MIND detector, so either there will be large uncertainties or a secondary detector with a different technology (for example, liquid argon) should be added to the two-MIND setup. Moreover, the systematic errors in the different oscillation channels will be different, which also limits the achievable sensitivity;
- Use neutral current events. This is also difficult [60], and, at present, only a sensitivity at the ten per cent level can be achieved. This might improve if the neutral current cross sections were known better and if more sophisticated event selection criteria could be developed.

Most of the new parameters could be measured using a dedicated near detector. The detector design should be optimized so as to measure as many oscillation channels as possible, and with very good $\tau$-identification capability. Therefore, this detector cannot be a scaled version of MIND. At present, no detailed study of such a detector has been performed, see references [46,53] for the potential of an ECC close to the Neutrino Factory source and the recent reference [42].

#### 2.2.3.4 NSI in propagation

NSI in propagation do not imply a non-unitary PMNS matrix. In this case it is therefore possible to obtain information on all of the new parameters $\epsilon^{m}_{\alpha\beta}$ using the two channels available at the MIND detector.

A detailed study of NSI in propagation at the Neutrino Factory has been presented in reference [57] (see figure 11, taken from that paper). The results obtained show that the IDS-NF baseline Neutrino Factory with two MIND detectors at $L \sim 4000$ km and $L \sim 7500$ km is sensitive to $\varepsilon^{m}_{\alpha\beta} \sim 0.01 - 0.1$, independent of whether a $\nu_\tau$ detector is present. There might be a physics case for this detector if the process $\nu_\tau + N \to \tau + X$ proceeds in an unexpected way (e.g. an anomalous energy dependence), if $\tau$ leptons are produced in a non-standard way (e.g. $\varepsilon^{d}_{e\tau} \neq 0$ or $\varepsilon^{d}_{\mu\tau} \neq 0$), or if the muons stored in the Neutrino Factory have a small branching to $\nu_\tau$, e.g. due to $\varepsilon^{s}_{\mu\tau} \neq 0$ or $\varepsilon^{s}_{e\tau} \neq 0$. In the first case, a $\nu_\tau$ detector at around the first oscillation maximum would be required because the $\nu_\tau$ flux first has to be generated by oscillation from $\nu_\mu$; in the second case, a $\nu_\tau$ *near* detector would be optimal due to the higher flux at the near site.

From this analysis, we conclude that an ECC detector to look for $\tau$'s produced through $\nu_e \to \nu_\tau$ does not improve the expected IDS-NF baseline setup sensitivity to NSI in propagation. A

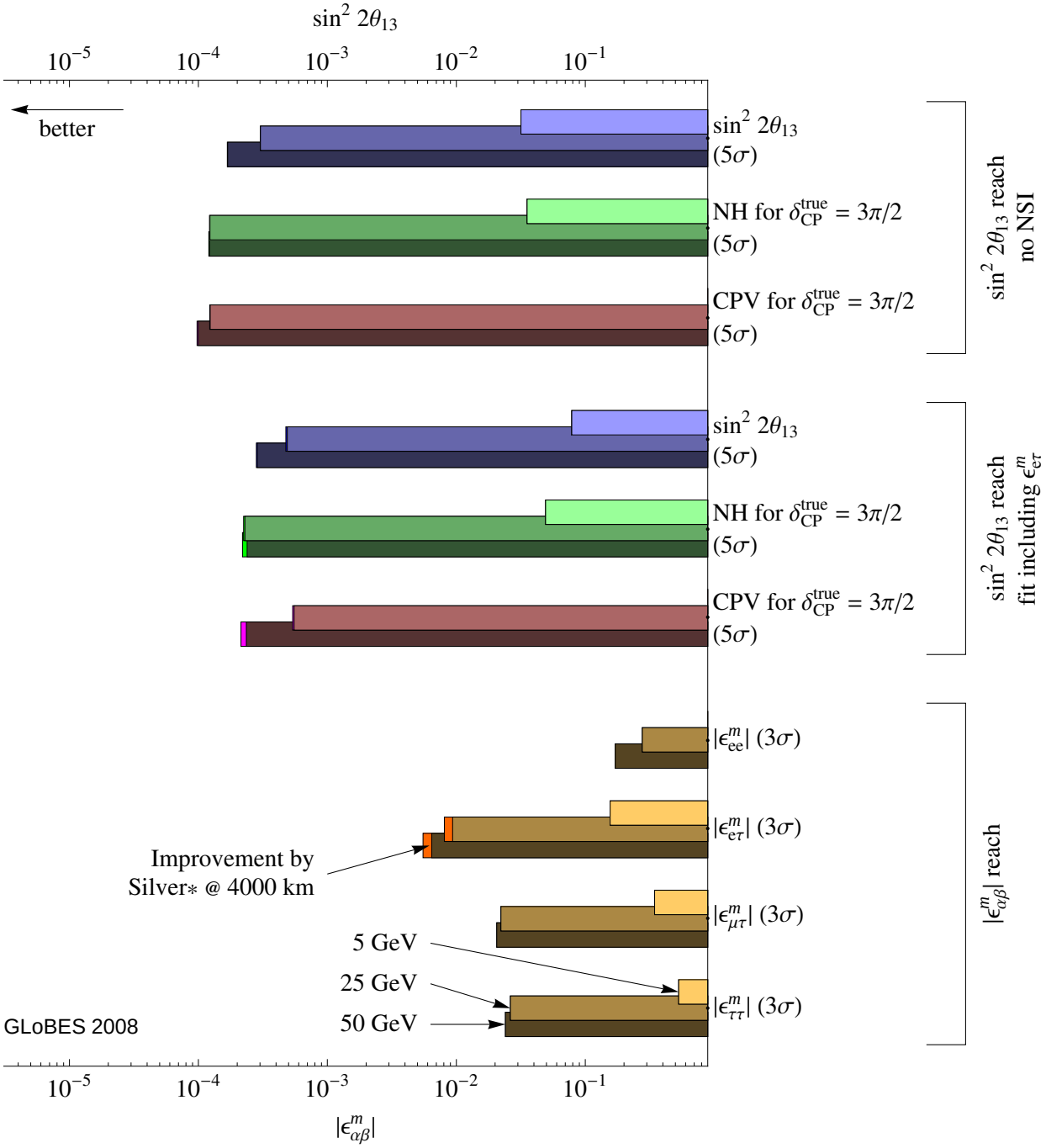


Figure 11: Summary of the Neutrino Factory performance with and without the presence of non-standard interactions. The IDS-NF setup with two MIND detectors at $L_1 = 4\,000$ km, $L_2 = 7\,500$ km was used, and the "true" parameter values $\sin^2 2\theta_{13} = 0.001$ and $\delta_{\rm CP} = 3\pi/2$ were assumed. The plot shows that sensitivities are poor at $E_\mu = 5$ GeV (light bars), but increase dramatically at $E_\mu = 25$ GeV (medium light bars). The benefit from increasing $E_\mu$ further to 50 GeV (dark bars) is only marginal, as is the benefit from including a silver channel detector. Figure taken from [57]; see that paper for details.

thorough study of the impact of $\nu_\mu \to \nu_\tau$ data is lacking. We do not expect, however, these data to have a striking impact on the sensitivity, due to the unitarity of the PMNS matrix in models in which only NSI in matter are considered.

#### 2.2.3.5 Sterile neutrinos

Even though sterile neutrinos no longer receive as much attention nowadays as before the publication of the MiniBooNE results, they are still a viable possibility, motivated by the fact that neutral singlet sterile neutrinos ($\nu_s$) appear in many models of new physics. If the $\nu_s$ are light, the neutrinos produced in the Neutrino Factory may have a small admixture of $\nu_s$, while heavy $\nu_s$ (such as right-handed Majorana neutrinos in type-I see-saw models) would manifest themselves in the form of a non-unitary mixing matrix for the light neutrinos.

In the case of one light $\nu_s$, a recent study [61] shows that the $\nu_\mu \to \nu_\tau$ appearance channel (mostly disregarded up to now; see, however, reference [62]), measured with a magnetized ECC, is extremely important when combined with $\nu_\mu \to \nu_\mu$ to measure some of the parameters of the model and in particular some of the new CP-violating phases. On the other hand, the silver channel, $\nu_e \to \nu_\tau$, is only of limited impact when added to the golden channel, $\nu_e \to \nu_\mu$, although it is useful to solve some of the many degeneracies in the parameter space.

A criticism of the use of the magnetized ECC to study the $\nu_\mu \to \nu_\tau$ channel is that the scanning load could be too high for this analysis to be realistic. However, it has been found that the scanning load for an emulsion detector at $L > 1\,000$ km is not huge: O(500) events per kton per year with a $2 \times 10^{20}$ flux are expected, for perfect efficiency. Adding a similar number of background events, this scanning load is compatible with extrapolation for present capabilities.

Notice that for standard three-family oscillation and in models with NSI in propagation, due to the unitarity of the PMNS matrix, a good knowledge of the golden and the disappearance channels (both studied at MIND) should be enough to explore the whole parameter space. This, however, is not the case in models in which the $3 \times 3$ PMNS matrix is not unitary. In sterile neutrino models, for example, since we are not able to study the $\nu_\mu \to \nu_s$ appearance channel(s), the information that can be extracted from the $\nu_\mu$ disappearance channel and the $\nu_\mu \to \nu_\tau$ channel are not identical. The same would happen in extensions of the Standard Model in which NSI violate the unitarity of the PMNS matrix are considered both in propagation and production.

From the analysis of reference [61] we conclude that the combination of the IDS-NF baseline setup (with two MINDs) with one or two magnetized ECC increase significantly the potential of the Neutrino Factory to measure all the parameter space of the (3+1)-neutrino model and, in particular, to increase its CP-violation discovery potential. However, it has been shown that the present design of the magnetized ECC is not optimized and that a dedicated study of the detector to look for new physics is required (see next section).

The optimal location for a long baseline $\tau$-detector to study sterile neutrinos is not yet clear. Whereas a detector the purpose of which is the study of the silver channel in the framework of

the three-family model or NSI in propagation is optimally located around the intermediate IDS-NF baseline (see the ISS final report [4] and reference [57]), it seems that to study (3+1) sterile neutrinos to put the magnetized ECC detector at the magic baseline could be more convenient. This is particularly true for searches of CP-violating signals. At the magic baseline, indeed, the standard three-family CP-violating effect vanishes, and therefore, if CP-violation is observed, this is clearly pointing out the existence of physics beyond the Standard Model (either new particles, such as sterile neutrinos, or new effective operators, such as in NSI). Notice that the $\nu_\mu \to \nu_\tau$ statistics at the magic baseline is still large (of O(500) events for 1 kton MECC with perfect efficiency and $2 \times 10^{20}$ useful muons per year).

#### 2.2.3.6 Technological options for $\tau$-detectors

The technology for tau-neutrino detection at the intermediate or the long baseline has not been fixed yet. The liquid-argon technology should be studied further, the timescale may be compatible with the time scale for the Neutrino Factory. Furthermore, the impact of systematic errors in the magnetised emulsion technique (MECC) is significant (see figure 12). In the figure, the sensitivity to two parameters of a model with three active neutrinos and one sterile neutrino (the "3+1" model) using the $\nu_\mu \to \nu_\tau$ channel is shown. The dashed gray line refers to the sensitivity to the relevant parameters that can be achieved using two 50 kton MIND detectors: one at an intermediate baseline, $L = 3000 - 4000$ km, and the second at the Magic Baseline. In the two panels, we show the sensitivity for a 50 GeV muon Neutrino Factory (left) and a 20 GeV muon Neutrino Factory (right). It is clear from the left panel that a huge increase in the sensitivity of the $\nu_\mu \to \nu_\tau$ channel is achieved if the uncorrelated systematic errors are reduced from 10% (black solid line) to 3% (green solid line). This improvement is actually much more important than an increase in the MECC detector mass from 4 kton (green solid line) to 8 kton (green dashed line).

This systematic error takes into account, in a non-detailed manner, systematic effects induced by uncertainties in the normalisation arising from the flux and the neutrino cross-sections. Both are expected to be better known after the first phase of OPERA. Moreover, the study of $\nu_\tau N$ cross-sections must be attempted with an intermediate detector. In this way, these sources of systematic uncertainty can be significantly reduced. A study of possible improvements in the sensitivity of the detector with a better design of the $\tau$-detector in the framework of NSI extensions of the Standard Model is also lacking.

#### 2.2.3.7 Conclusions and recommendations

In this section, we have discussed the potential of a MECC as part of the IDS-NF baseline setup (with two MIND detectors located at $L \sim 4000$ km and at the magic baseline), in three models: the standard three-family oscillation scenario; an extension of the SM with Non-Standard Interactions in matter; and an extension of the SM with one extra light singlet fermion (the so-called 3+1 sterile neutrino model). In the first two cases, the $\nu_\tau$ detector does not improve the poten-

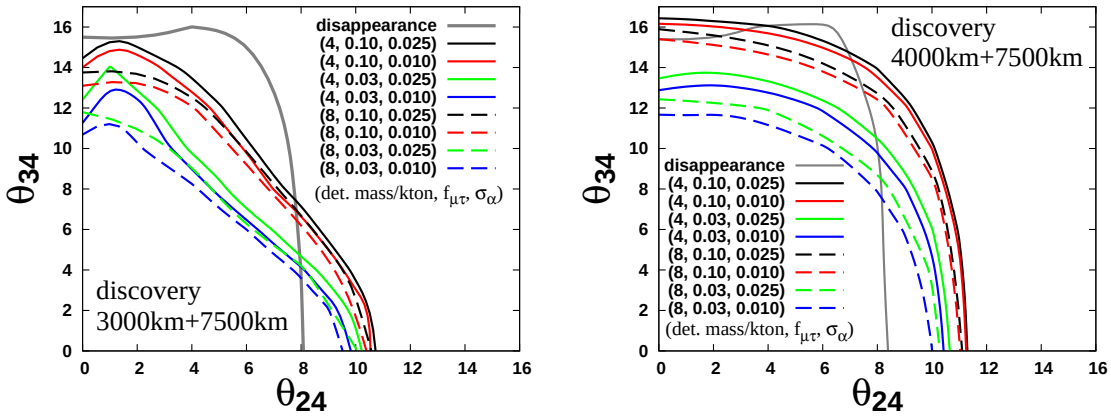


Figure 12: Left (right) panel: Dependence of the excluded region in the ($\theta_{24}$, $\theta_{34}$)-plane on the systematic errors $f_{\mu\tau} \equiv f_j$ and $\sigma_\alpha$ for the discovery channel ($\nu_\mu \to \nu_\tau$) as well as the MECC detector mass at the 50 GeV (20 GeV) Neutrino Factory, where the excluded regions are by the discovery channel only. The solid (dashed) lines assume 4 kton (8 kton) for the tau detector mass. The solid gray line, which stands for the excluded region by the $\nu_\mu$ disappearance channel, is also shown.

tial of the IDS-NF, two-MIND, baseline in the measurement of the oscillation parameters or to uncover new physics effects in neutrino oscillations. The reason is that, due to the large mixing in the $\mu$-$\tau$ sector, most effects that are present for $\tau$-neutrinos, will have a similar impact also for $\mu$-neutrinos. In these models, the $\tau$-detector could only serve as a tool for resolving parameter degeneracies. This, however, could also be achieved combining the golden and disappearance channels and data from two different baselines $L = 4\,000$ km and $L = 7\,500$ km. We must recall that a comparison of the potential of the IDS-NF baseline setup and the same setup with an additional $\tau$-detector to measure the $\theta_{23}$-octant in the standard three-family oscillation model is missing, see reference [58]. In the case of the (3+1)-sterile neutrino model, studied in reference [61], the availability of the $\nu_\mu \to \nu_\tau$ data using a magnetised ECC has been shown to be extremely important to measure the whole parameter space of the model and, in particular, to study CP-violating phases other than, $\delta$, the one present in standard, three-family, oscillations.

There may also be a physics case for $\nu_\tau$ detection if new physics should manifest itself in the $\nu_\tau$ detection process, or if non-standard couplings of $\nu_\mu$, $\nu_e$ to $\tau$ leptons or of $\nu_\tau$ to muons and electrons should exist. However, non-standard contributions to the $\nu_\tau$ detection process would require a $\nu_\tau$ detector at a long baseline (e.g. 4 000 km), while non-standard $\tau$ and $\nu_\tau$ production can be most efficiently observed in a $\nu_\tau$ near detector.

The outcome of this short review is that it is very difficult, at the present stage, to draw a final conclusion on the increase in the Neutrino Factory potential for the discovery of new physics if a $\tau$-detector is included in the IDS-NF baseline setup. It is also far from clear which detector technology would be optimal: a good knowledge of the ECC technology will be available only after some years of OPERA data taking; it is not clear if a magnetized ECC, important to increase the ECC statistics, is feasible; the liquid-argon technology has not been evaluated in detail here. Eventually, the technology to be used if an intgermediate $\tau$-detector should be built could be completely different from what has been proposed to date, exploiting the large neutrino

flux at the near detector when exposed to the Neutrino Factory beam.

In view of these arguments, we suggest that the MECC, as specified in [38], is not included in the IDS-NF baseline setup due to the absence of a compelling physics case and, given the present very preliminary status of the detector design. This does not exclude the option that a $\nu_\tau$ detector (not necessarily based on the ECC technology) is added to the Neutrino Factory setup if unexpected results from the LHC, from other neutrino experiments, or from the result of further study should provide a compelling physics case for it.

However, we think it is essential to pursue further the study of the potential of such a detector, especially in view of the fact that we do not know what new physics there may be. Having access to more flavours can only increase the discovery potential of the Neutrino Factory. Notice, finally, that if $\theta_{13}$ is determined to be large (see solar, atmospheric and MINOS results), part of the statistical problems of the $\tau$-channels may become less important. At the same time, the main motivation for a Neutrino Factory would become the search for new physics beyond the Standard Model, and therefore the option of an increased flavour sensitivity becomes extremely interesting.

### 2.2.4 Impact of systematics and location of detectors

In this short section, we discuss the impact of systematics and the location of the detectors on the performance of the baseline Neutrino Factory with a 100 kt MIND detector at the intermediate baseline. In figure 13, we show the impact of systematics on the CPV discovery potential for two different intermediate detector locations 4000 km (left panel) and 2300 km (right panel). In the right panel, the standard systematics curve from the left panel is shown as dashed curve for comparison.

The "no systematics" curves show the best performance that can be achieved if all systematic uncertainties can be controlled to within the statistical error. They represent the ideal sensitivities to be achieved at the Neutrino Factory, and consist of two contributions: systematical uncertainties such as signal and background uncertainties, and the matter density uncertainty. Therefore, the impact of the matter density uncertainty only is shown separately as intermediate solid curves. It is important for large values of $\theta_{13}$ only. In addition, the effect is larger in the left panel than in the right panel because of the longer baseline. On the other hand, the impact of the other systematic uncertainties is stronger for the shorter baseline. Note that the "standard" treatment of systematic uncertainties in this figure does not include the near detectors explicitely.

The main difference between the two intermediate baselines in the left and right panels of figure 13 is that the longer baseline (left panel) is optimised in the direction of $\sin^2 2\theta_{13}$, *i.e.*, for small values of $\theta_{13}$ [55]. The shorter baseline is better for large values of $\theta_{13}$ (right panel), as can be seen from the comparison of the lower solid and dashed curves in the right panel. In fact, the range of baselines at the intermediate baseline that do not have a strong impact on the sensitivity is relatively large, which means that specific baselines, such as CERN-Pyhasalmi,

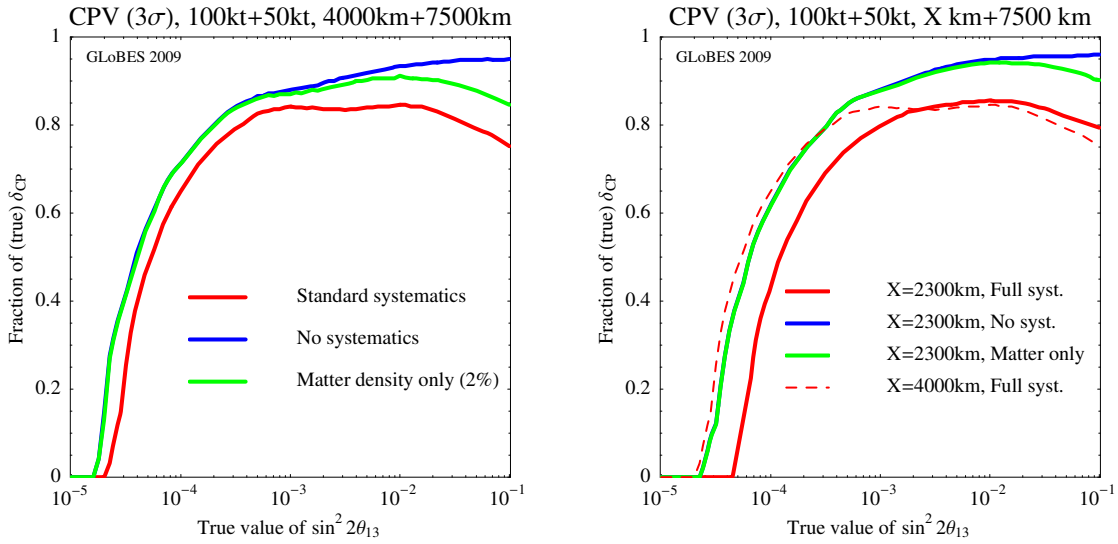


Figure 13: Impact of systematics on the CPV discovery potential for two different intermediate detector locations 4000 km (left panel) and 2300 km (right panel). In the right panel, the standard systematics curve from the left panel is shown as dashed curve for comparison.

could be used without tremendous trade-offs even for small $\theta_{13}$; see, for example, figure 5 in reference [57]. Indeed, somewhat shorter baselines than 4000 km are beneficial for intermediate $\sin^2 2\theta_{13} \simeq 10^{-2}$, whereas for very small $\theta_{13}$, 4000 km performs better; see, for example, figure 8 in reference [63] in the context of the staging discussion, where one would have information on $\theta_{13}$ from earlier phases of operation on which to base such a decision.

Note that one can also show that the very long baseline can be varied in a relatively wide baseline range between without large loss of sensitivity [64]. This very long baseline range reduces somewhat for shorter intermediate baselines, see figure 5 in reference [57], which means that the actual configuration of the two baselines has to be taken into account to judge the final sensitivity. Such configurations will be given by the geography using specific laboratories and possible detector sites.

## 2.3 Neutrino Factory in stages?

In this section, we discuss whether the Neutrino Factory can be reasonably be built in stages, such as starting with a low energy version and then upgrading the energy and adding detectors at more distant baselines. In addition, the combinations of the initial, low-energy, Neutrino Factory with the final 'high energy' (the IDS-NF baseline) Neutrino Factory. For details, see reference [63].

### 2.3.1 Large $\theta_{13}$ ($\theta_{13}$ discovered by next generation of experiments)

Here we discuss the options for large $\theta_{13}$, $\sin^2 2\theta_{13} \gtrsim 0.01$, such that will be observed at the next generation of experiments [65]. In this case, the value of $\sin^2 2\theta_{13}$ will be known at the time the facility is built, the optimisation must be performed accordingly. We show in figure 14 the baseline optimisation for a low-energy Neutrino Factory (LENF, left panel) and high energy Neutrino Factory (HENF, right panel) as a function of the source-detector baseline. The luminosity corresponds to the IDS-NF baseline set-up with all muons injected in one storage ring, and a total running time of ten years. The HENF uses $E_\mu = 25$ GeV and a 50 kt MIND detector, whereas the LENF uses $E_\mu = 4.12$ GeV and a 20 kt (fiducial mass times efficiency) TASD. The value of $\sin^2 2\theta_{13} = 0.04$ is chosen as an example. For the LENF (left panel), the optimum performance for CPV (thin curves) will be reached at around 1000 km. Without the platinum channel, slighly longer baselines are preferable to measure the mass hierarchy (thick curves). With the platinum channel, the optimal baseline window is about 500 km to 1500 km, and the absolute performance at the peak can be significantly improved. For the HENF (right panel), the optimal baseline window without any upgrades is between about 2000 km and 4000 km. It somewhat depends on the matter density uncertainty. As an upgrade option, the TASD may be used as an off-axis detector (OAD) at an off-axis angle 0.55° in the same beam, leading to the same spectrum as the LENF spectrum. In this case, the platinum channel may be used in the OAD, in just the same way as in the LENF. Obviously, using this option the fraction of $\delta_{\rm CP}$ increases, beyond that of the LENF, to 90%, and the baseline window for optimal performance becomes rather wide. This option may be interesting if searches for new physics point towards higher muon energies. However, the virtues of the LENF for large $\sin^2 2\theta_{13}$ are still needed. In this case, the baseline can be chosen relatively freely to match the new physics requirements.

### 2.3.2 Small $\theta_{13}$ ($\theta_{13}$ not discovered by the next generation of experiments)

If $\sin^2 2\theta_{13}$ is not found by the next generation of experiments, it may be searched for in a step-by-step fashion by the Neutrino Factory. We split the Neutrino Factory operation into phases, where the strategy in each phase can be adjusted depending on the outcome of the preceding phase. A plausible scenario may be the following, each phase lasting five years see figure 15) [63]:

**Phase I: LENF** with TASD optimized for $\sin^2 2\theta_{13}$ discovery, i.e., $L \sim 900\,$km. In this case, the $\sin^2 2\theta_{13}$ discovery reach exceeds that of the next generation of experiments by about one order of magnitude;

**Phase II: Energy upgrade.** If $\sin^2 2\theta_{13}$ was not discovered in phase I, the $\sin^2 2\theta_{13}$ discovery reach could be significantly improved by a muon energy upgrade, together with new 50 kt MIND detector and storage ring. If $\sin^2 2\theta_{13}$ was discovered in phase I, the mass hierarchy and CP-violation could be measured over a large part of the parameter space. In this case, the measured value of $\sin^2 2\theta_{13}$ should used for the baseline re-optimisation. For example, for $\sin^2 2\theta_{13} \simeq 0.01$, baselines around 3000 km are preferable, whereas for smaller $\sin^2 2\theta_{13}$,

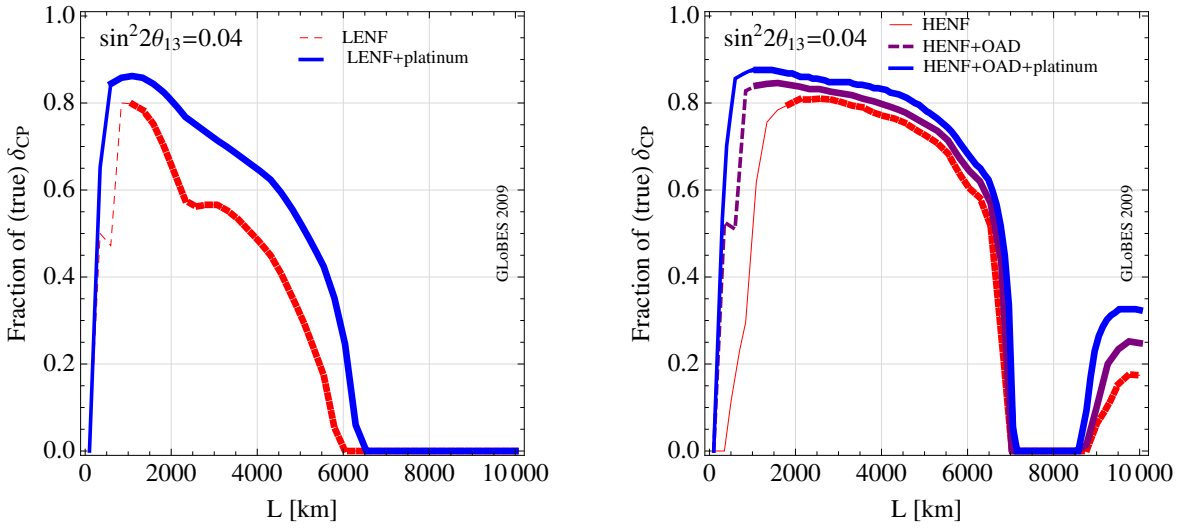


Figure 14: Fraction of $\delta_{\rm CP}$ for which CPV will be discovered as a function of baseline $L$ for the LENF (left panel) and HENF (right panel); $3\sigma$ CL. The different curves show different upgrade options: off-axis TASD (OAD) and platinum channel. The thick curves give the baseline range where also the mass hierarchy can be determined for *any* $\delta_{\rm CP}$ at the $3\sigma$ confidence level. Here $\sin^2 2\theta_{13} = 0.04$, $5 \cdot 10^{21}$ useful muons, a normal hierarchy and a 2% of the matter density uncertainty are assumed. Figure taken from reference [63].

baselines around 4000 km are better. The combination of the world data with the phase I Neutrino Facory data turns out to be synergistic; and

**Phase III: Detector upgrade or magic baseline.** Depending on the value of $\theta_{13}$ determined in phases I and II, it turns out that upgrading the MIND detector to 100 kt (dark/blue dashed curves in figure 15) or adding a second baseline (dark/blue solid curves in 15) is the better option. Note, however, that the magic baseline may be preferred for other reasons, such as new physics searches (see, *e.g.*, references [57, 66]).

In summary, the combination between elements of the LENF and HENF may be plausible in realistic scenarios, especially for small values of $\sin^2 2\theta_{13}$.

## 2.4 LENF

The low-energy Neutrino Factory (LENF) has recently come to the fore and so there is considerably less detail in the understanding of its performance and optimisation. Below we present the results obtained so far, in the full understanding that more detailed results are require before the IDR is completed.

The low energy Neutrino Factory with a baseline of $\sim$ 1000 km was first proposed in [67]. It was motivated by the fact that at this baseline, the oscillation spectrum at energies below $\sim$ 5 GeV is very rich, potentially allowing very precise measurements of the unknown oscillation parameters ($\theta_{13}$, $\delta$ and the mass hierarchy) to be made. Since then, developments in the accelerator and detector designs have enabled the experimental simulations to be refined and

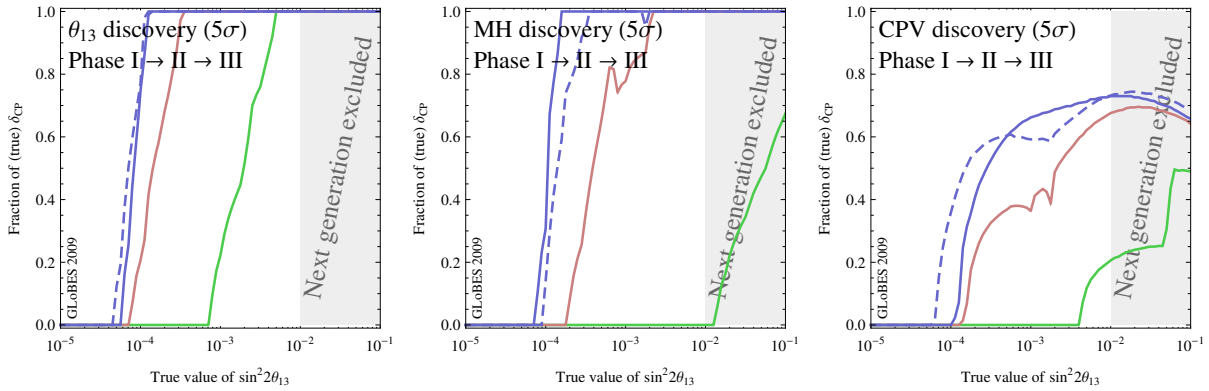


Figure 15: $\theta$, MH, and CP discovery reaches for a neutrino factory in three phases: Phase I (light gray/green) is a low energy neutrino factory with a magnetized TASD, phase II (medium gray/red) adds an energy upgrade with a MIND at the 4000 km baseline, and phase III (dark gray/blue) includes another (magic) baseline (solid curves) or a detector upgrade at the 4000 km baseline (dashed curves). $5\sigma$ confidence level. Figure taken from reference [63].

detailed optimisation studies to be performed [67]. The key finding was that, given sufficiently high statistics, an optimised low-energy Neutrino Factory can have excellent sensitivity to the standard oscillation parameters, competitive with the baseline, high energy Neutrino Factory for large $\theta_{13}$ ($\sin^2 2\theta_{13} \gtrsim 10^{-3}$). The sensitivity to the size of the integrated neutrino flux was recently explored in [63].

For the first time, the possibility of observing the platinum channels ($\nu_\mu \to \nu_e$ and $\bar{\nu}_\mu \to \bar{\nu}_e$) in addition to the golden channels ($\nu_e \to \nu_\mu$ and $\bar{\nu}_e \to \bar{\nu}_\mu$) [68] was considered, as there are early indications that certain detector technologies may be able to detect and distinguish $e^-$ and $e^+$. It is found that the complementarity between these platinum and golden channels can be of great benefit if statistics are limited, improving the sensitivity to the standard oscillation parameters. Current ongoing work [69] also indicates that the addition of these platinum channels is vital at the LENF in order to resolve the degeneracy between standard oscillation parameters and neutrino matter non-standard interactions.

Full details of the proposed setup can be found in [67]. We studied a setup having a baseline of 1 300 km with a beam capable of delivering $1.4 \times 10^{21}$ useful muon decays per year [70] for 5 years per polarity. For the detector we considered two possibilities: a 20 kton totally active scintillating detector (TASD) [43] and a 100 kton liquid argon (LAr) detector [71], both of which would be magnetised. These detectors would be capable of detecting and identifying the charges of both electrons and muons, providing access to multiple oscillation channels: the $\nu_\mu$ ($\bar{\nu}_\mu$) disappearance channels, as well as the golden and platinum channels.

To simulate the detectors we made the assumptions described in [67]. The main points are that for the TASD we assume a detection efficiency of 90% (47%) above 1 GeV for $\nu_\mu$ and $\bar{\nu}_\mu$ ($\nu_e$ and $\bar{\nu}_e$,), with backgrounds of $10^{-3}$ ($10^{-2}$). The energy resolution is assumed to be 10% for all channels. For the LAr detector we assumed an efficiency of 80% for all channels, then considered a range of values for the remaining parameters to accommodate for the present uncertainty in

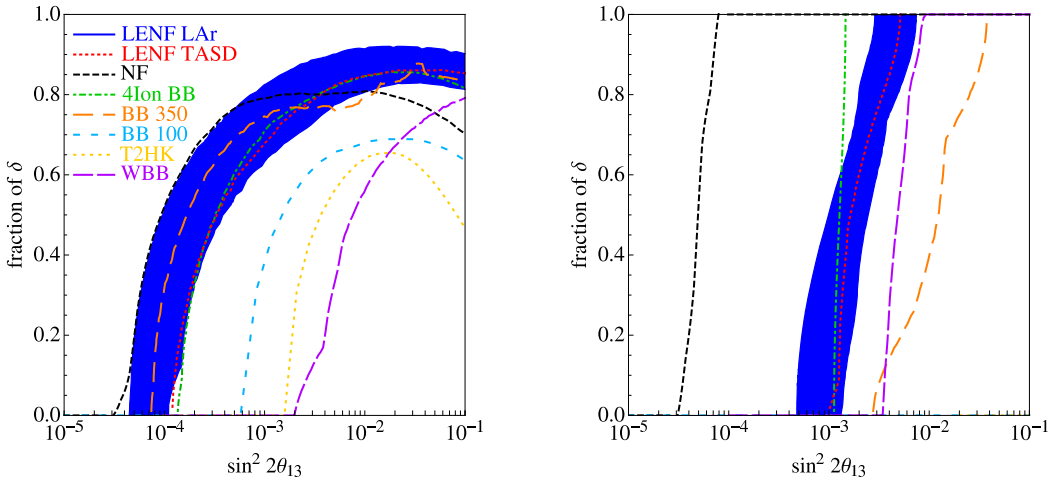


(a) CP discovery potential

(b) Hierarchy sensitivity

Figure 16: Comparison of the $3\sigma$ a) CP discovery potential and b) hierarchy sensitivity of the low energy Neutrino Factory with a 20 kton TASD and 100 kton LAr detector, the baseline, high energy Neutrino Factory, $\beta$-beams, T2HK, and the wide-band beam.

LAr technology. The conservative values were taken from [72] (reported in [73]): 20% energy resolution, and backgrounds of $5 \times 10^{-3}$ (0.8) on the $\nu_\mu$ ($\nu_e$) channels. For the optimisic LAr detector scenario we assumed the same values as for the TASD.

We have used the GLoBES software package [74,75] to simulate the experimental configuration, presenting the $3\sigma$ CP discovery potential and sensitivity to the mass hierarchy in figure 16 as a function of $\sin^2(2\theta_{13})$ in terms of the CP fraction. In addition to the low-energy Neutrino Factory with both a LAr detector (blue band) and a TASD (red line), we also show the sensitivities of the baseline, high energy Neutrino Factory [4] (black line), various $\beta$-beams (green [76], orange [77, 78], blue [79] lines), T2HK [80] (yellow line) and the wide-band beam [81] (purple line). In these simulations we used the same oscillation parameters as in [38], and assumed a normal hierarchy scenario. It can be seen that a low energy Neutrino Factory with an optimistic LAr detector has sensitivity to CP violation comparable to that of the high energy Neutrino Factory, for all values of $\theta_{13}$. A TASD also performs competitively for $\sin^2(2\theta_{13}) \gtrsim 10^{-3}$. The sensitivity to $\theta_{13}$ (not shown here, see [67] for details) is also very good – only the baseline, high energy Neutrino Factory and the $350\gamma$ $\beta$-beam scenarios perform better. The sensitivity to the mass hierarchy is not as competitive, but is still an order of magnitude better than that of the wide-band beam which uses the same 1 300 km baseline. This remarkable performance can be attributed to the combination of high statistics and good background rejection, together with an intermediate length baseline which allows for a clean measurement of CP violation whilst still allowing for the mass hierarchy to be determined for $\sin^2(2\theta_{13}) \gtrsim 10^{-3}$.

Neutrino-matter non-standard interactions (NSI's) can be parameterised by the parameters $\varepsilon_{\alpha\beta}$ (see, for instance, reference [57, 82]), which describe the rate of the transition $\nu_\alpha \to \nu_\beta$. The golden and platinum channels have leading order sensitivity to the parameters $\varepsilon_{e\mu}$ and

$\varepsilon_{e\tau}$ [57, 82].

Here we show the sensitivity of the low energy Neutrino Factory with a 20 kton TASD to the neutrino matter NSI parameter $\varepsilon_{e\mu}$, simulated by the MonteCUBES software package [83]. We illustrate how the platinum channel enhances the sensitivity of the experiment, by showing the 68%, 90% and 95% allowed regions in the $\theta_{13} - \varepsilon_{e\mu}$ plane, both with the platinum channel (red solid lines) and without (blue dashed lines), for the case of $\varepsilon_{e\mu} = 0$ (figure 17a) and $\varepsilon_{e\mu} = 0.01$ (figure 17b). The current bound on $\varepsilon_{e\mu}$ is $O(1)$ [84]. Figure 17a shows that the low energy Neutrino Factory could improve upon this and figure 17b shows that $\varepsilon_{e\mu} = 0$ could be excluded at $\sim 90\%$ confidence if $\varepsilon_{e\mu} \sim 0.01$.

We find that this sensitivity is not affected much by statistics [69], in contrast to the case of standard oscillations. This is an indication that if NSI's are present, the experimental sensitivity is not limited by statistics, but by the fact that it is not possible to distinguish between the standard and NSI parameters. Unless this degeneracy can be resolved, for instance by the inclusion of the complementary platinum channels, then the sensitivity to both standard oscillation and NSI parameters will be severly limited.

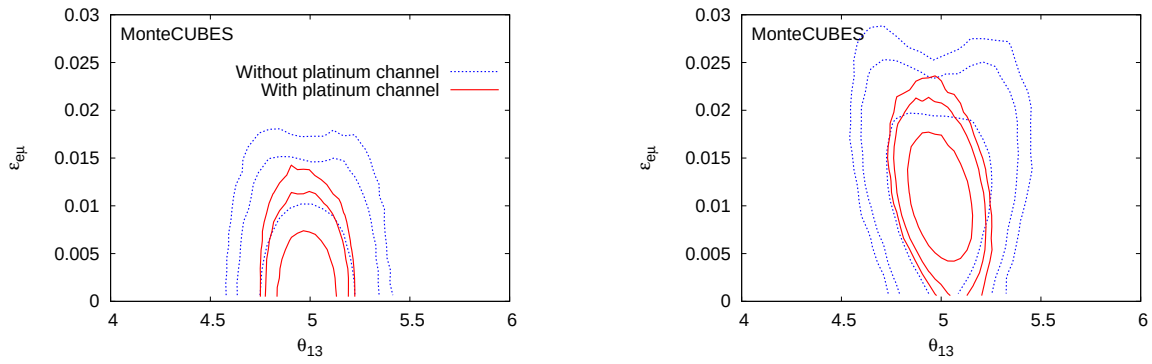


(a) $\varepsilon_{e\mu} = 0$ (b) $\varepsilon_{e\mu} = 0.01$

Figure 17: 68%, 90% and 95% allowed regions in the $\theta_{13} - \varepsilon_{e\mu}$ plane, with and without the platinum channel, for true values of a) $\varepsilon_{e\mu} = 0$ and b) $\varepsilon_{e\mu} = 0.01$.

An optimized low energy Neutrino Factory using either a TASD or LAr detector has excellent sensitivity to $\theta_{13}$ and the CP violating phase, $\delta$, for $\sin^2(2\theta_{13}) > 10^{-4}$, and to the mass hierarchy for $\sin^2(2\theta_{13}) > 10^{-3}$. The unique combination of golden and platinum channels helps to maximise the experimental sensitivity to these parameters if statistics are limited, and to resolve the degeneracy between the standard oscillation parameters and those which describe neutrino matter non-standard interactions.

## 2.5 Theory of neutrino masses and mixings

In the section we review the developments on the theory front. Note, that none of these issues is peculiar to the IDS-NF and that the theory community is actively persuing these, without being prompted to do so by the PPEG.

### 2.5.1 Connection to charged leptons flavour violation

The most sensitive probes of physics at the Terascale and beyond include searches for very rare or predicted-to-be-forbidden processes. Among these, searches for charged lepton flavour violation (cLFV) are especially promising. Some of the reasons for optimism include:

1. In the neutrino sector, lepton flavour is known to be violated. Furthermore, the lepton-flavour violating parameters are quite large, unlike the mixing observed in the quark sector. Furthermore;
2. We know that the Standard Model must be augmented somehow in order to accommodate neutrino masses. Searches for cLFV provide some of the best diagnostic tools for distinguising different new physics scenarios apart – charged leptons are leptons too!
3. In the near and intermediate future, we expect to explore cLFV well beyond current experimental bounds. finally;
4. The Neutrino Factory facility contains all of the necessary ingredients to host a very powerful experiment aimed at searching for cLFV with muons. Such searches could ultimately expand our sensitivity to $\mu \to e$ conversion in nuclei by seven or eight orders of magnitude with respect to current constraints [85].

In the following, we briefly review some of the points highlighted above and discuss recent progress in the study of CLFV processes.

The discovery of neutrino oscillations revealed that the Standard Model (SM) needs to be augmented somehow in order to accommodate massive neutrinos. Neutrinos also reveal that leptons mix and hence that individual lepton-flavour numbers are not conserved. The discovery of neutrino oscillations implies that, necessarily, cLFV must occur at some order in perturbation theory. Unfortunately, we don't know what the prediction of the neutrino-mass-enhanced SM ($\nu$SM) is since we don't have enough information to uniquely determine the $\nu$SM Lagrangian (we don't even know what are the relevant light degrees of freedom). In some well-motivated $\nu$SM, the expectation is that cLFV occurs at fantastically small rates. For example, if the neutrinos are massive Dirac fermions one can easily estimate $B(\mu \to e\gamma) \sim 10^{-54}$ while the normalised $\mu \to e$ conversion rate is several orders of magnitude larger (but still extremely small). The reason for the small number is easy to understand. cLFV are flavour-changing neutral-current processes and hence GIM suppressed. In the neutrino sector, GIM suppression is very efficient – $B(\mu \to e\gamma) \propto (\Delta m^2_{ij}/M^2_W)^2$ where $\Delta m^2_{ij}$ are the neutrino mass-squared differences and $M_W$

is the $W$-boson mass. Another way of understanding why in many minimal versions of the $\nu$SM cLFV phenomena are incredibly rare is that, in many scenarios, flavour-violation in the lepton-sector vanishes when the neutrino masses vanish (or are degenerate). Hence, the rate for LFV phenomena depends on neutrino mass-squared differences (as is the case for neutrino oscillations).

The discussion above does not apply to all manifestations of the $\nu$SM. Concrete counter examples have been identified in the literature[1] [86–90], and include different versions of the see-saw mechanism, and scenarios where small neutrino masses are a consequence of neutrinos propagating in extra dimensions. The main message is clear: significant progress in determining the $\nu$SM will require "help" from searches for cLFV.

Often independent from (or only indirectly dependent on) the mechanism behind neutrino masses, it is widely expected that new physics at the weak scale will mediate cLFV. Turning the picture around, searches for cLFV severely constrain new physics at the weak scale and usually restrict it to be either heavy ($M_{\rm new} \gg 1$ TeV) or very "flavour conserving." Recent studies or reviews in the literature associated to different well-motivated new physics scenarios include [91–97]. Different scenarios imply different predictions but, in general, cLFV tends already to severely constrain several well motivated scenarios of physics beyond the SM usually pushing them towards flavour-conserving regions of their respective parameter spaces. In many cases, cLFV is predicted to be "just around the corner." Finally, the phenomenology of different cLFV processes and what they can teach us about the nature of the new physics have received some attention recently, see, for example, [98–102]. This is especially true if one can perform precision measurements of different cLFV processes, including $\mu \to eee$ and $\mu \to e$ conversion in different nuclei. Also flagged were the measurement of correlations among the different decay electrons in $\mu \to eee$ and measurements of the polarisation of final state electrons or positrons in $\mu \to e$ conversion and $\mu \to eee$. Whether the latter are possible experimentally is, we believe, still the subject of debate and clearly requires a lot more investigation.

Experimentally, the MEG experiment searching for $\mu^+ \to e^+\gamma$ decays at PSI is currently taking data and has released its first results [103]. These are competitive with the current world average [2]. A next round of results is expected this calendar year. Over the last year or so, a couple of proposals have solidified both at Fermilab [104] and J-PARC [105]. Both are experimental setups that will aim to be sensitive to $\mu \to e$ conversion in nuclei assuming that the normalised rates are not smaller than $10^{-16}$ or so. It is expected that the next and next-next generation experiments will be of the $\mu \to e$ conversion type for a couple of reasons. One is that it appears to be very hard to build experiments that will reach beyond the ultimate reach of MEG [85]. We don't anticipate to hit any such wall with $\mu \to e$ conversion searches anytime soon. The second is that one can show that a $\mu \to e$ conversion experiment is more sensitive to cLFV physics than a search for $\mu \to e\gamma$ if the sensitivity of the $\mu \to e$ conversion experiment is about 100 times better than that of the $\mu \to e\gamma$ experiment. This result is (almost) model independent and the new physics sensitivities are similar in the "worst-case" scenario. There

[1] We have tried to concentrate on references that have been published within the last 18 months.

are models in which the normalised $\mu \to e$ conversion rate is several orders of magnitude larger than the branching ratio for $\mu \to e\gamma$. Discussions of this fact can be found in [85, 104]. The "odd-man-out" is the search for $\mu^+ \to e^+e^-e^+$. There are no searches for $\mu^+ \to e^+e^-e^+$ on the horizon, but there are discussions taking place at different places in order to ascertain whether one can search for $\mu^+ \to e^-e^+e^-$ decays significantly beyond the current experimental upper bound. It is important to note that there are new physics scenarios where $\mu^+ \to e^-e^+e^-$ is the only cLFV decay within experimental reach in the foreseeable future (see, for example, [106], for concrete examples).

cLFV phenomena involving tau-leptons are also important and being actively pursued by the B-factories. For some recent results see [107–112]. In some models, tau cLFV phenomena may be more common that those involving muons, sometimes compensating for the much larger experimental upper bounds (see, for example [97] for a concrete, very recent, example). Current bounds on the branching ratio of cLFV tau decays are approaching $10^{-8}$. It is expected that sigificant improvement (one or two orders of magnitude) will only become possible with the advent of Super B-Factories.

### 2.5.2 Summary of the NuFlavour 09 workshop

On 8–10 June 2009, the workshop "Flavour physics in the era of precision neutrino experiments" at Coseners House, Abingdon, UK, focussed on a critical review of the physics case for neutrino physics and long baseline neutrino oscillations from a theoretical perspective [9]. Neutrino experiments are part of a wide particle-physics program and their complementarity and synergy with the energy frontier (future collider) experiments and other flavour physics experiments should be clarified and exploited. The topics which were discussed included:

1. Lepton flavour violation (LFV) from grand unified theory (GUT) see-saw models and from TeV see-saw models;
2. Leptogenesis in the context of neutrino mass models;
3. A theoretical perspective on lepton flavour physics at the TeV scale within supersymmetric (SUSY) models and extra-dimension models;
4. Interplay between neutrino masses and other phenomenological signatures;
5. Neutrino physics and cosmology/astroparticle physics; and finally
6. Performance indicators in long baseline neutrino oscillation experiments.

While the Standard Model (SM) has been extremely successful in explaining the precision data obtained in collider and flavour-physics experiments, evidence of physics Beyond the SM (BSM) has been obtained in the recent past in the lepton sector. In particular, neutrino oscillations imply that neutrinos have mass and that they mix. This phenomenon cannot be explained within the context of the SM and constitutes the first indications of a theory BSM.

New questions in neutrino physics have arisen and need to be addressed in the future:

- What is the nature of neutrinos – are they Dirac or Majorana particles?
- What are the values of the mixing angles;
- what are the absolute values of neutrino masses;
- Is there CP-violation in the lepton sector; and
- Is the standard, 3-neutrino mixing scenario correct?

These questions will be addressed experimentally in a wide neutrino experimental program which includes neutrino oscillation experiments, direct mass searches, neutrinoless double-beta-decay experiments and from cosmological and astrophysical observations. This is the information which is needed in order to understand the origin of neutrino masses and of flavour in extensions of the Standard Model.

#### 2.5.2.1 LFV from GUT see-saw models and from TeV see-saw models

See-saw models [113–116] provide a natural solution to the smallness of neutrino masses and they can be embedded in Grand Unified Theories (talk by G. Ross) or emerge at the TeV scale, being testable at the LHC in the forecoming future (talk by E. Ma). All these models need also to account for the low-energy flavour structure (talk by M. Schmidt). A series of theoretical questions emerged at the meeting:

- Is it possible to discriminate between GUT and TeV-scale see-saw models?
- How do these models inscribe into a more general theory?
- Where does the smallness of neutrino masses come from, and does it require fine-tuning anywhere?
- How can flavour mixing be implemented?
- Is it possible to define some "benchmark" scenarios? If so, which ones?
- Is it possible to have arguments for the precisions required for $\theta_{13}$, $\delta$, and the Majorana phases? and
- What information on the origin of neutrino masses can be obtained from the mass hierarchy measurement?

These questions were addressed in the discussion session lead by M. Frigerio. It was mainly emphasised that there are two aspects which need to be studied: the origin of neutrino masses and the rationale for the leptonic flavour structure.

In GUT-scale see-saw models, neutrino masses arise from the interaction between SM neutrinos and heavy Majorana particles $N$. Due to the very heavy scale of $N$, it is not possible to test these models directly. However there are other signatures which can be searched for and could be used to get some information on the underlining mechanism. Lepton-flavour violating charged-lepton decays are predicted to be close to present bounds for supersymmetric models due to the running of the supersymmetric scalar masses down to the see-saw scale or to misalignment of soft terms in flavour models with familons. The rate for these processes depends very strongly on the SUSY-breaking pattern and on the SUSY parameters and the discoveries at the LHC will play a crucial role in testing these models.

On the other hand, there are see-saw models in which the new physics is at the TeV scale and therefore testable in present and future colliders. In order to suppress neutrino masses and have them compatible with the measured values, in general, a new symmetry needs to be imposed: it protects neutrino masses and in many cases guarantees a neutral particle to be stable and to constitute a viable dark matter candidate. There are well-motivated TeV see-saw models in which neutrino masses are generated with no fine-tunings. Despite the relatively low energy of the new particle, it might be difficult to test these models because the mechanism responsible for the smallness of neutrino masses also suppresses lepton flavour violating processes, lepton-number violating processes at colliders and non-unitary effects. In the presence of additional gauge interactions or in type-II see-saw models, signals can be found in colliders but the connection between these observables and neutrino masses is weakened.

Three contributed talks were also given by A. Adulpravitchai on Non-abelian Discrete Flavour Symmetries from $T^2/Z_N$ Orbifolds, by D. Hernandez on the Minimal Flavour Seesaw Models and by M. Satriawan on Possible mechanism for generating a very small Dirac neutrino mass.

#### 2.5.2.2 Neutrino physics and the cosmology/astroparticle physics complementarity

The bath of relic cosmological neutrinos, which decoupled at $T \sim 1$ MeV, affects the evolution of the Universe, in particular Big Bang Nucleosynthesis, large scale structure formation, and the Cosmic Microwave Background and allows neutrino masses, the number of neutrinos and the type of neutrino interactions to be constrained (talk by S. Hannestad) [117]. In the discussion session lead by P. Di Bari, various issues were discussed, in particular those related to the comparison between cosmological bounds and terrestrial ones, the estimation of systematic errors in the measurement of neutrino parameters from cosmological observations, and the impact of a non-standard evolution of the early Universe.

Cosmological observations constrain the number of neutrinos and the values of neutrino masses in the Early Universe. A combination of WMAP3+SDSS-LRG+SNI-A data allows to the number of neutrinos to be $N_\nu = 3.9^{+2.0}_{-1.6}$ at 95% C.L. [118] and the case of no neutrinos is excluded at more than $5\sigma$. Due to their gravitational effects, neutrinos have a strong impact on the growth of large scale structures and it is possible to put strong bounds on neutrino masses, with a sensitivity comparable with laboratory experiments. At present one has $\sum m_\nu < 0.2$–1 eV depending on the analysis (see for example [117]). Future observations will improve these

bounds and will constitute an important source of information on neutrino masses. Combining it with results from other experiments such as direct mass searches or neutrinoless double-beta decay, it might be possible to get further insight into the evolution of the Universe and even test whether neutrinos are Dirac particles, if cosmology finds large values for $m_\nu$ while no signal is found in neutrinoless double-beta decay. Sterile neutrinos are the leading candidate for warm dark matter and can be tested in x-ray searches from dark matter overdensities, as the centre of the galaxy or nearby dwarf galaxies (talk by A. Kusenko). Neutrino mixing cannot be tested with cosmology, but supernova neutrino observations could provide important information and potentially test small values of $\theta_{13}$. At the moment theoretical uncertainties in the evolution of the flavour compositions of neutrinos from the core to the neutrinosphere are still large and need to be resolved to be able to extract this information.

#### 2.5.2.3 A theoretical perspective on lepton flavour physics at the TeV scale within i) SUSY models ii) extra-dimension models

The origin of neutrino masses requires new particles and interactions which need to be embedded in a wider scheme to solve the hierarchy problem and explain the pattern of masses and mixing. Possible scenarios are supersymmetric and little Higgs models and models with extra dimensions. One needs to consider how these models fit into a wider particle physics theory and whether there are any model-independent signatures. These issues were discussed by A. Santamaria.

Generically, the embedding of neutrino mass models in a wider scheme induces new signatures such as LFV processes at low energy, for example $\mu \to e\gamma$, $\mu - e$ conversion and $\tau \to e\gamma$. In non-supersymmetric models which embed the see-saw mechanism, lepton-flavour violating (LFV) charged-lepton decays such as $\mu \to e + \gamma$, $\tau \to \mu + \gamma$, $\tau \to e + \gamma$, are predicted to take place with branching ratios which are strongly suppressed [119]. SUSY theories have additional sources of lepton number non-conservation (talks by S. Khalil and A. Texeira). If SUSY is broken at $M_X \gg M_R$ as, for example, in gravity-mediated symmetry-breaking scenarios, there are renormalisation group effects that generate new lepton number non-conserving couplings at low energy even if such couplings are absent at the GUT scale [120–122]. In contrast to the non-supersymmetric case, the LFV processes can proceed with rates and cross-sections which are within the sensitivity of present and proposed experiments.

Neutrino masses can also arise in supersymmetric models with R-parity violation (talk by S. Lavignac). The models can easily accommodate the measured values of neutrino masses and predict negligible rates for LFV processes. Extra-dimension models can also be at the origin of neutrino masses and typically prefer Dirac neutrinos (talks by F. del Aguila and J. M. Frere). Models with warped dimensions explain the hierarchy of lepton masses by requiring a different zero mode localization of the corresponding wave-functions on the brane. These models have specific signatures which could allow them to be distinguished from other TeV scale ones at colliders.

#### 2.5.2.4 Leptogenesis in the context of neutrino-mass models: model dependent versus model independent considerations

Leptogenesis [123] (talk by A. Abada) is one of the favoured mechanisms for the generation of the baryon asymmetry of the Universe and naturally takes place in see-saw models. In the presence of CP-violation the decays of heavy Majorana neutrinos in the early Universe produce a lepton asymmetry which is partially washed-out and converted into a baryon asymmetry by sphaleron processes [123–128]. Compelling questions arise (discussion session lead by E. Nardi):

- Under what conditions can a connection between low and high energy CP violation be established?
- Is it obvious that leptogenesis takes place if a low energy CP violation and lepton-number violation is observed?
- Can one get additional information from an observation of LFV?

In many cases it might possible to relate the low-energy parameters which can be measured in neutrino experiments with the ones responsible for the baryon asymmetry and test the hypothesis of leptogenesis as the source of the matter-dominated Universe. In see-saw type I models, by counting the parameters one finds that there are six independent CP-violating phases at the see-saw scale which can play a role in leptogenesis. In teh absence of flavour effects, it might be possible to have leptogenesis even if there is no CP-violation at low energy and, in general, there is not a direct connection between low energy parameters and the high energy ones. This link arises if a theory of flavour is present, which explains the observed mixing pattern and reduces the number of free-parameters. In this case it is possible to predict the baryon asymmetry from a measurement of light neutrino masses and mixing. For masses of the heaviest neutrino smaller than $10^{12}$ GeV, flavour effects play an important role [129]. In this case, generically a connection between leptogenesis and low energy CP-violating phases can be obtained in the sense that if CP-violation is found in future neutrino experiments a lepton asymmetry needs to be generated in the early Universe [130, 131]. Starting from the case of CP-violation only in the leptonic mixing matrix, the baryon asymmetry can be computed for various choices of the values of the phases. For Dirac CP-violation, values of $\sin\theta_{13}$ that may be reached in the future long-baseline neutrino oscillation experiments are required. Leptogenesis can also be successful in the case of dominant Majorana CP-violation which plays a role in neutrinoless double-beta decay. Leptogenesis can also take place in other see-saw models, for example see-saw type II models and in other scenarios of neutrino mass generation.

#### 2.5.2.5 Interplay between neutrino masses and other phenomenological signatures

Small neutrino masses can naturally be generated in models which implement the see-saw mechanism by introducing heavy Majorana neutrinos at very high energies through their coupling to SM neutrinos. Although these models cannot be tested directly in experiments unless

the new physics required is just above the electroweak scale, they have other signatures at low energy. The talks in this session focussed in particular on lepton flavour violation, neutrinoless double-beta decay, non-standard interactions and collider signatures of TeV scale see-saw models.

Additional sources of lepton flavour violation induce processes at low energy such as $\mu \to e\gamma$, $\mu - e$ conversion, $\tau \to e\gamma$ (talk by A. de Gouvea) at rates which could be close to present bounds. From a phenomenological perspective the observation of these processes will give an indication of the new physics scale at which LFV arises. The LHC experiments will provide information on the physics at the TeV scale and this will guide us in understanding the properties of the theory BSM. In some models the new physics required to explain neutrino masses arises at these scales (talk by T. Schwetz) and have signatures which can be tested at colliders. Additional effects can arise in neutrino oscillations due to non-standard interactions of neutrinos with matter affecting the oscillation probabilities significantly and changing them with respect to standard oscillations. Non-standard interactions can be tested in future long-baseline neutrino experiments (talk by E. Fernandez-Martinez). Neutrinoless double-beta decay can be mediated not only by light Majorana neutrino masses but also by other mechanisms such as heavy sterile neutrinos, supersymmetric R-parity violation. Once a positive signal is found, it will be critical to discriminate between the various mechanisms. S. Kom gave a contributed talk on LHC probes of SUSY neutrinoless double beta decay mechanism and C. Jackson on the issues related to understanding the mechanism of neutrinoless double beta decay with the SuperNEMO experiment. In the discussion session T. Ohlsson addressed the synergy and complementarity of these different experimental signatures in pinning down the mechanism at the origin of neutrino masses.

#### 2.5.2.6 Round table on a preliminary discussion on performance indicators in long baseline experiments

Future long-baseline neutrino-oscillation experiments play a crucial role in determining the value of the unknown mixing angle $\theta_{13}$, the type of neutrino mass hierarchy and the existence of CP-violation in the lepton sector. A rich experimental program is under consideration for the near future: conventional beam experiments (MINOS, OPERA) are already taking data, superbeams (T2K, NOvA) are under construction or at the R&D phase while even more ambitious projects such as the Neutrino Factory and beta-beams are being studied [4]. The sensitivity of the various setups is studied in detail. T. Li discussed the physics reach of the low energy Neutrino Factory and J. Lopez Pavon the search for 3+1 sterile neutrinos in contributed talks. It is necessary to compare the reach of different experiments in an objective way and with comparable assumptions. These issues where discussed in the round table led by K. Long. Long-baseline neutrino experiments constitute one strategy to determine neutrino parameters but other physics searches are also taking place: neutrinoless double-beta decay, charged lepton-flavour decay, other oscillation experiments and direct mass searches. All these experiments will bring different information on neutrino properties which should be combined together. It is important to establish the complementarity between these experiments and their synergy as

well as to define the priorities between these experiments from a theoretical point of view.

#### 2.5.2.7 Conclusions

With the discovery of neutrino oscillations, neutrino physics has opened a new window on the physics BSM. Various models of neutrino masses and of mixing have been proposed and the see-saw mechanism has emerged as the most natural explanation. Despite being introduced at very high scales which typically are not testable directly in future experiments or at the TeV scale, its low energy signatures such as neutrino masses and mixing, the baryon asymmetry in the leptogenesis mechanism, and lepton-flavour violating processes allow us to get information on the physics BSM.

# 3 Accelerator Working Group

## 3.1 Overview

The baseline accelerator facility (see figure 18), a development of that described in [132], provides $5 \times 10^{20}$ decays per year towards each of the two distant neutrino detectors [38]. The process of creating the muon beam begins with the bombardment of a pion-production target with a 4 MW, pulsed proton beam. The target must be sufficiently heavy to produce pions copiously, yet not so large as to cause a significant rate of interaction of the secondary pions within the target material. In addition, the target must withstand the substantial beam-induced shock. The IDS-NF baseline calls for a free-flowing, liquid-mercury jet operating in a solenoid-focusing, pion-capture channel. A solenoid transport channel, in which the pions decay to muons, follows the capture section. The muon beam that emerges from the decay channel must be manipulated. First, bunching and phase rotation are performed to produce a beam with small energy spread, bunched at 201 MHz. At this point, the muon beam occupies a large volume of phase space which must be reduced, 'cooled', before it can be injected into the acceleration sections. The short muon lifetime makes traditional cooling techniques inappropriate. The required phase-space reduction is achieved by means of ionisation cooling in which the muon beam is passed through a material in which it loses energy through ionisation. The energy lost in the passage of the beam through the material is replaced in accelerating cavities. The IDS-NF baseline calls for lithium hydride absorbers embedded in a solenoidal transport channel with re-acceleration achieved using 201 MHz cavities at a gradient of 16 MV/m. Muon acceleration must be rapid, especially at low muon energy. In the IDS-NF baseline, muons are accelerated to 0.9 GeV in a superconducting linac and then to 12.6 GeV in a sequence of two re-circulating linear accelerators. The final stage of acceleration, from 12.6 GeV to the baseline stored-muon energy of 25 GeV, is provided by a fixed field alternating gradient (FFAG) accelerator. The following paragraphs summarise the status of the work of the Accelerator Working Group.

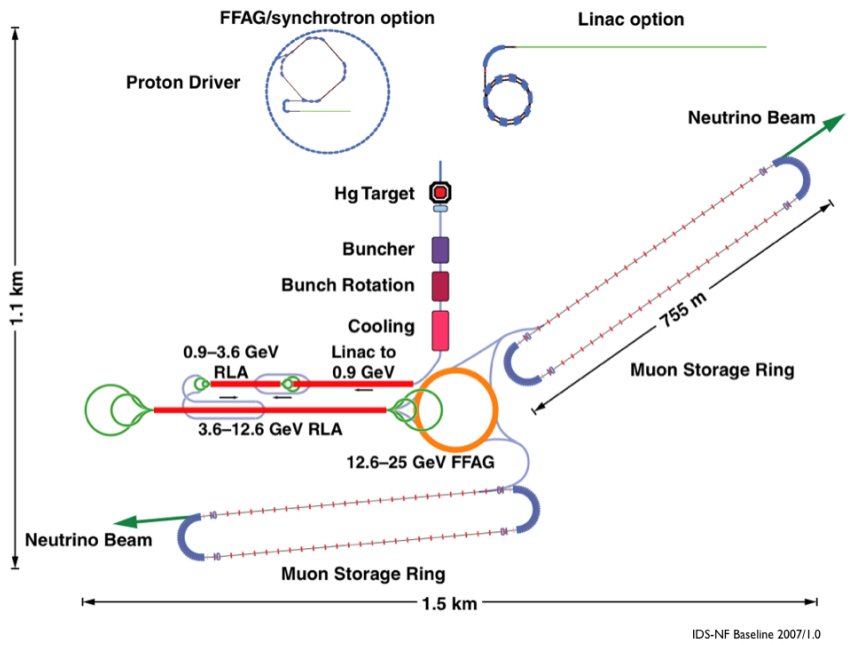


Figure 18: Schematic drawing of the ISS baseline for the Neutrino Factory accelerator complex. The various systems have been drawn to scale. More details can be found in [38] from which the figure is reproduced.

## 3.2 Proton driver

The proton driver is required to deliver 4 MW beam power at an energy of 5–15 GeV. In addition, a particular time structure consisting of three 2 ns rms bunches separated by about 200 $\mu$s is required. The very short bunch length is dictated by the efficiency of the muon-beam capture and the bunch separation is constrained by beam loading in the downstream muon accelerator and the disruption time of the mercury-jet target. In order to achieve such short bunches, a dedicated bunch-compression scenario needs to be designed in order to deal with very strong space-charge forces. The IDS-NF is considering two options for the proton driver. One, based on a superconducting linac, could be implemented by suitable development of the Superconducting Proton Linac (SPL) proposed at CERN [133] or the Project-X linac proposed at FNAL [134]. The second option, based on Rapid Cycling Synchrotrons (RCS) or a novel non-scaling FFAG, could be implemented by upgrading the proton infrastructure at the J-PARC facility or the ISIS accelerator at the Rutherford Appleton Laboratory [135,136]. Accumulator and compressor rings are required in the case of the linac option. A suitable isochronous accumulator ring design has been developed [137]. Two bunch compression schemes, exploiting either superconducting or normal magnets, have been studied taking space-charge forces into account [138]. These studies indicate that the required bunch structure can be delivered. An initial study of a scheme by which the ISIS proton accelerator could be upgraded to provide a MW-class, pulsed spallation-neutron source and a proton driver for the Neutrino Factory has been carried out [139]. By doubling the proton energy used to serve the spallation target, a 4 MW proton beam with appropriate bunch structure could be provided to serve the Neutrino Factory. In such a scenario, the proton drivers

for both facilities share the same source, chopper, linac, accumulation and RCS acceleration to 3.2 GeV. After extraction, three bunches will be sent directly to the neutron-spallation target while three others will be injected into a second RCS where, after acceleration and bunch compression, the beam will be extracted towards the Neutrino Factory pion production target. It will be important to ensure that the schemes developed for inclusion in the IDR remain compatible with the infrastructure envisaged for the potential host laboratories.

## 3.3 Target station

### 3.3.1 Status

The principal objective of thet target tast is to provide a targeting solution for the conversion of a powerful MW-class proton beam into an intense muon beam. We are building on the results of the MERIT experiment which has successfully demonstrated the core concept of a targeting system which can accomplish this task. The IDS-NF baseline concept is based on a free-flowing liquid mercury (Hg) jet which intercepts the proton beam within the confines of a 20 T solenoid field. This configuration presents a high-$Z$ target material which has the attractive attribute of generating copious pions of both signs. These pions are then conducted down a decay channel where muons of both signs can be collected. This target concept is particularly attractive in that although the target is disrupted by the passage of the beam, it is regenerated before the following proton pulse arrives and is capable of with-standing rep rates of up to 50 Hz.

Several technical issues are being studied in order to advance this target concept from a proof-of-principle demonstration to a viable functioning target system. Issues being addressed include improving the performance of the jet-delivery nozzle system and the consideration of the optimal configuration of the mercury-collection pool which will also serve as an in-situ absorber for the unspent proton beam and/or the full proton beam pulse which could be delivered in an accident scenario.

Studies of pion-production efficiencies as a function of the primary proton energy have been performed based on the MARS particle-production code. These results currently favour the energy range of 7–9 GeV for the incoming protons. This result is being checked using other codes. An effort is also underway to benchmark the MARS code in the region of 2–10 GeV based on recently available data from the HARP experiment.

In additional, modeling has explored a range of proton-beam entry angles with a view to optimizing the production effieniency of the pions as well as offering an opportunity to explore the possibility of multiple beam entry points for the proton beam onto the jet. This capability could eventually prove useful as the scenario for producing an intense, short (1 to 3 ns) proton pulse is evaluated.

### 3.3.2 Work in progress

Modeling is ongoing to determine the extent of shielding required to protect adequately the superconducting coils required to generate the 20 T field at the target that tapers to the more modest fields required at the phase rotion section of the front end. Energy deposition studies are ongoing to evaluate the adequate attenuation of the radiation generated at the target and beam dump sites. Thermal management of the target environment will be a principle engineering focus toward a system solution for this target scenario.

Also under consideration is a study of the optimal shape of the field taper as well as an evaluation of the impact of raising and lowering the field strengths at the target. Trade-offs of cost verses performance will be evaluated.

### 3.3.3 Alternative approaches

Solid target solutions remain interesting. The principle attraction for this approach is the relative simplicity of handling the target material. The main challenges for this approach are: the avoidance of rupture due to beam-induced shock; deteriation due to material fatigue; and the need to overcome the formidablechallenge of continually replacing the target in the interaction region at a high rep-rate.

Experiments in which the beam-induced shock is simulated by a current pulse indicate that tungsten rods could form the basis of a solid target system for the Neutrino Factory so long as a mechanism to exchange the tungsten rods at an appropriate frequency can be implemented. Work on the evaluation of such a system based on a rotating wheel have been initiated.

A novel powder jet scheme, in which tiny tungsten balls are fluidised in a high-velocity carrier gas, offers some of the advantages of the mercury jet while avoiding the chemical and some of the radiological issues associated with mercury. A prototype of a powder-jet target has successfully been built and operated; initial results are promising.

## 3.4 Muon front end

In the muon front end we are considering improvements to the baseline configuration. Recent experimental results indicate that RF cavity peak fields may be limited in the presence of magnetic fields and we are investigating a number of techniques to mitigate this technical risk. In addition, we are considering the optimisation of the baseline to improve the muon rate and to reduce the length of the macrobunch, which may ease requirements on kickers and the muon storage rings.

### 3.4.1 Baseline optimisation

We are optimising the baseline configuration presented in the ISS report [132] toward the specification of the subsystem in preparation for the IDS-NF costing excersise. We are developing a baseline which is $\sim 30\%$ shorter than the ISS case and therefore more economical, while exploring the RF-dependent performance, so that we will have a solution with good acceptance, if the RF peak gradient specification must be reduced. The candidate configuration starts with the tapered solenoid from the target (20 T to 1.5 T), where we have alotted 18.9 m for this tapered region to be followed by a drift of 60.7 m length at a constant 1.5 T field. This is followed by a 33 m long buncher with RF that decreases in frequency from 320 MHz to 240 MHz while increasing in gradient (from cavity to cavity). This is followed by an RF rotator (42 m), which then matches into an alternating solenoid cooling channel. The buncher and rotator operate with a 1.5 T focusing field.

### 3.4.2 Alternative Technologies

Three alternative technologies are under consideration. We are examining the possibility of moving to a low RF frequency lattice, increasing the lattice length to remove the RF cavities from magnetic fields, and operating with high pressure gas that will act as an insulator for the cavities.

#### 3.4.2.1 44/88 MHz lattice

This lattice (a development of that presented in [140] is composed of a 30 m long decay channel in 1.8 T magnetic field, followed by a rotation section, a cooling section using $H_2$ absorbers, and an acceleration section, all three using 44 MHz cavities operating at 2 MV/m. Another cooling and acceleration section follows using 88 MHz cavities operating at 4 MV/m. Previous simulation performed using PATH [141] based on the CERN baseline scenario [140] shows that the energy spread is reduced by a factor of two in the rotation stage. The transverse emittance in each plane is reduced by 40% in the first cooling section and by an additional 30% in the second cooling section. The performance of the lattice is being re-examined in ICOOL [**?**] using the current IDS-NF baseline proton beam energy and target geometry.

#### 3.4.2.2 Stretched lattice

Here RF cavities are taken outside of the magnetic fields by making the lattice cell longer and introducing a modicum of shielding around the coil. While this abrogates the issue of RF cavities sitting in magnetic fields, it makes the beam optics more challenging. This necessitates the use of liquid hydrogen absorbers in the cooling section, possibly a more challenging technology, and quite an aggressive optimisation of the beam optics. Simulations show that a reasonable performance can be achieved, close to that which can be reached by the baseline.

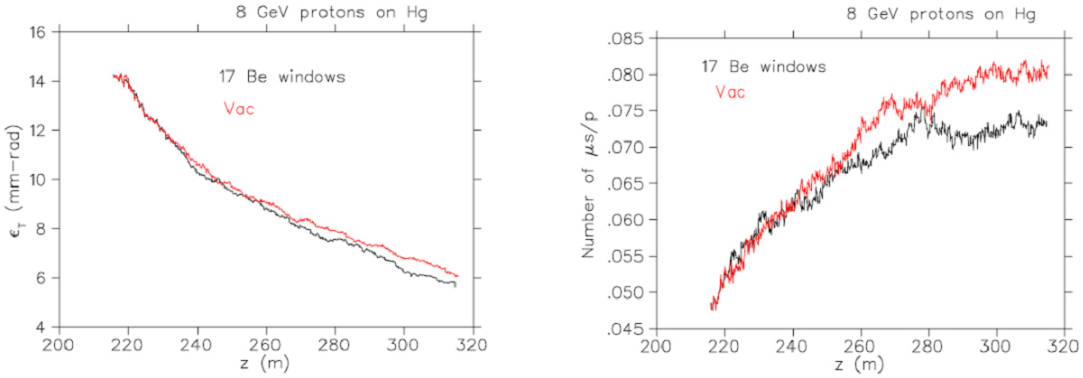


Figure 19: (left) Emittance cooling of hybrid channel (black line) with 17 Be isolation windows compared with that of baseline vacuum case (red line). (right) Throughput of hybrid cooling channel (black line) compared with vacuum channel (red line). Even with 17 isolation windows, the cooling is comparable and the transmission is only reduced by about 10%.

#### 3.4.2.3 Hybrid lattice

A potential vulnerability of the vacuum-RF-cavity cooling channel designs is the degradation in maximum gradient observed for such cavities when immersed in a strong axial magnetic field. While we have not yet studied this in detail for a 201-MHz "MICE-like" cavity, the effect could limit the achievable gradient in our baseline cooling channel, with a concomitant decrease in its particle transmission. From other experiments [142] we know that a cavity filled with high-pressure H2 gas does not suffer a degradation in gradient in a magnetic field. This is encouraging, though it remains to be seen whether such a gas-filled cavity can operate successfully in an intense beam of ionizing radiation.

As a fall-back scenario, we have taken an initial look at the possibility of using gas-filled high-pressure RF (HPRF) cavities in place of vacuum cavities to achieve the required 15 MV/m gradient. Because the energy loss in a high-pressure gas is much lower than that for a liquid or a solid, we have adopted a hybrid approach, wherein the gas pressure is chosen to be sufficient only to reach the desired gradient, and the bulk of the energy loss still occurs in solid LiH absorbers. Initial simulations of such a channel operating at 34 bar have been carried out [143] and the results are encouraging. Figure 19 shows the results of an ICOOL simulation of the baseline cooling channel with HPRF cavities. Even if the effects of many low-Z isolation windows (which might be required for safety reasons) are included, there is essentially no loss in performance of the hybrid channel compared with the baseline design. In terms of lattice layout and magnets, the hybrid channel is identical to the baseline channel, so the beam dynamics performance is maintained.

Other experiments planned for the MTA at Fermilab will demonstrate the performance of gas-filled cavities in an intense ionizing beam. If these tests are successful, the hybrid approach studied here would provide a validated means of reaching the design performance in a linear 4D cooling channel and might be an attractive option to consider for an updated baseline configuration.

### 3.4.3 Other Options

We are also considering a few other options, for example the use of a helical magnet or a tilted solenoid that would introduce dispersion into the beam. This may allow emittance exchange, allowing emittance to be reduced in both transverse and longitudinal phase space. In addition, we are looking at a few novel options for the cooling lattice, such as a doublet magnet structure.

## 3.5 Muon acceleration

In the IDS-NF baseline, muons are accelerated by a linac, two recirculating linear accelerators (RLAs) and a fixed-field alternating gradient accelerator (FFAG).

### 3.5.1 Muon linac and RLAs

To ensure an adequate survival rate for the short-lived muons, acceleration must occur at high average gradient. The accelerator must also accommodate the phase-space volume occupied by the beam after the cooling channel. The need for large transverse and longitudinal acceptances [144] drives the design of the acceleration system to low RF frequency, e.g. 201 MHz. High-gradient, normal-conducting RF cavities at these frequencies would require very high peak-power RF sources. Hence, superconducting RF (SCRF) cavities are preferred. In the acceleration scheme presented we choose a state-of-the-art SCRF gradient of 17 MV/m.

### 3.5.2 Muon RLA complex

The proposed recirculating-linear-accelerator (RLA) based muon accelerator complex consists of the following components:

1. A 201 MHz SCRF linac pre-accelerator that captures the large muon phase space coming from the cooling channel lattice and accelerates the muons to 0.9 GeV, while adiabatically decreasing the phase-space volume;
2. A low energy RLA (RLA I) that further compresses and shapes the longitudinal and transverse phase-space, while increasing the energy to 3.6 GeV; and
3. A second stage RLA (RLA II) that further accelerates muons to 12.6 GeV.

The overall layout of the accelerator complex is shown in figure 20.

#### 3.5.2.1 Linear pre-accelerator

A single-pass linac "pre-accelerator" raises the beam energy to 0.9 GeV. This makes the muons sufficiently relativistic to facilitate further acceleration in an RLA. In addition, the longitudinal


Figure 20: Layout of the accelerator complex. For compactness all components (the linac and the two RLAs) are stacked vertically; $\mu^{\pm}$ beam transfer between the accelerator components is facilitated by the vertical double chicane (see text).

phase-space volume is adiabatically compressed in the course of acceleration [145]. The large acceptance of the pre-accelerator requires large aperture and tight focusing at its front-end. Given the large aperture, tight space constraints, moderate beam energies, and the necessity of strong focusing in both planes, we have chosen solenoidal focusing for the entire linac [144]. To achieve a manageable beam size in the linac front-end, short focusing cells are used for the first 6 cryo-modules. The beam size is adiabatically damped with acceleration. This allows the short cryo-modules to be replaced with eight intermediate-length cryo-modules and then with 11 long cryo-modules as illustrated in figure 21. The initial longitudinal acceptance of the linac is chosen to be $2.5\sigma$, i.e. $\Delta p/p = \pm 17\%$ and RF pulse length $\Delta\phi = \pm 72°$. To perform adiabatic bunching [144, 146] the RF phase of the cavities is shifted by 72° at the beginning of the pre-accelerator and then gradually changed to zero (on-crest) by the end of the linac. In the first half of the linac, when the beam is still not completely relativistic, the offset causes synchrotron motion which allows bunch compression in both length and momentum spread, yielding $\Delta p/p = \pm 7\%$ and $\Delta\phi = \pm 29°$. The synchrotron motion also suppresses the sag in acceleration for the bunch head and tail. In our tracking simulation we have assumed a particle distribution that is Gaussian in 6D phase space with the tails of the distribution truncated at $2.5\sigma$, which corresponds to the beam acceptance. Despite the large initial energy spread, the particle tracking simulation through the linac does not predict any significant emittance growth. There is a 0.2% beam loss coming mainly from particles at the longitudinal phase space boundary. Results of the simulation are illustrated in figure 22, which shows 'snapshots' of the longitudinal phase space at the beginning and at the end of the pre-accelerator.

#### 3.5.2.2 Main acceleration system

The superconducting accelerating structure is expected to be by far the most expensive component of the accelerator complex. Therefore, maximising the number of passes in the RLA has a significant impact on the cost-effectiveness of the overall acceleration scheme [146]. We propose to use a 4.5 pass 'dog-bone' configuration for the RLA (figure 20), which has the following advantages compared to a race-track configuration:

- Better orbit separation at the linac ends resulting from a larger (factor of two) energy

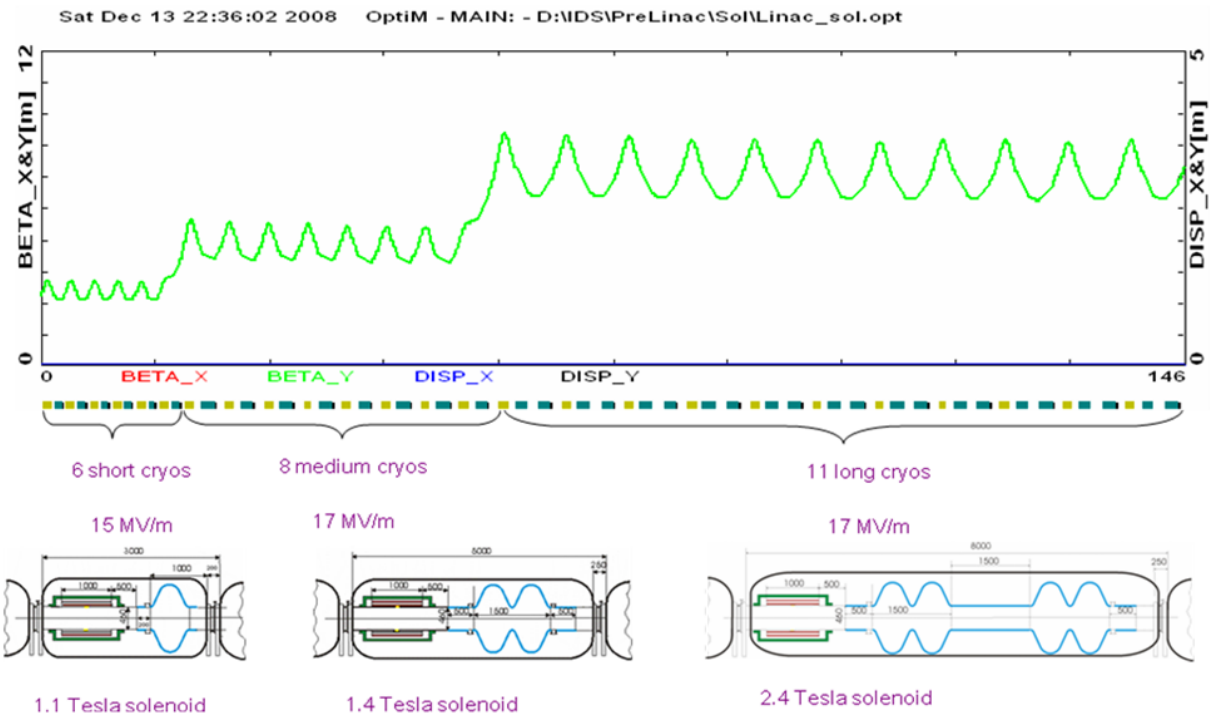


Figure 21: Top: Transverse optics of the linac - uniform periodic focusing with 6 short, 8 medium, and 11 long cryo-modules. Bottom: Layout of the short, intermediate and long cryo-modules.

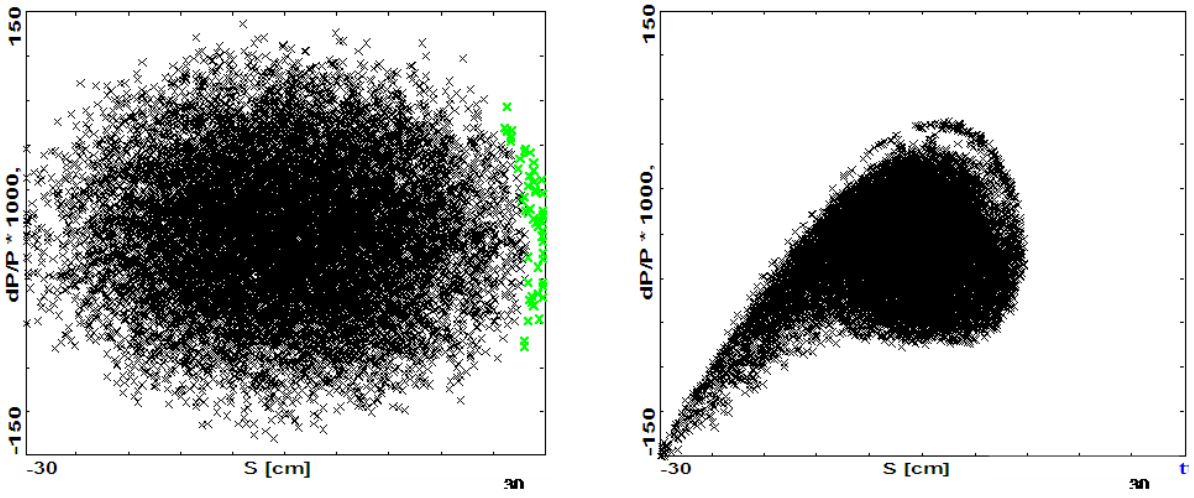


Figure 22: Particle tracking results showing adiabatic bunch compression along the linac. The longitudinal phase-space $(z, \Delta p/p)$ is shown before (left) and at the end (right) of acceleration. Particles marked in green are lost during tracking (outside the 20 cm aperture).

difference between two consecutive linac passes [147]; and

- A favourable optics solution for simultaneous acceleration of both $\mu^+$ and $\mu^-$ in which both charge species traverse the RLA linac in the same direction while passing in the opposite

directions through the mirror symmetric optics of the return droplet-arcs [148].

The dog-bone multi-pass linac optics are shown in figure 23. The dog-bone RLA I simultaneously accelerates the $\mu^+$ and $\mu^-$ beams from 0.9 GeV to 3.6 GeV. The injection energy into the RLA and the energy gain per RLA linac were chosen so that a tolerable level of RF phase slippage along the linac could be maintained.

We have performed a simple calculation of the phase slippage for a muon injected with initial energy $E_0$ and accelerated by $\Delta E$ in a linac of length $L$, where the linac consists of uniformly spaced RF cavities phased for a speed-of-light particle. Our calculation used the following cavity-to-cavity iterative algorithm for the phase-energy vector:

$$\begin{pmatrix} \phi_{k,i+1} \\ E_{k,i+1} \end{pmatrix} = \begin{pmatrix} \phi_{k,i} + \frac{\pi h}{\lambda \gamma_{k,i}^2} \\ E_{k,i} + qV_i \cos(\phi_{k,i}) \end{pmatrix} ; \tag{9}$$

where $\phi$ represents the phase slip of the bunch centroid at a given cavity (in degrees of 201 MHz RF), $h = L_{\rm linac}/N_{\rm cav}$, $\lambda = c/f_0$, $k$ is the particle index, $i = 0, \ldots N_{\rm cav} - 1$, and $V_i$ is the maximum accelerating voltage in cavity $i$.

The resulting phase slippage profiles along the multi-pass RLA linacs can be summarized as follows. For the RLA injection energy of 0.9 GeV, the critical phase slippage occurs for the initial half-pass through the linac and it is about 40°, which is still manageable and can be mitigated by appropriate gang phase in the following linac (1-pass). For subsequent passes, the phase slippage gradually goes down and can be used, along with the sizable momentum compaction in the arcs, to compress the longitundinal phase space of the beam further. The initial bunch length and energy spread are still large at the RLA input and further compression is required in the course of the acceleration. To accomplish this, the beam is accelerated off-crest with non-zero momentum compaction ($M_{56}$) in the droplet-arcs [146]. This induces synchrotron motion, which suppresses the longitudinal emittance growth arising from the non-linearity of the accelerating voltage. Without synchrotron motion, the minimum beam energy spread voltage over the bunch length and would be equal to $(1 - \cos\phi) \sim 9\%$ for a bunch length $\phi = 30°$. The synchrotron motion within the bunch averages the total energy gain of particles in the tail to the energy gain of particles in the core. The focusing profile along the linac of the dog-bone RLA is designed so that beams within a vast energy range can be transported within the given aperture. It is also desirable that the focusing profile is optimized to accommodate the maximum number of passes through the RLA.

In addition, to facilitate simultaneous acceleration of both $\mu^+$ and $\mu^-$ bunches, a mirror symmetry must be imposed on the droplet-arc optics (oppositely charged bunches move in opposite directions through the arcs). This puts a constraint on the exit/entrance Twiss functions for two consecutive linac passes, namely $\beta_{\rm out}^n = \beta_{\rm in}^{n+1}$ and $\alpha_{\rm out}^n = \alpha_{\rm in}^{n+1}$, where $n = 0, 1, 2 \ldots$ is the pass index. Since the beam is traversing the linac in both directions throughout the course of acceleration, a 'bisected' focusing profile [148] has been chosen for the entire linac, illustrated in figure 23.

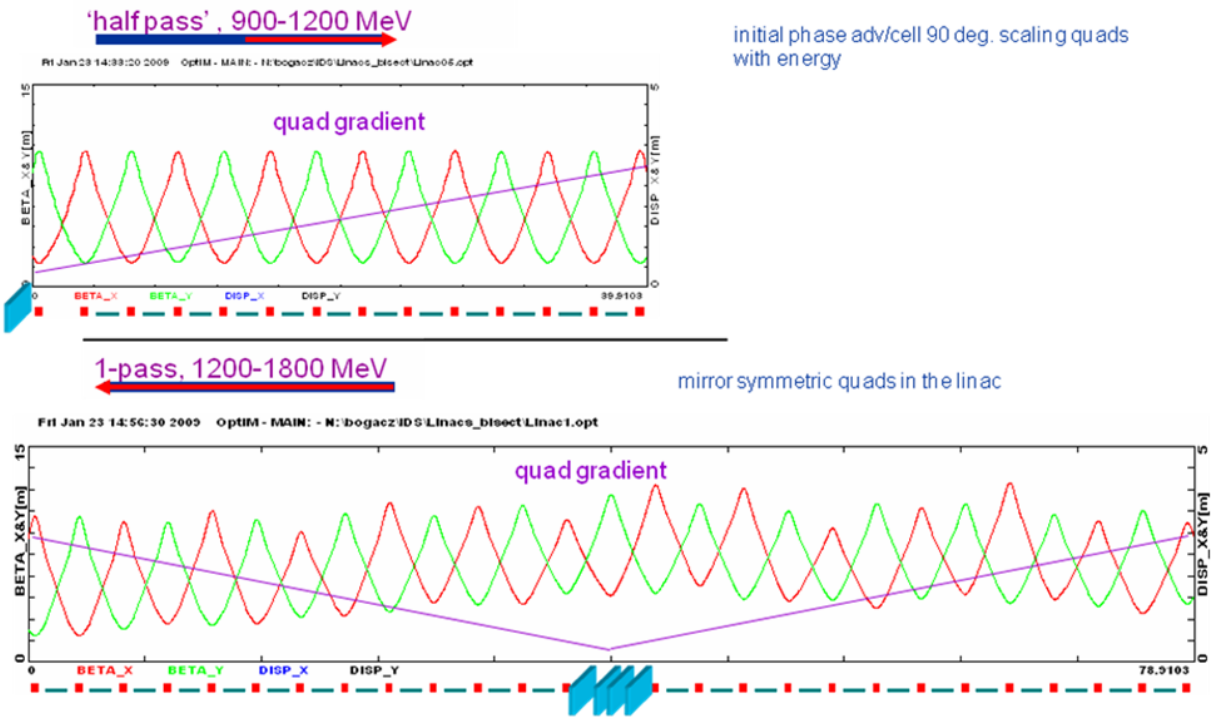


Figure 23: FODO based multi-pass linac optics. The quadrupole gradients scale up with momentum to maintain 90° phase advance per cell for the first half of the linac, then they are mirror reflected in the second half. The resulting linac optics is well balanced in terms of Twiss functions and beam envelopes; there is sufficient phase advance up to the fifth pass.

At the ends of the RLA linacs, the beams need to be directed into the appropriate energy-dependent droplet-arc for recirculation [147]. For practical reasons, horizontal rather than vertical beam separation was chosen. Rather than suppressing the horizontal dispersion created by the spreader, the horizontal dispersion has been smoothly matched to that of the outward 60° arc. Then, by an appropriate pattern of removed dipoles in three transition cells, the dispersion for the inward bending 300° arc is flipped. The droplet-arc layout is shown in figure 24. The entire droplet-arc architecture is based on 90° phase advance cells with periodic beta functions. The droplet-arc optics, based on FODO focusing [146], are illustrated in 24, which also shows the longitudinal phase-space occupied by the beam at the entrance and at the exit of the arc. The momentum compaction is relatively large, which guarantees significant rotation in the longitudinal phase space as the beam passes through the arc. This effect, combined with off-crest acceleration in the subsequent linac, yields further compression of the longitudinal phase-space as the beam is accelerated.

To transfer both $\mu^+$ and $\mu^-$ bunches from one accelerator to the other, which is located at a different vertical elevation, we use a compact double chicane [148] based on a periodic 90° phase advance FODO cell. Each leg of the chicane involves four horizontal and two vertical bending magnets, forming a double achromat in the horizontal and vertical planes, while preserving periodicity of the beta functions.

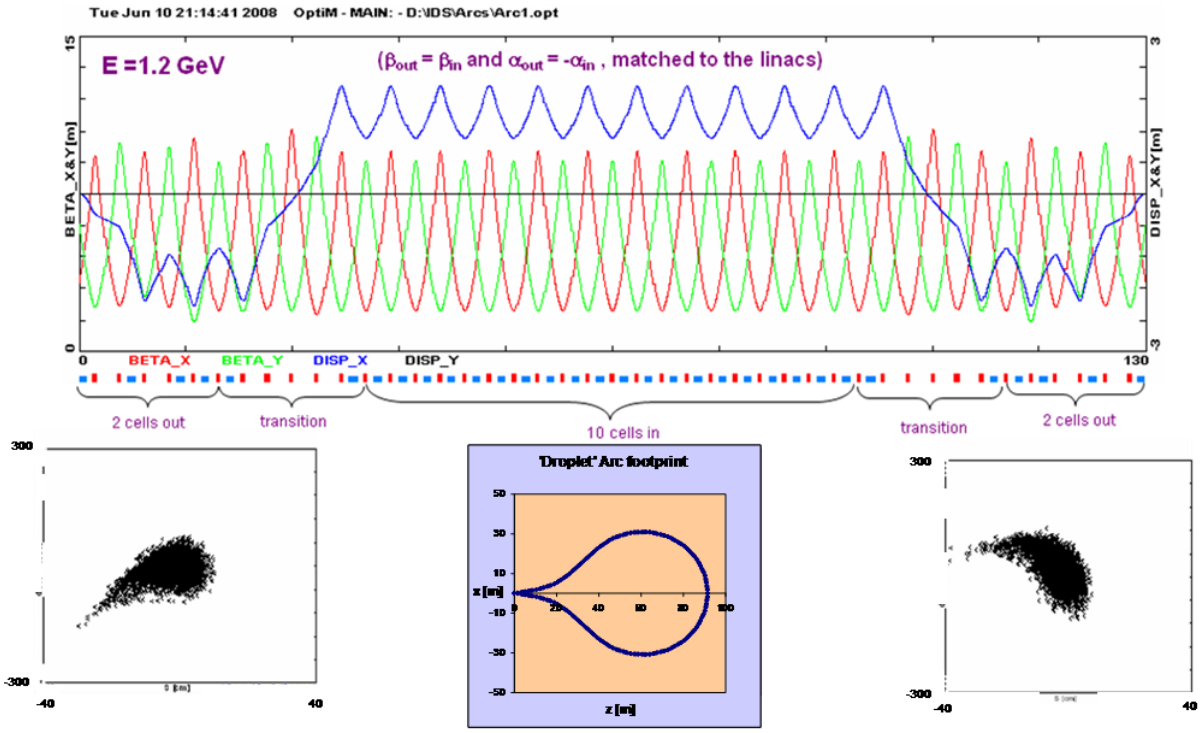


Figure 24: Top: Droplet-arc optics, showing the uniform periodicity of beta functions and dispersion. Bottom: Particle tracking results showing the longitudinal phase-space compression. The longitudinal phase space ($s$ [cm], $\Delta p/p \times 1000$) is shown at the beginning (left) and at the end (right) of the arc.

#### 3.5.2.3 Accelerator performance

The 6D distribution at the end of the cooling channel [148] was used to define initial longitudinal and transverse acceptances. The 6D distribution was then traced through all stages of the accelerator complex. The resulting longitudinal emittance evolution is shown in figure 24. The phase space at the RLA exit is characterised by $\Delta p/p = 0.012$ (rms) and $\Delta z = 8.5$ cm (rms). A similar end-to-end tracking study was carried out for the transverse phase space. Overall, 2% of the beam was lost out of the dynamic aperture. These losses may be mitigated by using chromaticity correcting sextupoles [147] placed at the spreader and recombiner regions of the droplet-arcs.

#### 3.5.2.4 Linac Engineering Design and Tracking Simulation

In addition to the optics design outlined above, work has begun on the engineering design of the linac and detailed tracking studies using realistic field maps. Magnetic field distribution and fringe effects have been analysed using dedicated numerical codes such as Superfish [149, 150]. Also, making use of the Superfish and Comsol [151] codes, the superconducting RF cavities have been modelled and particle tracking was performed using the GPT code [152]. In order to accommodate the real muon beam from the cooling channel into the linac an additional solenoid has been inserted in-between with the aim of matching the beam optics.

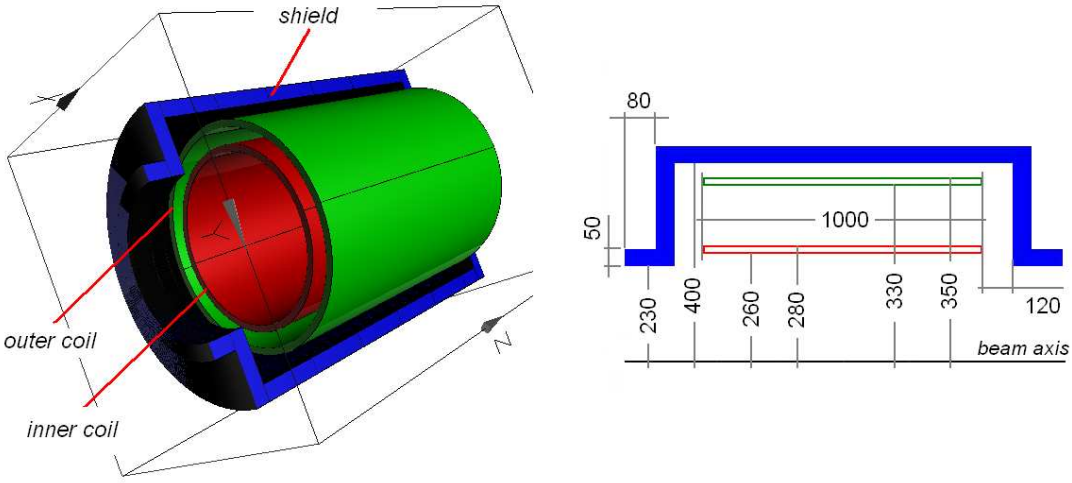


Figure 25: Solenoid layout for all three linac sections.

The basic layout of the solenoids is shown in figure 25; it consists of two coaxial superconductor shells carrying opposite currents and a low-carbon iron shield. Numerical optimisation of the shielded solenoids has been performed keeping their length constant to 1 m and tuning the two opposite currents so that the on-axis peak longitudinal magnetic field is $B_0 = 2$ T while the magnetic shield remains below the saturation level. First magnetization curves for decarburized iron are shown in figure 26 as implemented in the Superfish and Roxie codes.

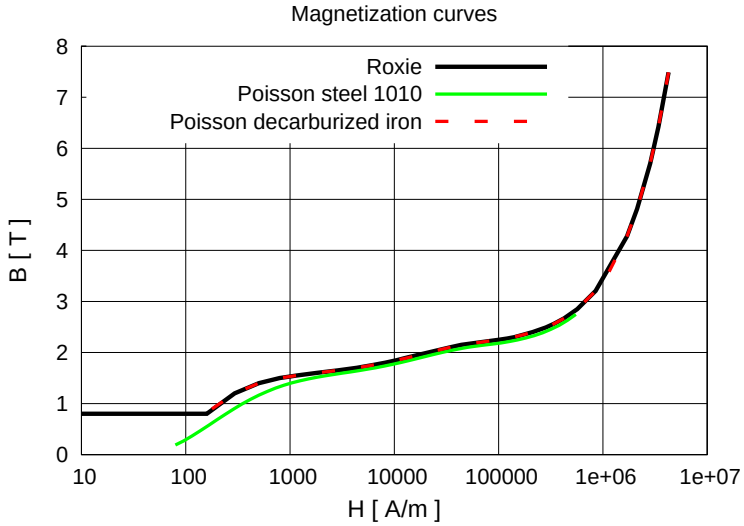


Figure 26: First magnetization curves for some materials used by the Superfish and Roxie codes.

Before finding suitable values for the two opposite currents it is useful to establish a relationship between their ratio and the total magnetic field along three important paths, namely at $r = 0$ m (beam axis), $r = 0.305$ m (mid-distance between the two shells), $r = 0.425$ m (shield core) and

any fixed path with $r \geq 0.45$ m (beyond the shield). As can be seen from figure 27, working with $1.5 \leq j_i/j_o \leq 2.5$ keeps the shield under saturation since there is almost no leakage radially beyond it.

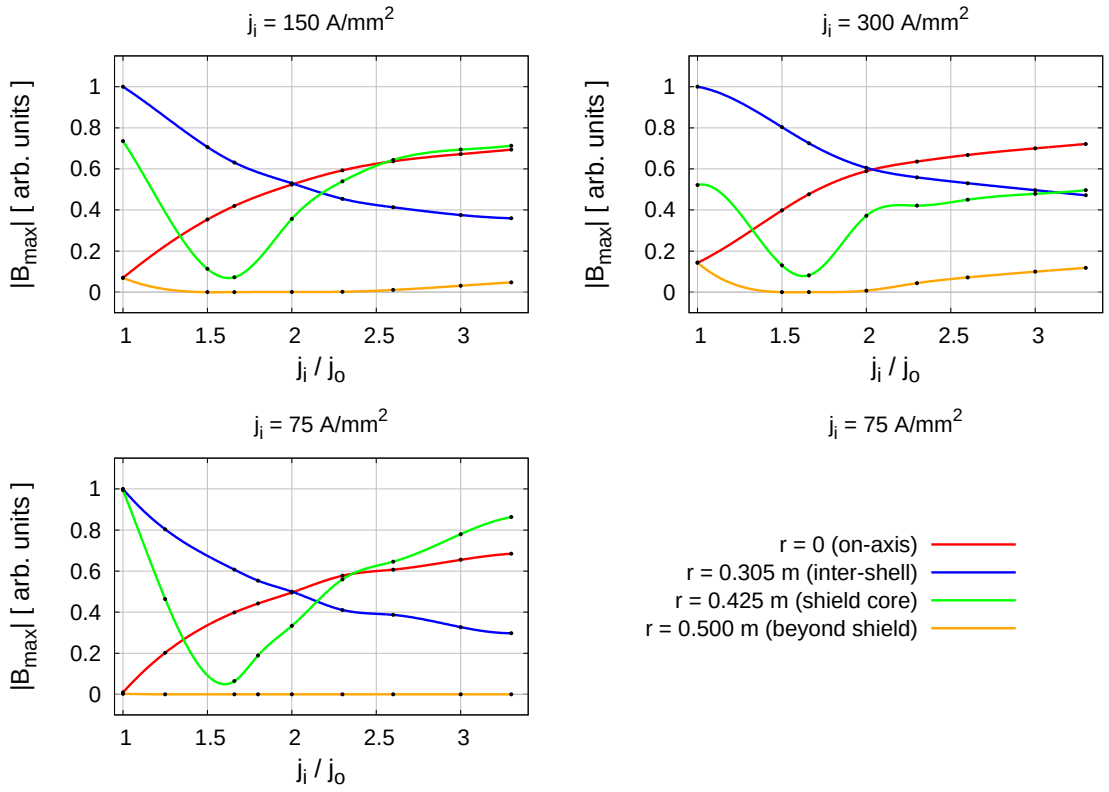


Figure 27: Magnetic induction as a function of the ratio between the inner and outer shell currents. Black dots represent values read from the Superfish code.

The optimum point is around $j_i/j_o = 2$ for which the on-axis field equals the inter-shell field. An increase of the latter indicates an enhanced probability to reach the saturation of the shield at its longitudinal edges as well as to quench the shell conductors. Remarkably, at this point the field along the shield core is about 30% less than the on-axis field. The relationship found at $j_i/j_o = 2$ holds for three different current densities of the inner shell, which ensures that setting $j_i$ around 150 A/mm$^2$ makes essentially no difference. This linearity also means that the radial shield is bellow the saturation point. However, its longitudinal edges have to be analysed. In order to achieve 2 T on the beam axis, the two current densities must be $j_i = 180$ A/mm$^2$ and $j_o = -90$ A/mm$^2$ respectively. As it can be seen from figure 28 there is no leakage beyond the shield for these current densities, but the field is locally enhanced around the inner shell.

A layout for the single-cell RF cavity is shown together with its total electric field map in figure 30. It resonates on the acceleration mode at 201.25 MHz having a transit time factor of 0.7.

As described in [153], the Courant-Snyder beta- and alpha-functions for a given momentum

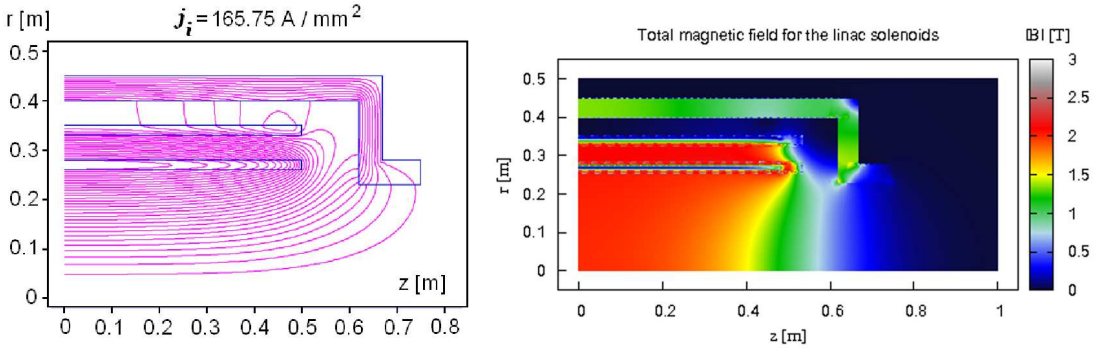


Figure 28: Fringe magnetic fields as retrieved from the Poisson code corresponding to $B_0 = 2$ T.

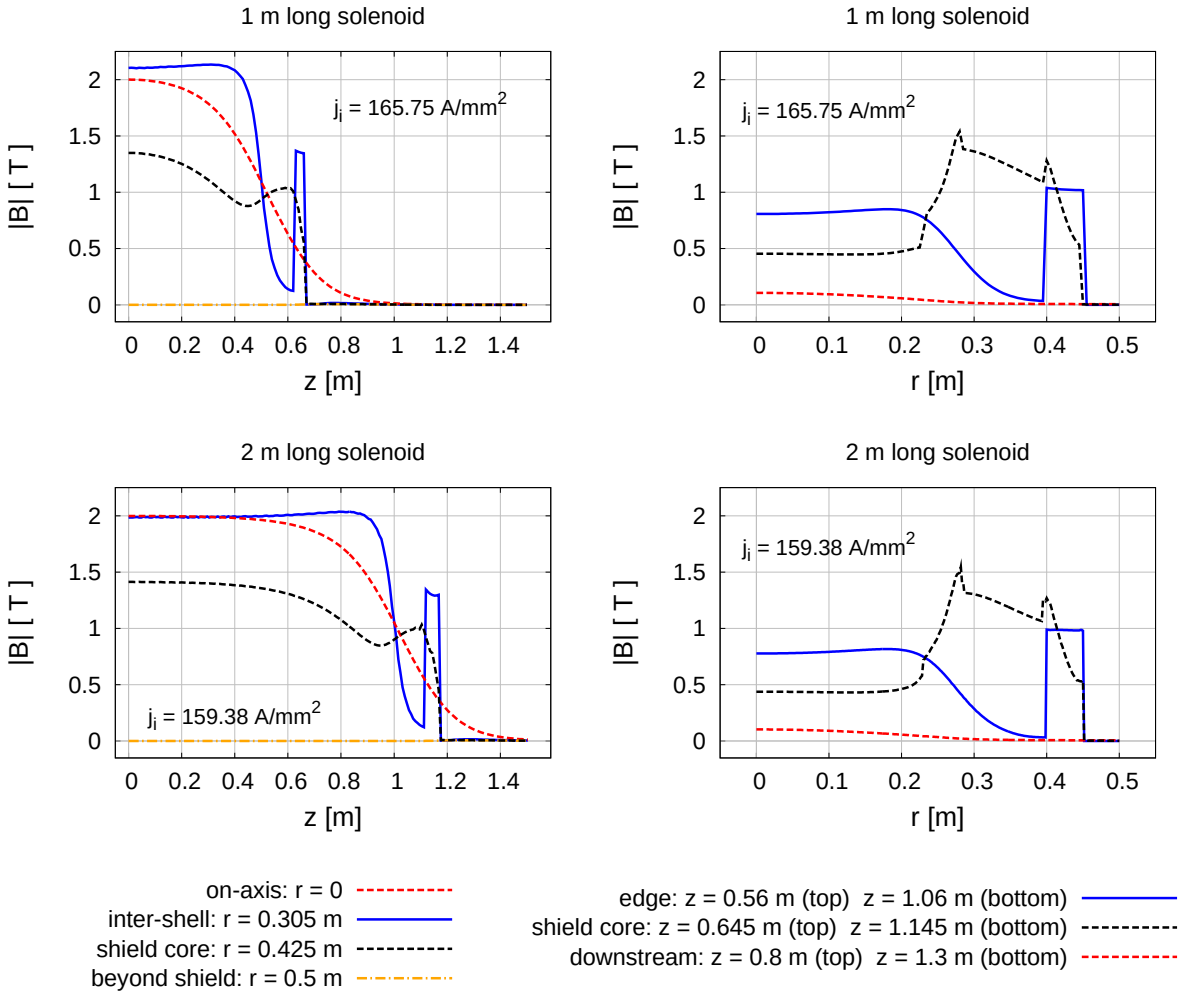


Figure 29: Magnetic field along four paths for $j_i = 180$ A/mm$^2$.

can be derived from the on-axis magnetic field maps. The periodic betatron functions for the present lattice is shown in figure 31. When the RF cavities are added, the solenoids have to be tuned to keep the same focusing strength while acceleration occurs between them. Matching

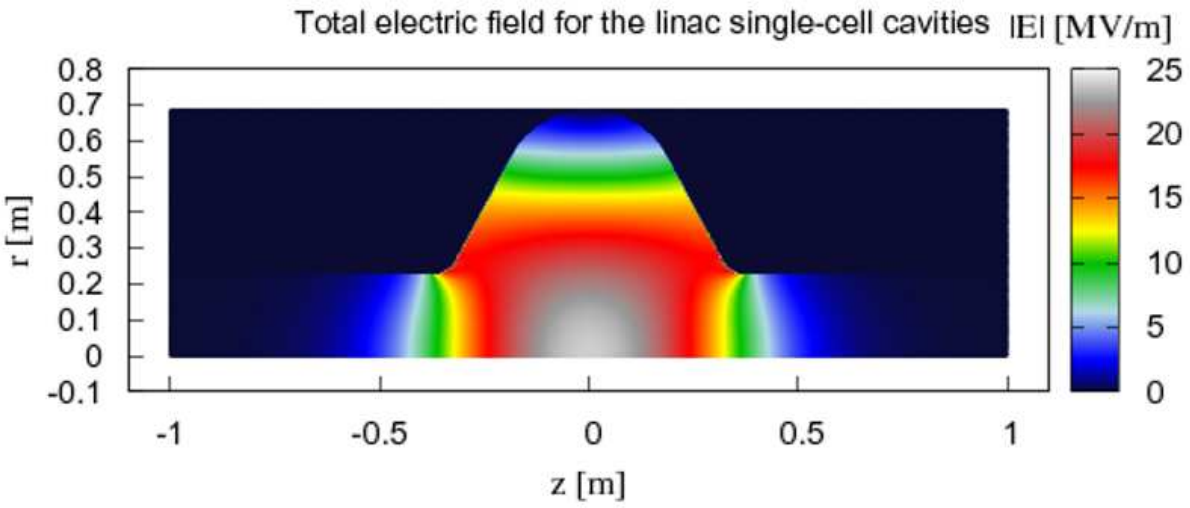


Figure 30: Layout of the single-cell RF cavity.

between the cooling channel and the linac has been achieved adding an extra solenoid identical to those in the cooling channel i.e. $15 \times 15$ cm$^2$ for the transverse cross-section:

$$\frac{1}{2}\beta\beta'' - \frac{1}{4}\beta'^2 + \frac{1}{4}\beta^2 S^2 = 1\,;$$
$$S = \frac{q[C]\, B_{||}[T]}{p[kg\ m\ s^{-1}]}\,.$$

Having the optics matched has enabled particle tracking to be performed from the cooling channel through the linac with filtered realistic beam ditributions as shown in figure 32. Tracking results are shown up to the first solenoid in the linac in figure 33. It is noticed that the beam passes into the linac with minor losses.

#### 3.5.2.5 Linac and RLA conclusions

In summary, the results of our study suggest that there are no obvious physical or technical limitations precluding design and construction of an accelerator complex based on a pair of 4.5-pass dog-bone RLAs for acceleration of muons to 12.6 GeV. Design choices made in the proposed acceleration scheme were driven by the beam dynamics of large phase-space beams. The presented end-to-end simulation validates the efficiency and acceptance of the accelerator system. Tracking simulations and detailed engineering designs are now in progress.

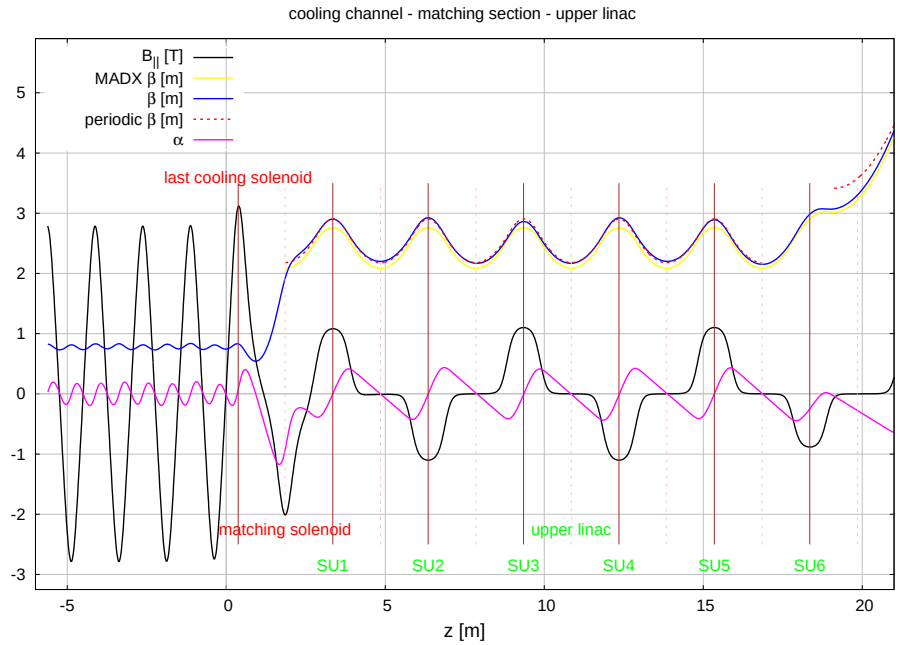


Figure 31: Betatron functions for the cooling channel, matching solenoid and upper section of the linac using MADX (yellow solid line) and the field maps approach (blue solid and red dashed lines).

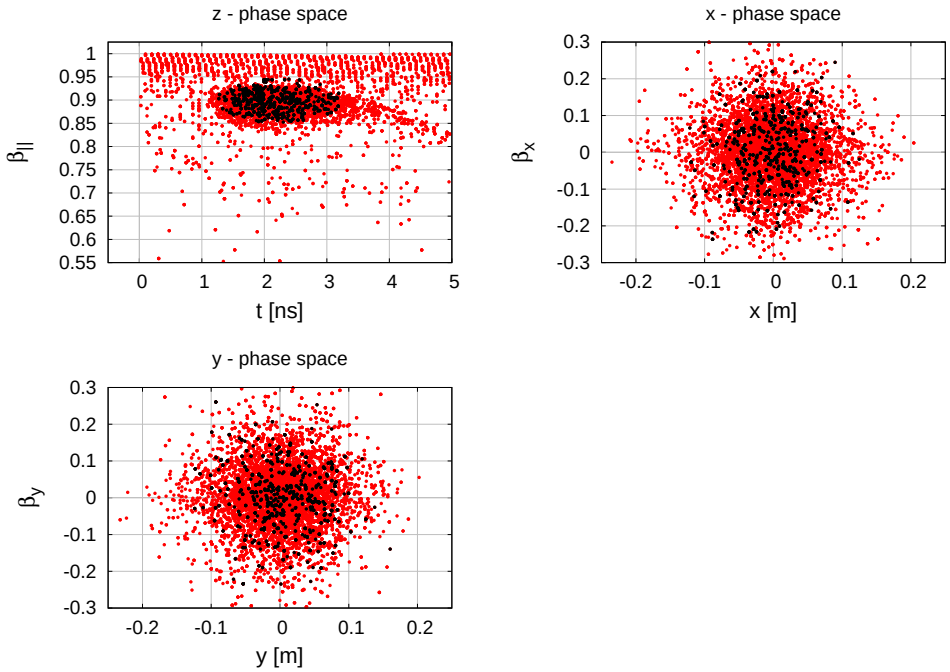


Figure 32: Only 10% of the initial particle distribution has been selected for a preliminary tracking session. They cover the whole $x$- and $y$-phase spaces but only 2 ns - range of the longitudinal phase space.

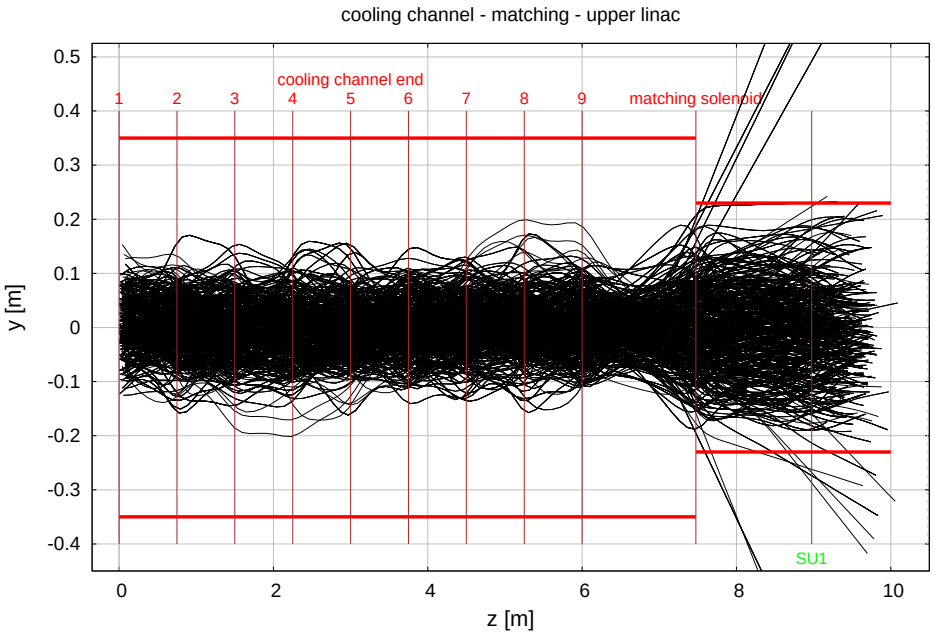


Figure 33: Beam tracking with 1000 particles. The red horizontal lines mark the appertures of the cooling and linac solenoids respectively.

### 3.5.3 Scaling FFAG as an alternative to the RLAs

#### 3.5.3.1 Introduction

The possibility of using the scaling type of FFAG ring for muon acceleration has already been proposed [154]. However, the design proposed in [154] assumed very low RF frequencies, incompatible with a frequency of the order of 200 MHz or higher. Here we present a scheme, based on stationary bucket acceleration [155], to accelerate muon beams in a scaling FFAG ring, with 200 MHz RF frequency.

### 3.5.4 Muon Beam Acceleration

The example of a 3.6 GeV to 12.6 GeV ring with parameters given in table 3 is considered. It is assumed that scaling FFAG magnets with a maximum field of about 4 T will be used. It is a reasonable assumption once superconducting magnets with an left-right asymmetric coil distribution [156] are employed to realise the scaling field law. In order to allow simultaneous acceleration of $\mu^+$ and $\mu^-$ beams, the path length per cell of the synchronous particle is adjusted to be a multiple of $\frac{1}{2}\beta_s\lambda_{RF}$, with $\beta_s$ the ratio of the synchronous-particle velocity to the speed of light and $\lambda_{RF}$ the RF wavelength. We use stepwise particle tracking in a geometrical field model with Enge-type fringe field [157] to study the beam dynamics. Results of single particle tracking at fixed energy show normalised transverse acceptances larger than 30 $\pi$ mm rad for both horizontal and vertical planes.

Table 3: Ring parameters.

| | |
|---|---|
| Lattice type | scaling FFAG FDF triplet |
| Injection energy | 3.6 GeV |
| Extraction energy | 12.6 GeV |
| RF frequency | 200 MHz |
| Mean radius | $\sim$ 160.9 m |
| Synchronous energy (kinetic) | 8.04 GeV |
| Hormonic number $h$ | 675 |
| Number of cells | 225 |
| Field index $k$ | 1390 |
| RF peak voltage (per turn) | 1.8 GV |
| Number of turns | 6 |
| $B_{max}$ (at 12.6 GeV) | 3.9 T |
| Drift length | $\sim$ 1.5 m |
| Horizontal phase advance per cell | 85.86 deg. |
| Vertical phase advance per cell | 33.81 deg. |
| Excursion | 14.3 cm |

#### 3.5.4.1 6D Simulation of a Whole Acceleration Cycle

At the beginning of each 6D tracking, the bunch of particles is prepared as follows: 1000 particles are uniformly distributed inside a transverse 4D ellipsoid ('waterbag' distribution) and, independently, distributed uniformly inside an ellipse in the longitudinal plane. Initial normalised bunch emittances are 30 $\pi$ mm rad in both horizontal and vertical planes and 150 mm in the longitudinal plane.

Tracking results show no beam lost during the acceleration cycle. No significant emittance blow-up is observed in either the longitudinal (see figure 34) or the transverse planes (see figure 3.5.4.1.

Tracking introducing random alignment errors in the lattice has been performed. No beam loss has been observed with an rms alignment error smaller than 1 mm.

#### 3.5.4.2 Summary

A scheme to accelerate muon beams inside the stationary RF bucket of scaling FFAG rings using 200 MHz RF cavities has been proposed. This ring can accelerate both $\mu^+$ and $\mu^-$ beams simultaneously. Acceleration is done within 6 turns, the RF is used in an efficient way. Detailed tracking study on the example of a 3.6 GeV to 12.6 GeV muon ring has been presented. 6D particle tracking in soft-edge field model shows that the acceptance of this scheme is larger than 30 $\pi$ mm rad in both horizontal and vertical planes, and larger than 150 mm in the longitudinal

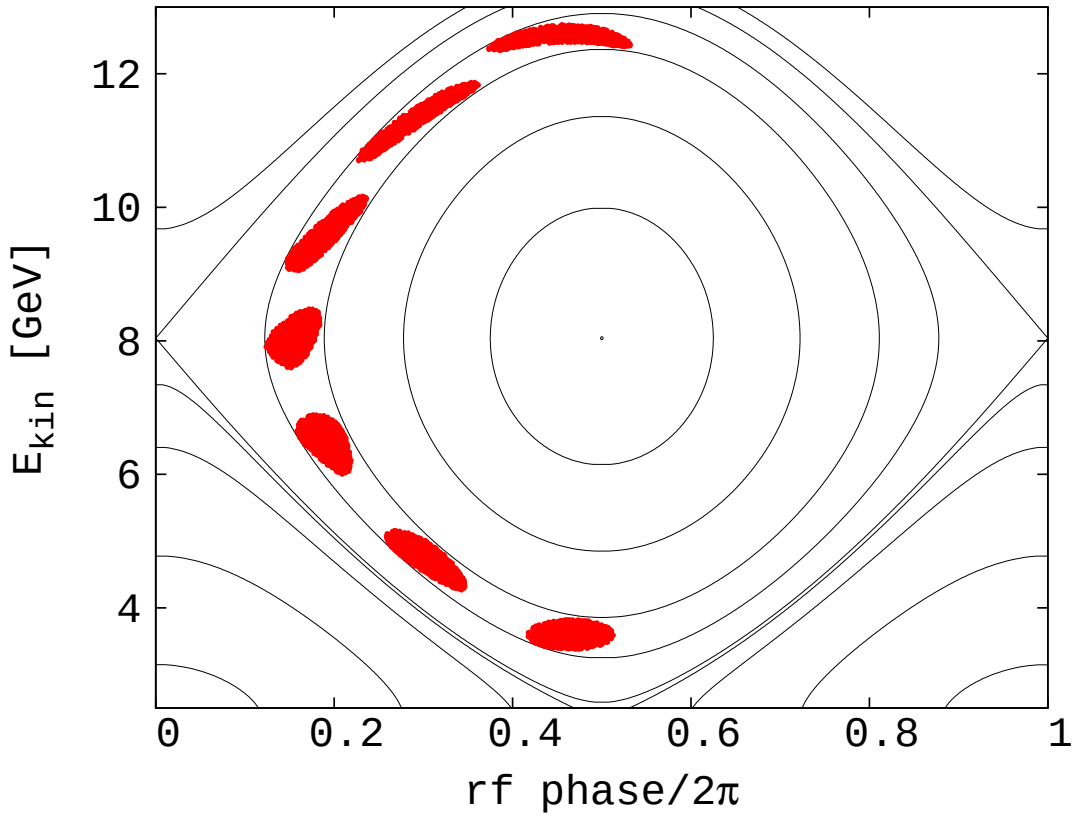


Figure 34: 6-turn acceleration cycle plotted in the longitudinal phase space. Hamiltonian contours are superimposed.

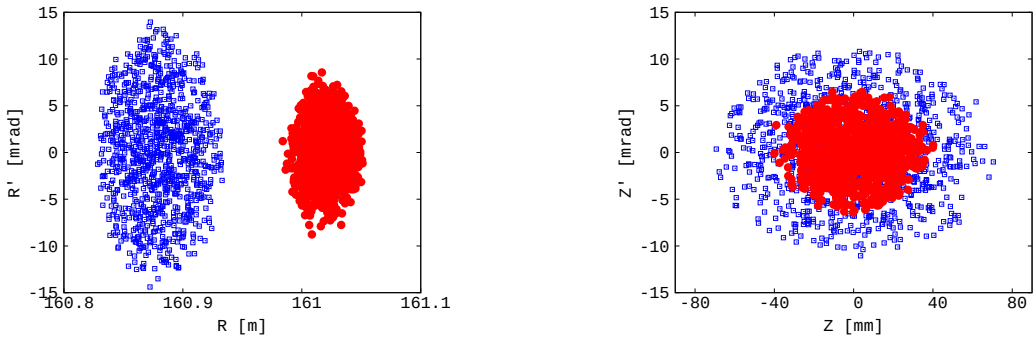


Figure 35: Initial (blue squares) and final (red dots) particle positions plotted in the horizontal (left figure) and vertical (right figure) phase spaces.

plane. No beam loss and no significant emittance blow-up was observed, either in the transverse or in longitudinal plane. This scheme also shows a good tolerance to alignment errors.

The design of superconducting scaling FFAG magnet has been initiated at Kyoto university. The study of the injection and extraction schemes for this ring has been started in collaboration with J. Parsternak (Imperial College London/RAL STFC).

### 3.5.5 Muon FFAG

#### 3.5.5.1 Parameter Updates

The basic parameters of the FFAG lattice have been updated from the values presented at the 2009 Particle Accelerator Conference [158]. Additional cavity-free drifts were added to accommodate hardware for injection and extraction, additional drifts were added for other hardware, and an error was corrected in the previous lattices (neglecting a drift in the circumference calculation). A doublet lattice is no longer under consideration since it does not allow for a symmetric treatment of injection and extraction for the two muon charge signs.

| Configuration | FDFC | FCDC | FDFCC |
|---|---|---|---|
| Cells | 80 | 68 | 64 |
| D length (m) | 1.494717 | 1.420965 | 1.956090 |
| D radius (mm) | 87 | 94 | 115 |
| D max field (T) | 7.0 | 6.4 | 6.5 |
| F length (m) | 0.997549 | 2.238741 | 1.286477 |
| F radius (mm) | 115 | 200 | 153 |
| F max field (T) | 3.9 | 3.1 | 3.6 |
| Inter-magnet drift (m) | 0.5 | n/a | 0.5 |
| Long drift(s) (m) | 2.0 | 2.0 | 3.0 |
| Cavity cells | 60 | 116 | 88 |
| RF voltage (MV) | 763.066 | 1475.261 | 1119.163 |
| turns | 17.3 | 9.0 | 11.8 |
| Circumference (m) | 519 | 521 | 546 |
| Decay (%) | 7.7 | 4.1 | 5.6 |
| Cost (A.U.) | 146.1 | 170.3 | 171.4 |

The changes in machine parameters from earlier designs are modest. Additional minor modifications will be made to take into account the asymmetry of the curve for the time of flight versus energy, the requirement that the number of turns be an integer plus one half (due to the injection/extraction scheme), to take into account the average effect of beam loading, to match the number of drifts for injection and extraction to the final requirements determined by the injection/extraction studies, and some other minor modifications to the modeling.

#### 3.5.5.2 Injection and Extraction

The current design parameters for injection and extraction are:

| Configuration | FDFC Inj. | FDFC Ext. | FCDC Inj. | FCDC Ext. | FDFCC Inj. | FDFCC Ext. |
|---|---|---|---|---|---|---|
| Plane | H | V | V | V | H | V |
| Kickers | 6 | 6 | 6 | 6 | 3 | 4 |
| Kicker B (T) | 0.103 | 0.103 | 0.113 | 0.101 | 0.089 | 0.078 |
| Septum B (T) | 3 | 4 | 3 | 4 | 2.5 | 4 |
| Kicker len. (m) | 1.4 | 1.4 | 1.4 | 1.4 | 2.4 | 2.4 |
| Cells needed | 8 | 8 | 8 | 5 | 5 | 6 |

These are updates of the values from the 2009 Particle Accelerator Conference [159] to use the new lattice parameters. Note that the kicker and septum parameters for the triplets with the longer drifts are considerably more favorable than in other configurations.

A superconducting septum similar to the one required for the shorter drift lattices (FDFC and FCDC) was used at Jefferson Laboratory [160].

Magnets in the injection and extraction regions will need to be larger than magnets in other places in the ring. Simulations indicate that the resulting symmetry breaking has only a modestly deleterious effect on the beam dynamics. The additional cost required for these magnets should be estimated.

The injection and extraction systems are clearly challenging. Some early engineering studies should be performed as soon as possible to ascertain the approximate fraction of the machine cost required for these systems and whether the parameters as outlined are achievable with current technology.

#### 3.5.5.3 Chromaticity Correction

Chromaticity correction will mitigate problems with the time-of-flight dependence on transverse amplitude. It will also allow for an alternative configuration where special sections with long drifts are introduced for injection and extraction, easing the requirements on the injection and extraction hardware and allowing for a more compact (and therefore efficient) lattice in the remainder of the ring.

Chromaticity correction has been studied with the updated lattice design. Nearly perfect correction of the chromaticity was achieved using sextupoles only. Unfortunately, the dynamic aperture was only 5 mm normalised. However, as in earlier studies, we expect that chromaticity can be partially corrected and give a more reasonable dynamic aperture. Two different insertions were tried with the FDFC lattice, the insertions having 4 m and 6 m drifts. Matching into the insertions worked well over the energy range.

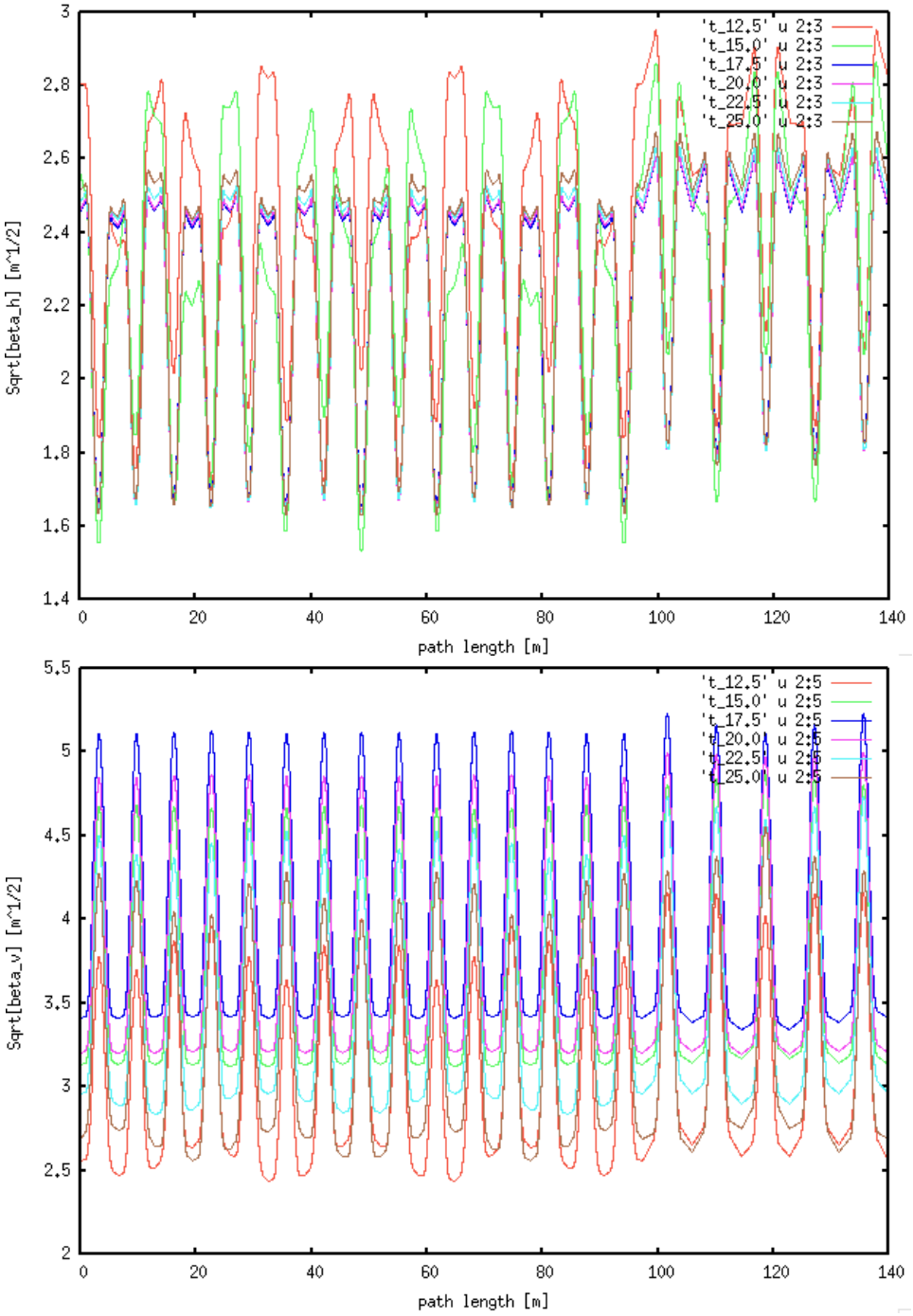


Figure 36: Beta functions for various momentum from 12.5 GeV to 25 GeV with 1.5 GeV step. (Top) Horizontal, (bottom) vertical. Chromaticity of the lattice is corrected with sextupole and 5 cells out of 20 cells have longer straights.

We should determine the approximate cost impact of using chromaticity correction. The lower tune used in the chromatically-corrected lattice will increase the magnet aperture and reduce the machine efficiency. Some chromaticity correction is probably advantageous; we should determine the appropriate amount. The goal will be to have modest cost impact and still maintain an acceptable dynamic aperture.

#### 3.5.5.4 Beam Loading

There are two primary effects of beam loading: bunches within a train having different energies, and different bunch trains having different energies. In the baseline scenario with three bunch trains per RF pulse, the energy spread within a bunch train is relatively modest (approximately 0.1%). This is significantly smaller than the energy spread within an individual bunch. If desired, even this energy spread could be corrected with a modest amount of RF after the last accelerating stage.

The energy difference between RF pulses is larger, but only rises to about 0.4% if the pulses arrive over a short period of time according to the original baseline. This source of spread is eliminated if the pulses arrive over 200 $\mu$s.

#### 3.5.5.5 Deciding Parameters for IDR

We must make final desicisions on the design parameters for the final system. Triplets appear to be the best choice, and the question becomes whether to use the long or short drift version. The long drift version gives a significant advantage for the time of flight dependence on transverse amplitude, while only incurring a 17% cost penalty over the short drift version. Furthermore, injection and extraction hardware has more reasonable parameters for the long drift version. Thus, this is appearing to be the better choice, though no final decision has been made on this point. Furthermore, we must decide how large of a sextupole component we wish to add to the machine and whether we would like to add long-drift insertions for injection and extraction.

### 3.6 Storage Ring

The race-track design has been chosen as the baseline for this study. In order to understand the machine properties of these storage rings the original optics has been adapted in the framework of the MAD-X code [161]. MAD-X allows an easy calculation of the Twiss parameters, determination of the working point and particle tracking used to infer the dynamic aperture of the machine. The structure of the ring is illustrated in figure 37 which shows the three main elements of the optics: straight sections, arcs and matching sections. The total length of this machine is 1608.8 m (600.2 m for each of the straight sections) with a central momentum of 25 GeV/c.

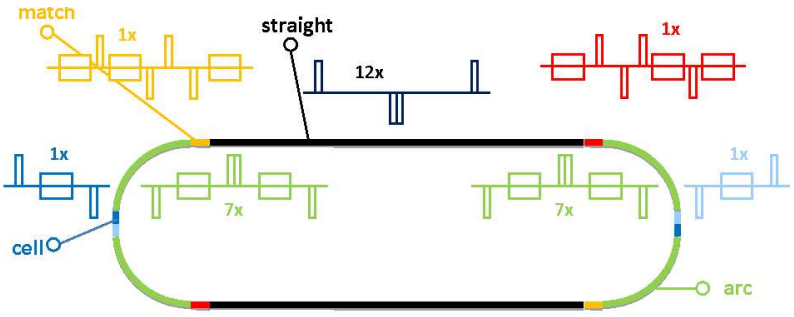


Figure 37: Schematic diagram of the Race Track decay ring illustrating its linear optics elements: (black) decay straights, (green/blue/cyan) arc sections, (red/yellow) matching sections.

### 3.6.1 Optical Parameters and Working Point

The optical parameters from MAD-X are shown in figure 38; it can be seen how the beta functions are kept low in the arcs to reduce the size of the beam and increase transmission, while their values are increased in the straight sections to reduce the divergence of the beam and make it negligible with respect to the divergence originating from muon decays. The merging of these two opposite behaviours is guaranteed by the matching sections. The optics for the decay ring is shown in figure 38. Figure 39 illustrates the phase advance along the ring: the working point is found to be ($Q_x$=8.5229,$Q_y$=8.2127). It should be stressed how a ±10% change in momentum

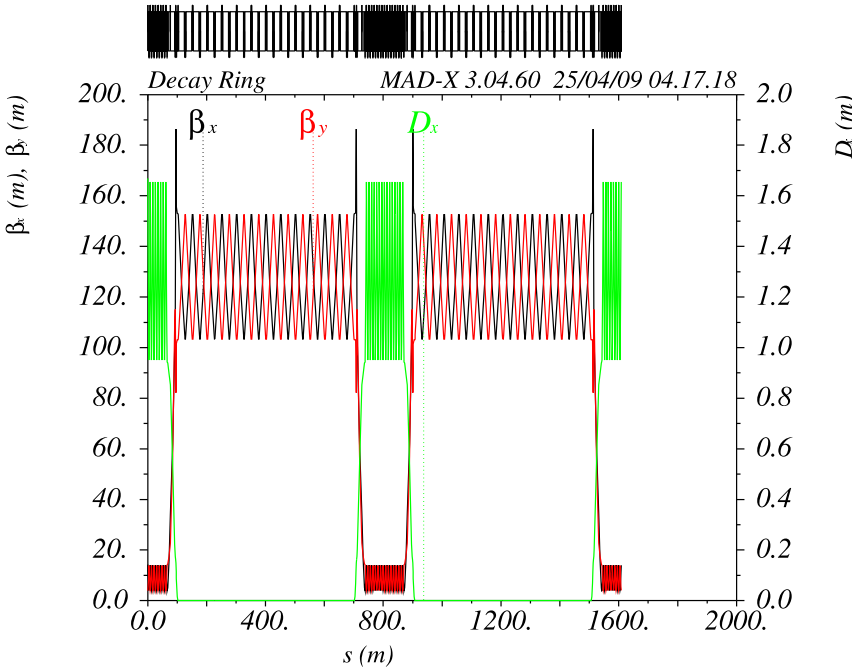


Figure 38: $\beta_x$ (black) and $\beta_y$ (red) functions for the decay rings. Their values are deliberately chosen high in the straight sections to reduce the divergence of the beam (see text). Dispersion in the arcs is also shown (green plot).

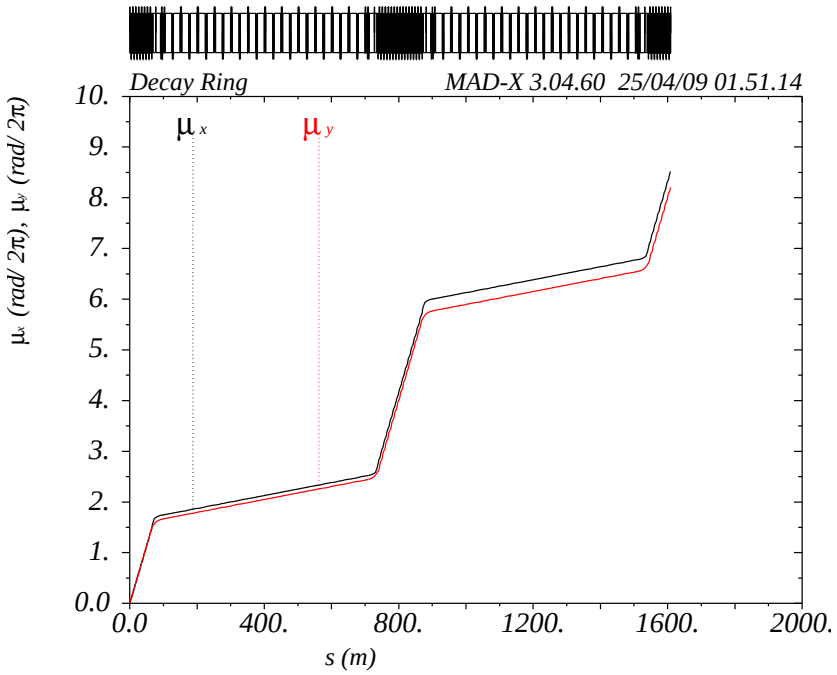


Figure 39: Phase advance over a period in the decay ring with a fast increase in the arcs due the small $\beta$ functions and a slow increase in the straights where $\beta$ functions are large.

causes the working point to move noticably in the ($Q_x$,$Q_y$) plane crossing resonances which could be detrimental for the stability of the beam. To mitigate this effect, one can introduce non-linear elements, like sextupoles in the dispersive arcs, and tune them to make the chromaticity plots flat. Chromaticity correction is motivated by the large momentum spread that may be introduced by transverse-longitudinal coupling in the FFAG system [158]. A visual summary of these results is shown in figure 40 where resonance diagrams and chromaticity plots are displayed.

### 3.6.2 Particle Tracking and Dynamic Aperture

Introduction of non-linear elements along the ring is advocated to mitigate resonance crossing effects, potentially catastrophic for a storage ring. However, two things should be stressed in the case of a muon ring: (a) at 25 GeV/c muons circulate on average fewer than 100 times in the 1608.8 m long ring before decaying; and (b) the sextupoles introduced in the optics create coupling between the transverse planes and reduce the dynamic aperture of the beam. Concerning point (a) the natural question that arises is whether it is important to avoid resonance crossing, given the relatively short beam lifetime required. The second aspect has been investigated to produce a more quantitative answer. The study has been carried out using the module *thintrack* of MAD-X and tracking particles checking whether they survive after a large number of turns. Prior to tracking, lattice magnets are sliced into 50 thin elements and the structure is re-matched to produce the same working point. Muon decays are not present in this simulation. After some trials we decided that a particle is stably confined in the lattice if it is not lost after

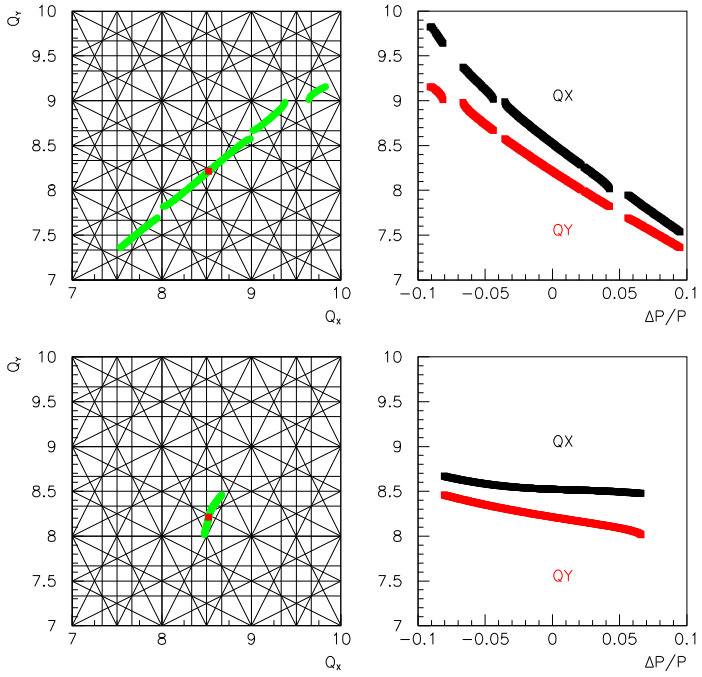


Figure 40: Upper section: linear optics configuration, showing the crossing of resonances (left) as a function of momentum displacement (green line): the red dot shows the working point. The natural chromaticity of the beam is shown on the right for both the transversal planes. Lower section: the effect of sextupoles is shown. Chromaticity is strongly reduced (right) and also the crossing of potentially dangerous resonances.

500 turns. The physical aperture of the ring is chosen arbitrarily high ($x$=$y$=1 m) in order to focus on the dynamic aspects of beam transport only. Muons are started in the mid-point of an arc with initial phase-space coordinates given by the formula $(x_{i=1,N},\, y_j,\, x'{=}0,\, y'{=}0)_{j=1,M}$.

If a muon is lost before 500 turns, the corresponding $(x, y)$ values are recorded. Figure 41 shows how increasing the initial $x$ (and therefore the associated amplitude) results in a loss of the muon (the physical aperture is chosen to be $x = y = 1$ m). We notice how the elliptical shape of the Poincaré plots is preserved and also how particle losses happen in a rather sudden way. With the introduction of non-linear elements phase space plots are distorted from the original ellipses, and $x - y$ correlation is visible in the blurred trajectories in both planes (figure 42). A summary of the dynamic aperture calculations is shown in figure 43.

### 3.6.3 Decay Rings Diagnostics

After assessing the general properties of the race-track lattice it was felt the importance for an investigation of the diagnostic of the decay rings. Three main topics have been identified:

- Energy monitoring;
- Beam current measurement; and
- Beam divergence measurement.

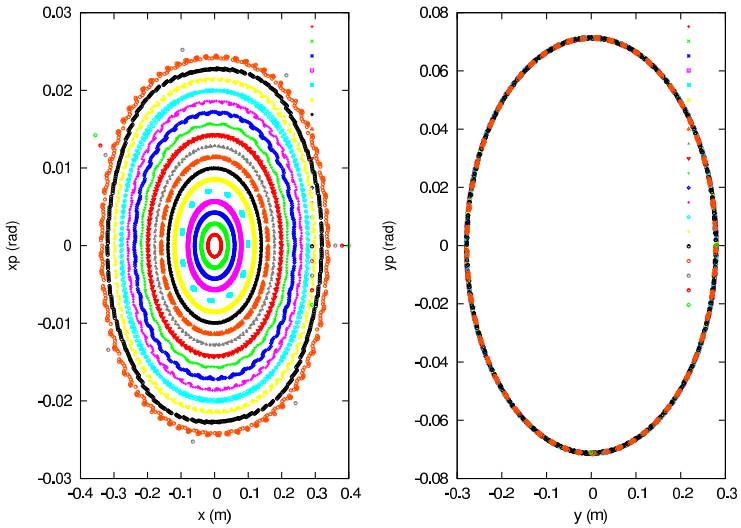


Figure 41: A scan in the $(x, x')$ phase space is shown with a fixed initial value ($y$=28 cm, $y'$=0), for the linear optics ring. The lefmost plot is a Poincaré map for the $(x, x')$ section, showing a behaviour very close to elliptical curves even for high beam radii. The evolution of the other transverse coordinates $(y, y')$ is totally decoupled, as can be inferred by the sharp ellipse in the right plot.

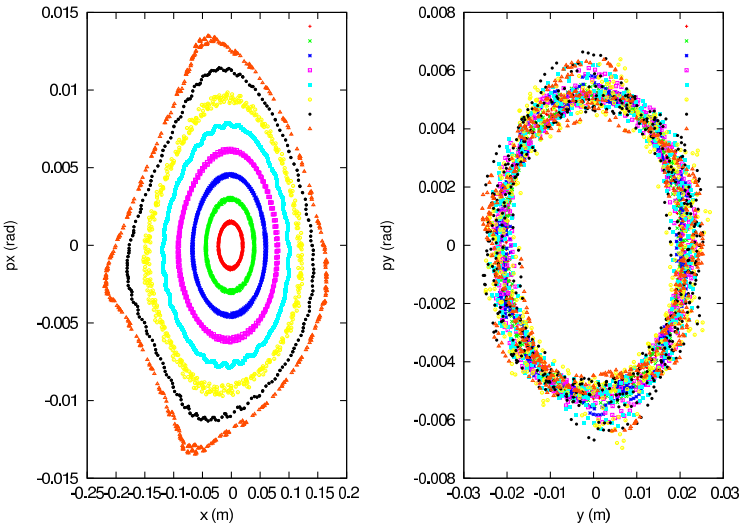


Figure 42: The meaning of the plots is the same as in figure 41 but the ring is now equipped with sextupoles to correct for chromaticity effetcs (see text). This results in highly non elliptical trajectories (leftmost Poincaré plot) and coupling between $x$ and $y$ planes, as can be inferred from the blurred trajectories.

The first item has been addressed since the IDS-NF meeting in Mumbai (October 2009). Some preliminary studies focus on the possibility of a beam energy monitoring based on the polarisation of the beam itself. In the hypothesis of a residual 27% polarisation of the muons a per-turn energy change in the electron spectrum can be measured which allows to evaluate both the central energy of the beam and its spread. A possible detector could be located on the inner side of

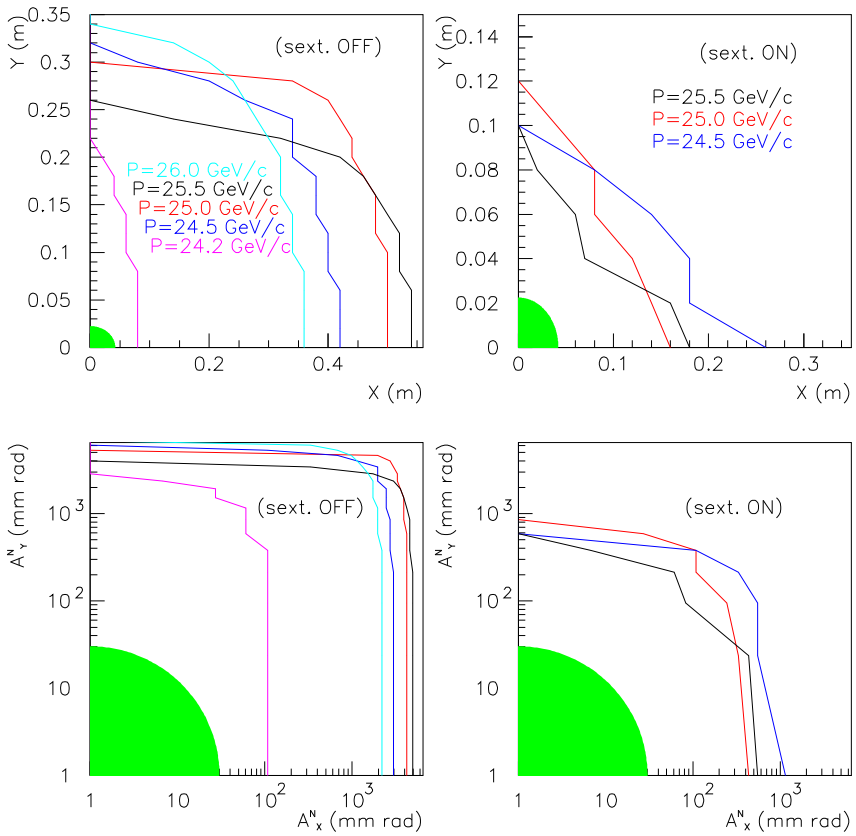


Figure 43: Dynamic Aperture for the Decay Ring: (left column) linear optics, (right column) sextupoles introduced in the lattice. (Top) contour plots defining the maximal radius for a particle injected in the middle point of an arc before being lost in the lattice. In off-momentum cases this radius is generally reduced. The green area represents the beam size corresponding to the nominal acceptance (30 mm rad). Points on the contour plots $(R_x, R_y)$ are used to define the amplitudes in the two transversal planes ($A_x^N$,$A_y^N$), where $(A_i^N = \frac{P}{m_\mu} R_i^2/\beta_i)_{i=x,y}$ (bottom). In this case the green area marks the 30 mm rad fiducial acceptance.

a bending dipole following the straight section of the ring. While first results seem interesting and encourages the pursuit of the study, a lot still needs to be understood and improved. The Geant4 based code used for the study (G4Beamline [162]) has been combined with a newly written model of the spin-polarisation effects. The use of other codes incorporating spin effects (Zgoubi [163]) is presently being considered for a more realistic description of the physics. Figure 45 illustrates the energy oscillations for the total detected electron energy at every turn. The oscillating pattern (due to spin precession) is combined to the decay of the muon and can be parametrised by a function:

$$f(T) = N_0 e^{-BT}(Ce^{-(GT^2)}cos(D + ET) + F)\,; \tag{10}$$

where the relevant parameters are $G$ (containing $\Delta$P/P), $E$ (the spin tune from which $\gamma$ can be inferred and $B$ (describing the muon decay slope). A general view of the decay ring in the G4Beamline rendering is illustrated in figure 44, while a close up of the matching section is shown in figure 46.

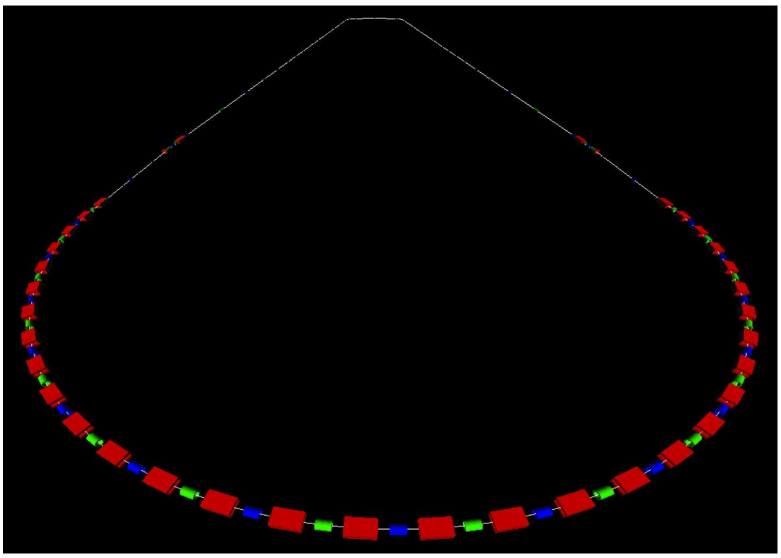

Figure 44: A perspective view of the Race Track Decay Ring in G4Beamline. Colour convention: (red) dipoles, (blue) focussing quadrupoles, (green) defocussing quadrupoles, (yellow) virtual detectors for tracking studies.

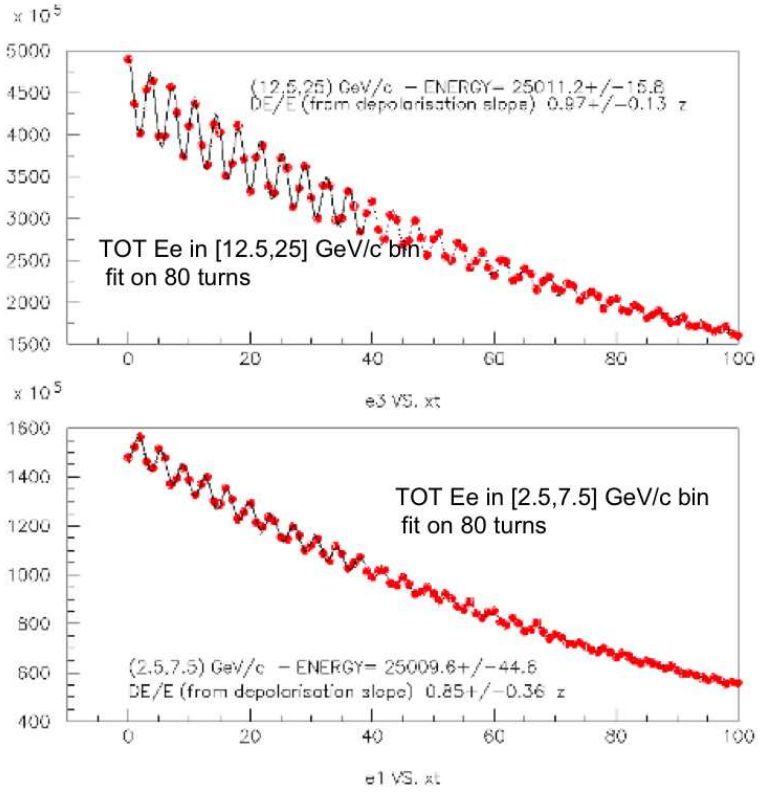


Figure 45: Effect of spin precession on the decay electron energy spectrum. The plots in the figure show the total electron energy for a defined energy slot as a function of the beam turn (top) electrons in the energy range [12.6,25.0] MeV/c, (bottom) electrons in the energy range [2.5,7.5] MeV/c. A it to the curve described in XXX is done over the first 80 turns.

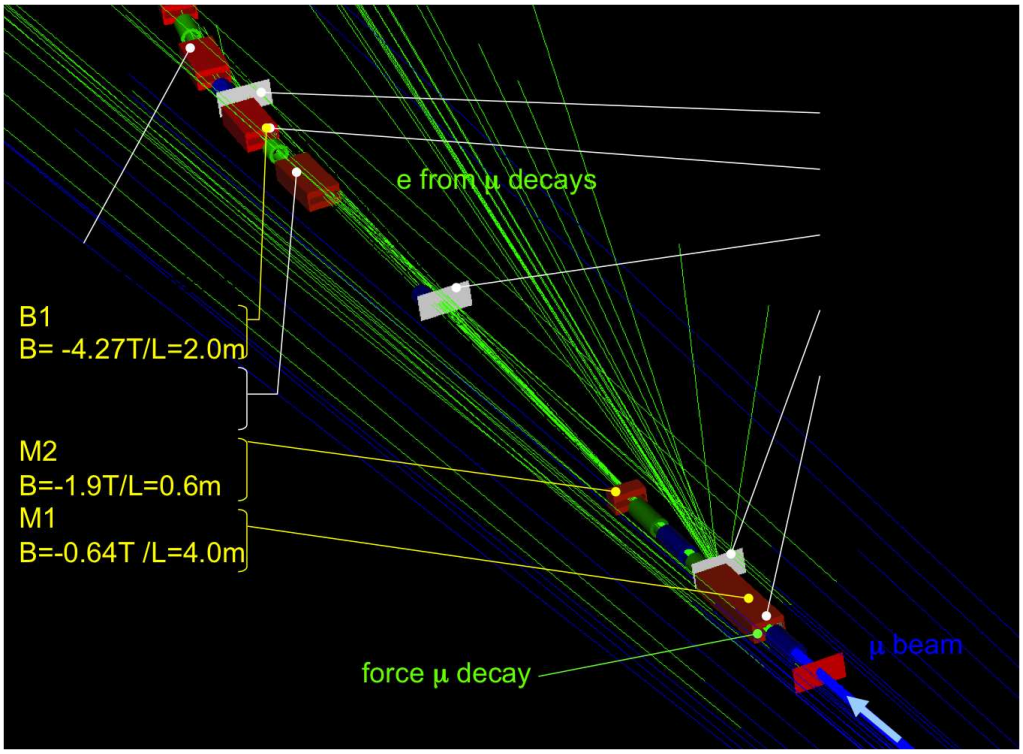


Figure 46: Expanded view of the matching section showing a beam of muons (blue) decaying into electrons(green) bent by the dipole elements.

# 4 Detector Working Group

## 4.1 Overview

The detector group of the International Scoping Study of a future Neutrino Factory and superbeam facility (the ISS) [43] set out to determine the baseline detector options for each of a number of possible future neutrino beams and to define a research and development (R&D) plan necessary to develop those detector options. The baseline detector options that have been adopted by the International Design Study for a Neutrino Factory (muon energy between 25 GeV) is a 100 kton magnetized iron neutrino detector (MIND) for the wrong sign muon final states (golden channel). The possibility of the inclusion of $\sim$ 10 kton of a hybrid neutrino magnetic emulsion cloud chamber (NM-ECC) detector for wrong sign tau detection (silver channel) is being retained. The optimum strategy to measure $\delta_{CP}$, $\theta_{13}$ and the mass hierarchy (the sign of $\Delta m^2_{13}$) includes having two magnetised iron detectors, one at $\sim$ 4000 km and another at the magic baseline of $\sim$ 7500 km, rather than the silver $\nu_\tau$ appearance channel (see section 2.2.3). Non standard interactions in the $\nu_\tau$ detection process would require a $\nu_\tau$ detector at a $\sim$ 4000 km, while non-standard $\tau$ and $\nu_\tau$ production can be most efficiently observed in a near detector with $\nu_\tau$ detection capabilities. This would be the main argument to preserve $\nu_\tau$ detectors in the baseline.

Furthermore, there are possibilities of detector technologies that go beyond the baseline, which

could potentially achieve improved performance in the measurement of the oscillation parameters if these detectors are found to be feasible and affordable. They include platinum detectors (to measure $\nu_e$ appearance): a magnetised Totally Active Scintillator Detector or a large (100 kton) magnetised Liquid Argon detector.

The near detector options also need to be studied, but these need to be defined for each of the neutrino beam options. Current near detector technologies, such as those adopted for the T2K ND280 detector [164] or the Minerva [165] detectors are possible options, but the final choice will depend on the far detector chosen. What is clear is that a near detector needs to carry out at least three tasks: measurement of neutrino flux, measurement of neutrino cross-sections and measurement of charm production from neutrino interactions, which remains the main background to the wrong-sign neutrino oscillation signal.

The ISS laid the foundations to proceed towards a full International Design Study for a Neutrino Factory. In this section of the progress report, we will describe the most recent developments in defining the performance for a Magnetised Iron Neutrino Detector (section 4.2), which includes for the first time an analysis using full reconstruction and pattern recognition. section 4.3 describes the simulation carried out to determine the performance of a Totally Active Scintillating Detector (TASD), section 4.4 describes the necessary R&D to be able to build a large Liquid Argon detector and section 4.5 describes how the flux measurement can be carried out at a near detector at a Neutrino Factory.

## 4.2 Magnetised Iron Neutrino Detector

### 4.2.1 Introduction

Early papers on the physics outcomes of a Neutrino Factory concentrated on the sub-dominant $\nu_e \rightarrow \nu_\mu$ oscillation [166] in which a muon of opposite charge to that stored in the storage ring (wrong-sign muon) would be produced in a far detector by the charge current (CC) interactions of the oscillated $\nu_\mu$. The first analysis of the capabilities of a large magnetised iron detector to detect the wrong-sign muon signature was discussed in [68] (termed the Golden Channel), where it was demonstrated that this combination was capable of the extraction of the remaining unknown parameters in the neutrino sector, the third mixing angle $\theta_{13}$ of the Pontecorvo-Maki-Nakagawa-Sakata (PMNS) matrix [167–169] and the $CP$ violating phase $\delta_{CP}$.

The Magnetised Iron Neutrino Detector (MIND) is a large scale iron and scintillator sampling calorimeter. As a result of the studies mentioned above it is considered the baseline detector for a Neutrino Factory storing muons in the energy range 20-50 GeV [43]. Under the remit of EUROnu [170] and the International Design Study for a Neutrino Factory [5] all aspects of possible future neutrino beam facilities including accelerator, detectors and physics must be studied and compared to select the best option to determine the remaining oscillation parameters.

Previous studies of MIND focused on the topology and kinematics of neutrino events in the detector, assuming perfect pattern recognition. By smearing the kinematic variables of the

participant muon and hadronic shower it was demonstrated that using a combination of cuts on the relative length of the two longest particles in the event and the momentum and isolation of this candidate, high signal identification efficiency and background suppression could be achieved [171, 172]. However, a full study without such assumptions is necessary to fully characterise the detector response.

While MIND is essentially a large scale version of the MINOS detector [173], the nature of the Neutrino Factory beam – containing 50% $\nu_e$ and 50% $\overline{\nu}_\mu$ in the case of stored $\mu^+$ – means that the optimisation of the analysis is somewhat different. Incorrect charge assignment (charge misidentification) of non-oscillated $\overline{\nu}_\mu$ CC interactions present a significant possible background in this beam configuration, in addition to backgrounds from meson decays in the hadronic shower and misidentification of neutral current (NC) and $\nu_e$ CC events.

The study carried out in this section [174] re-visits the problem by taking an un-biased look at the visible part of a large sample of neutrino interactions – generated using the same GEANT3 [175] simulation as in the above mentioned studies with a uniform distribution in neutrino energy – and developing pattern recognition algorithms (first presented in [176]) – described in section 4.2.3 – to extract a candidate muon for fitting using a Kalman filter. Successful fits are then subject to offline analyses – described in section 4.2.4 – to determine the validity of those wrong sign candidates. Analysis results are presented in Sec 4.2.5.

### 4.2.2 MIND parameterisation and expected event yields

For the purpose of the study, MIND is a cuboidal detector of 14 m × 14 m cross-section and 40 m length, segmented as 4 cm of iron and 1 cm of plastic scintillator for a total mass of ∼51.0 ktonnes. A dipole magnetic field of mean induction 1 T in the transverse plane provides the field neccessary for charge and momentum

In the first part of the analysis, event vertices were generated centred in the detector plane at 1.5 m from the front of the detector in the beam direction ($z$) in order to study the nature of the backgrounds without detector edge effects. section 4.2.4 discusses the expected fiducial effects when a more realistic randomly generated vertex is considered.

At a MIND placed 4000 km from the neutrino source and assuming the current best global fit oscillation parameters: $\theta_{12} = 33.5°$, $\theta_{13} = 5.7°$, $\theta_{23} = 45°$, $\Delta m^2_{21} = 7.65 \times 10^{-5}$ eV$^2$, $\Delta m^2_{32} = 2.40 \times 10^{-3}$ eV$^2$ [1], setting $\delta_{CP} = 45°$ and calculating matter effects using the PREM model [177], the expected total number of interactions due to $10^{21}$ $\mu^+$ decays at 25 GeV energy would be of order those shown in table 4.

| $\overline{\nu}_\mu$ CC | $\nu_e$ CC | $\overline{\nu}_\mu + \nu_e$ NC | $\nu_\mu$ (Signal) |
|---|---|---|---|
| $1.22 \times 10^5$ | $3.34 \times 10^5$ | $1.48 \times 10^5$ | $5.56 \times 10^3$ |

Table 4: *Expected absolute number of interactions in a 51 ktonne MIND at a distance of 4000 km from a Neutrino Factory storage ring with 25 GeV muons.*

Thus in order to successfully extract oscillation parameters from the golden channel, potential backgrounds from non-signal interactions must be suppressed to at most the $10^{-3}$ level in absolute terms. Moreover, the existence of possible degenerate solutions due to uncertainty in the measured parameters and due to the nature of the oscillation probability (see [178, 179]) means that spectral information is required to determine $\delta_{CP}$ reliably. This additional requirement dictates that backgrounds must be suppressed to below $10^{-3}$ in each energy bin while maintaining an efficiency threshold below 5 GeV so that information on the rise of the first oscillation maximum is available.

### 4.2.3 Reconstruction tools

The reconstruction package was used to analyse a large data set comprised of Deep Inelastic Scattering (DIS) neutrino interactions of $\overline{\nu}_\mu$ and $\nu_e$ generated by the LEPTO61 [180] package and tracked through the GEANT3 simulation of MIND. Considering CC interactions of $\overline{\nu}_\mu$ and $\nu_e$ with a dedicated study of events containing wrong sign muons from meson decay in $\nu_\mu$ CC and NC interactions the main expected backgrounds were studied.

Each event considered comprised all three dimensional points with their associated energy deposit, which were recorded in the scintillator sections of the MIND simulation, with the *x,y* position of these hits smeared according to a $\sigma = 1$ cm Gaussian before analysis began.

*Muon candidate extraction*

After ordering the hits from smallest to greatest $z$ position[2] in the detector the first step of the reconstruction was to extract a candidate muon from the event. Two methods were employed to perform this task depending on the event topology: a Kalman filter incremental fit was used to extract candidates from those events with one particle clearly longer than the others (described in section 4.2.3), while a Cellular Automaton method was used in those events not viable for reconstruction through the first method (see section 4.2.3). The criterion for the first category was that the five planes with activity furthest downstream should contain no more than one hit per plane.

*Kalman Filter candidate extraction*

Using the Kalman filter algorithm provided by RecPack [181] it is possible to propagate the track parameters back through the planes using a helix model, which takes into account multiple scattering and energy loss. Since, in general, a muon will act as a Minimum Ionising Particle (MIP) and will travel further in the detector than the hadronic particles, those hits furthest downstream can be assumed to be muon hits and used as a seed for the Kalman filter. The seed state is then propagated back to each plane with multiple hits and the matching $\chi^2$ to each of the hits is computed. Hits with matching $\chi^2$ below 20 are considered and in each plane the one with the best matching among these is added to the trajectory and filtered (the track

[2] The coordinate axis is such that the $z$ axis points along the beam direction, the $y$ axis is perpendicular to the $z$ axis, pointing upward, and the $x$ axis completes a right-handed coordinate system

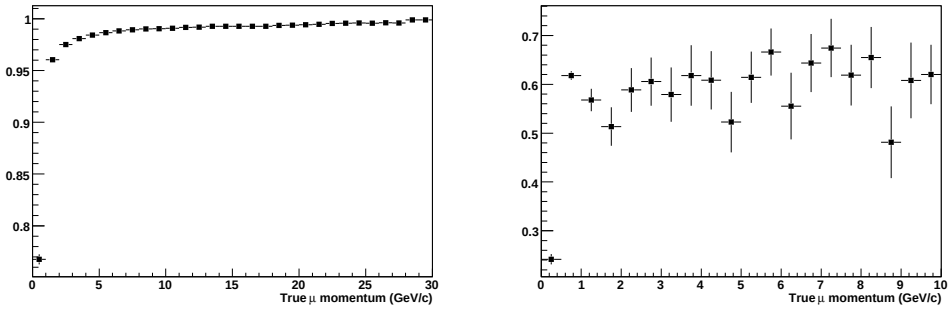


Figure 47: *Muon candidate purity as a function of true muon momentum for i) the Kalman filter extraction method and ii) the Cellular automaton method.*

parameters are updated with the new information). All accepted hits constitute the candidate muon and are presented for fitting (section 4.2.3), with the remaining hits being considered as hadronic activity. figure 47-(left) shows the fraction of true muon hits in the candidate when using this method.

*Cellular Automaton candidate extraction*

Events with high four-momentum transfer, $Q^2$, transfer or low neutrino energy can tend to be rejected by the first method, since in general the muon will not escape the region of hadronic activity. In order to recover these events a second method is employed. The Cellular Automaton method (based on the method described in [182]) uses a neighbourhood function to first rank all the hits and then form all viable combinations into possible trajectories.

A 'neighbour' is defined as a hit in an adjacent plane within a pre-defined transverse distance of the projection into that plane of the straight line connecting hits in the previous two planes. Starting from the plane with lowest $z$ position, hits are given a rank one higher than their neighbour in the previous plane should they have one. Trajectories are then formed from every possible combination of one hit per plane starting with those of highest rank using the neighbourhood function with a stricter condition.

Those trajectories formed using this method are then subject to a number of tests to determine which is most likely to be a muon. After having a basic helix fit performed and being assessed according to their length, trajectories are rejected for being short, having high $\chi^2$ fit or high relative curvature error (described in section 4.2.4). The candidate muon is then selected as the longest remaining trajectory with the lowest $\chi^2$. All other hits in the event are considered to be from hadronic activity. figure 47-(right) shows the purity of the candidate when using this method.

*Candidate fitting*

All candidates successfully extracted from their event that have greater than six hits are presented to the fitter as a candidate muon. The same Kalman filter algorithm is used here as in section 4.2.3. Fitting the candidate iteratively improves seeding and thus using a more

constricted $\chi^2$ condition than in the pattern recognition, the maximum number of successful, reliable fits were achieved.

With the trajectory hits ordered in increasing $z$ position, a least squares quartic fit was performed on the section outside the planes where there was hadronic activity. This fit was used to estimate the slopes in $x$ and $y$ and the momentum of the candidate, to be used as a seed for the Kalman filter helix fit in the forward direction. The matching $\chi^2$ was once again checked at each hit. Hits with greater than the pre-determined maximum (20) were ignored. In addition, the filtering process only allows a pre-determined maximum number of hits (5) to be ignored. Should this number be reached, the filtering process is aborted and the smoother uses only those hits up to this point in the candidate. This method efficiently rejects hits beyond any large angle scatter which could cause charge misidentification. Successful fits were re-seeded with the state vector at the first fitted hit and a scalar multiple (5) of the corresponding covariance matrix (taking only the diagonal elements) and then refitted.

Failed fits and those with less than 50% of their hits fitted are then fitted again in the backwards direction using the seed from the pattern recognition. Two iterations are once again performed, with successful fits being accepted and those which are unsuccessful reverting to the result of the original fit.

The result of a fit being the track parameters at the projection to the event true vertex $z$ position (3-momenta, position and charge).

*Hadronic reconstruction*

The hadronic activity must be used to reconstruct the energy of the hadronic shower in order to ultimately reconstruct the energy of the interacting neutrino. In the absence of a well developed algorithm to perform this task, the current study assumes reconstruction of the hadronic energy $E_{had}$ with a resolution $\delta E_{had}$ equal to that recorded by the MINOS CalDet testbeam [173, 183]:

$$\frac{\delta E_{had}}{E_{had}} = \frac{0.55}{\sqrt{E_{had}}} \oplus 0.03. \tag{11}$$

It was demonstrated in [68] that a cut based on the isolation of the muon candidate from the hadronic shower was a powerful handle for the rejection of hadronic backgrounds. This isolation was measured via the $Q_t$ variable:

$$Q_t = P_\mu \sin^2 \vartheta, \tag{12}$$

where $P_\mu$ is the muon momentum and $\vartheta$ is the angle between the muon and the resultant hadronic vector. This requires the reconstruction of the direction vector of the shower. The Monolith test-beam [184] measured an hadronic angular resolution described by:

$$\delta\theta_{had} = \frac{10.4}{\sqrt{E_{had}}} \oplus \frac{10.1}{E_{had}} \tag{13}$$

for a similar detector. This parameterization was used to smear the hadron shower direction vector, which in combination with the reconstructed muon momentum and direction (see section 4.2.3) were use to compute the $Q_t$ variable defined above.

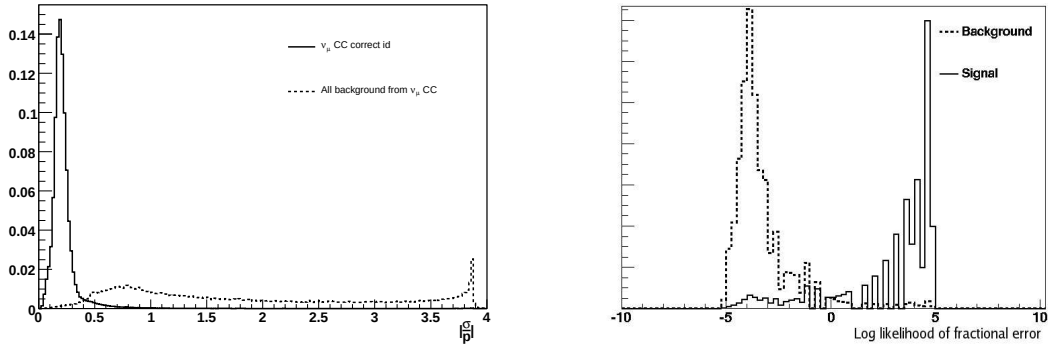


Figure 48: *i)* $\frac{\sigma_{q/p}}{q/p}$ *likelihood for signal and background from* $\overline{\nu}_\mu$ *CC, and ii)* $\frac{\sigma_{q/p}}{q/p}$ *log likelihood ratio* ($\mathcal{L}_{q/p}$).

### 4.2.4 Analysis tools and cuts

As mentioned in section 4.2.1 there are four main possible sources of background to the wrong sign muon search: incorrect charge assignment and high energy wrong sign muons from meson decays in $\overline{\nu}_\mu$ CC events, and NC and $\nu_e$ CC events wrongly identified as $\nu_\mu$ CC. In order to reduce these backgrounds while maintaining good efficiency a number of offline cuts were employed. They can be organised in four categories: i) muon candidate quality cuts, ii) $\nu_\mu$ CC selection cuts, iii) fiducial cuts and iv) kinematic cuts.

*Muon candidate quality cuts*

These cuts are related to the quality of the candidate track fit and the determination of its curvature. Two observables are considered: the $\chi^2$ probability of the Kalman filter fit and the relative error of the determined curvature ($\frac{\sigma_{q/p}}{q/p}$). The first helps in rejecting high angle scatters or muon candidates with a large contamination from hadronic hits. The second variable is related to the probability of misidentifying the charge, and shows significant separation for correct and incorrect charge assignments as shown in figure 48-(left).

It is possible to reject a large portion of possible backgrounds using sequential cuts on these two variables:

$$\left|\frac{\sigma_{q/p}}{q/p}\right| < 0.7 \text{ and } \chi^2_{prob} > 0.9999\,; \tag{14}$$

where $\chi^2_{prob}$ is the $\chi^2$ probability as calculated in the TMath class of the ROOT framework [185]. However, a slightly better rejection is found when the relative error cut is substituted by a cut on the log likelihood ratio of $\frac{\sigma_{q/p}}{q/p}$ for signal and background (see figure 48-(right)):

$$\mathcal{L}_{q/p} > 2 \text{ and } \chi^2_{prob} > 0.9999. \tag{15}$$

*$\nu_\mu$ CC selection cuts*

The discrimination between $\nu_\mu$ CC and NC interactions relies on three easily available or calculable parameters, which are those of the extracted muon candidate. Due to the similarity

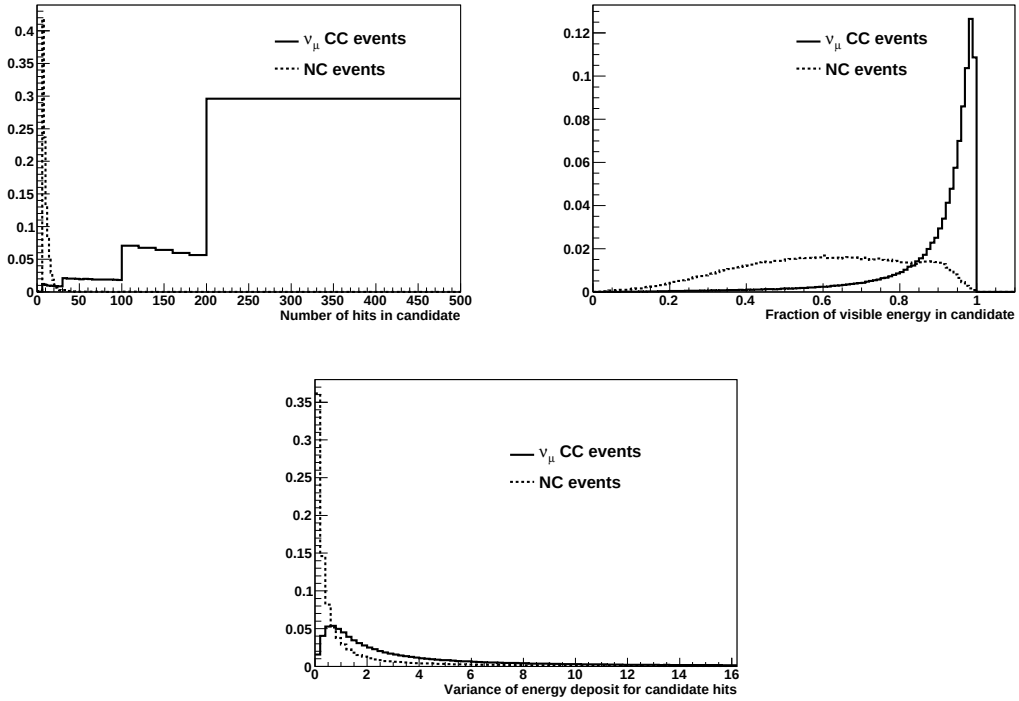


Figure 49: *PDFs of the three parameters used for NC/CC likelihood separation. i) Number of hits in candidate $l_{hit}$, ii) Fraction of visible energy in candidate $l_{frac}$ and iii) Variance of energy deposit in candidate $l_{var}$.*

of MIND and MINOS the parameters employed in the MINOS analysis [186] were used. Using a high statistic data set with knowledge of the true nature of each event, distributions of these three parameters for both NC and CC events were formed into PDFs (or likelihoods).

The first parameter was the length of the candidate in terms of the number of hits which form it ($l_{hit}$). This variable takes advantage of the nature of the muon as a penetrating particle and shows clear separation between $\nu_\mu$ CC and NC events (see figure 49-(top-left)).

The second parameter is the fraction of the total visible energy in the event which is in the candidate ($l_{frac}$). This parameter is not useful for all events due to the high probability for both NC and CC events to have a fraction very close to or equal to one. Thus, events that fall into this category, low $Q^2$ CC events or single pion production NC predominantly, are excluded from this distribution and do not use this parameter in their analysis. Here, while NC events demonstrate the full spectrum of possible values, signal events tend to be more concentrated at high fractions (see figure 49-(top-right)). However, high $Q^2$ CC events will tend to exhibit NC like behaviour.

While the third parameter used by MINOS is the mean energy deposited per plane for the candidate, the current simulation setup of MIND does not exhibit sufficient separation in this parameter for effective analysis. Thus, in place of this parameter the variance of the deposit is used ($l_{var}$), shown in figure 49-(bottom).

The likelihood ratio for each of the three observables was computed and combined in three

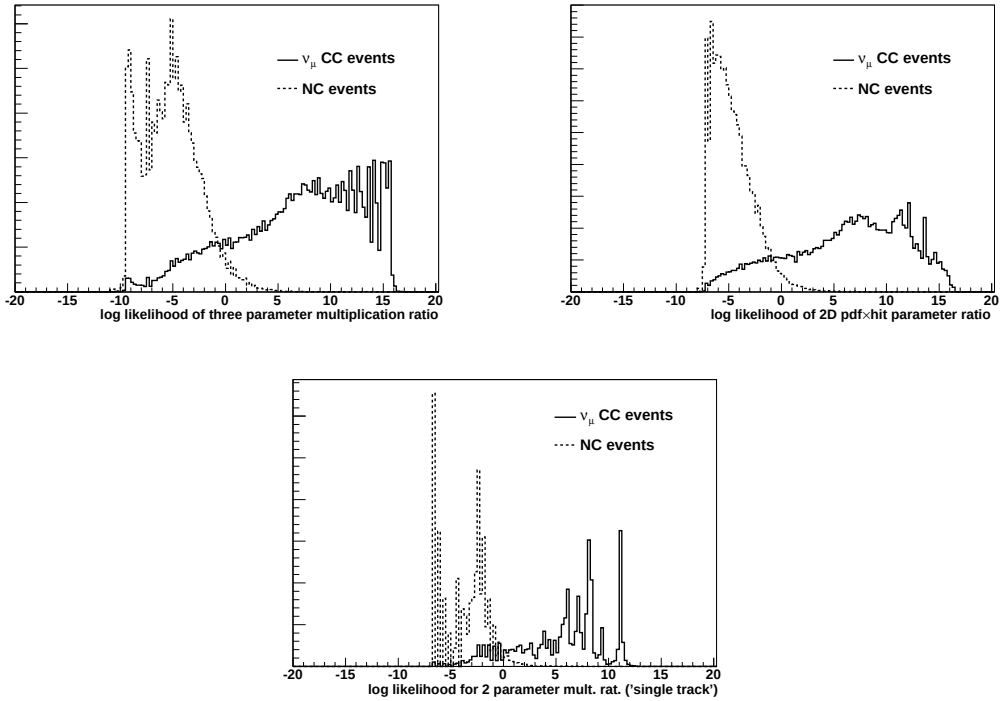


Figure 50: *Log likelihood discriminator distributions for energy fraction <0.999, i) $\mathcal{L}_1$, defined in equation 16, ii) $\mathcal{L}_2$, defined in equation 17 and iii) for energy fraction $\geq$ 0.999, $\mathcal{L}_3$, defined in equation 18.*

main log likelihood discriminators described in equations 16 to 18:

$$\mathcal{L}_1 = \log\left(\frac{l_{hit}^{CC} \times l_{frac}^{CC} \times l_{var}^{CC}}{l_{hit}^{NC} \times l_{frac}^{NC} \times l_{var}^{NC}}\right) \quad (16)$$

$$\mathcal{L}_2 = \log\left(\frac{l_{2D}^{CC} \times l_{hit}^{CC}}{l_{2D}^{NC} \times l_{hit}^{NC}}\right) \quad (17)$$

$$\mathcal{L}_3 = \log\left(\frac{l_{hit}^{CC^{frac=1}} \times l_{var}^{CC^{frac=1}}}{l_{hit}^{NC^{frac=1}} \times l_{var}^{NC^{frac=1}}}\right) \quad (18)$$

$\mathcal{L}_1$ is formed from the multiplication of the likelihoods mentioned above while $\mathcal{L}_2$ is formed by the multiplication of the $l_{hit}$ likelihood and a 2 dimensional likelihood of the variance and energy fraction ($l_{2D} = l_{hit} : l_{frac}$). $\mathcal{L}_1$ or $\mathcal{L}_2$ are used when the energy fraction is less than 0.999 and $\mathcal{L}_3$ otherwise. Distributions of these discriminators for samples of $\nu_\mu$ NC and CC events are shown in figure 50.

*Fiducial cuts*

Events originating near the edges of the detector can leave the sensitive volume. This will result not only in the loss of event energy and thus worsened energy resolution but, due to the shortening of the event, can cause a misidentification of the charge of a candidate. While the shortening of the event has the potential to reduce backgrounds from NC and $\nu_e$ CC as there should be less viable candidates, viable signal can also be lost, with a corresponding increase in

charge misidentification background. Therefore, it is reasonable to apply a fiducial volume cut so that these pathologies are minimised. Specifically, events are rejected should their candidate have both its first hit within 50 cm of the sides or back of the detector and its last within 10 cm. In section 4.2.5, the edge effects and their suppression are presented using $\overline{\nu}_\mu$ CC events as a model since they should affect little or no increase on NC and $\nu_e$ CC backgrounds and any small variation should be of the same spectral form as those seen in $\overline{\nu}_\mu$ CC events.

*Kinematic cuts*

Considering the remaining signal and background after applying all cuts described above, the $Q_t$ (see section 4.2.3) and muon candidate momentum ($P_\mu$) distributions are those shown in figure 51. A clear separation between signal and background events is observed. In particular, background events are concentrated at very low $Q_t$, while the signal exhibits much larger $Q_t$ values. In order not to reduce the efficiency at low neutrino energy, cuts on these two variables are only applyed for reconstructed neutrino energy ($E_\nu$) above 7 GeV. The applyed cuts are those of equation 19:

$$P_\mu \geqslant 0.2 \cdot E_\nu \quad \text{and} \quad Q_t > 0.25 \text{ GeV/c} \quad \text{for } E_\nu > 7 \text{ GeV}. \tag{19}$$

*Summary of analysis cuts*

As will be dicussed in the next section the most succesful set of cuts is given below in table 5.

| Cut type | Cut value |
|---|---|
| Fiducial | if $\lvert r_i^{first} - r_i^{det}\rvert \leqslant 50\ cm$, $\lvert r_i^{last} - r_i^{det}\rvert > 10\ cm$ for $r_i = x, y, z$ |
| Track quality | $\mathcal{L}_{q/p} > 2.0$ and $\chi^2_{prob} > 0.9999$ |
| $\nu_\mu$ CC selection | $\mathcal{L}_1 > 0$ for $l_{frac} < 0.999$<br>$\mathcal{L}_3 > 0$ for $l_{frac} \geq 0.999$ |
| Kinematic | $P_\mu \geqslant 0.2 \cdot E_\nu$ and $Q_t > 0.25$ for $E_\nu > 7\ GeV$ |

Table 5: *Summary of analysis cuts.*

### 4.2.5 Analysis Results

Using a large data set and the analyses described above the efficiency and rejection power of MIND has been studied.

*$\overline{\nu}_\mu$ charge current interactions*

The background from $\overline{\nu}_\mu$ interactions can be separated in two different contributions: i) fake wrong-sign muons from charge misidentification of the primary muon (mainly) and from pion to muon confusion, and ii) true wrong-sign muons from the decay of hadrons.

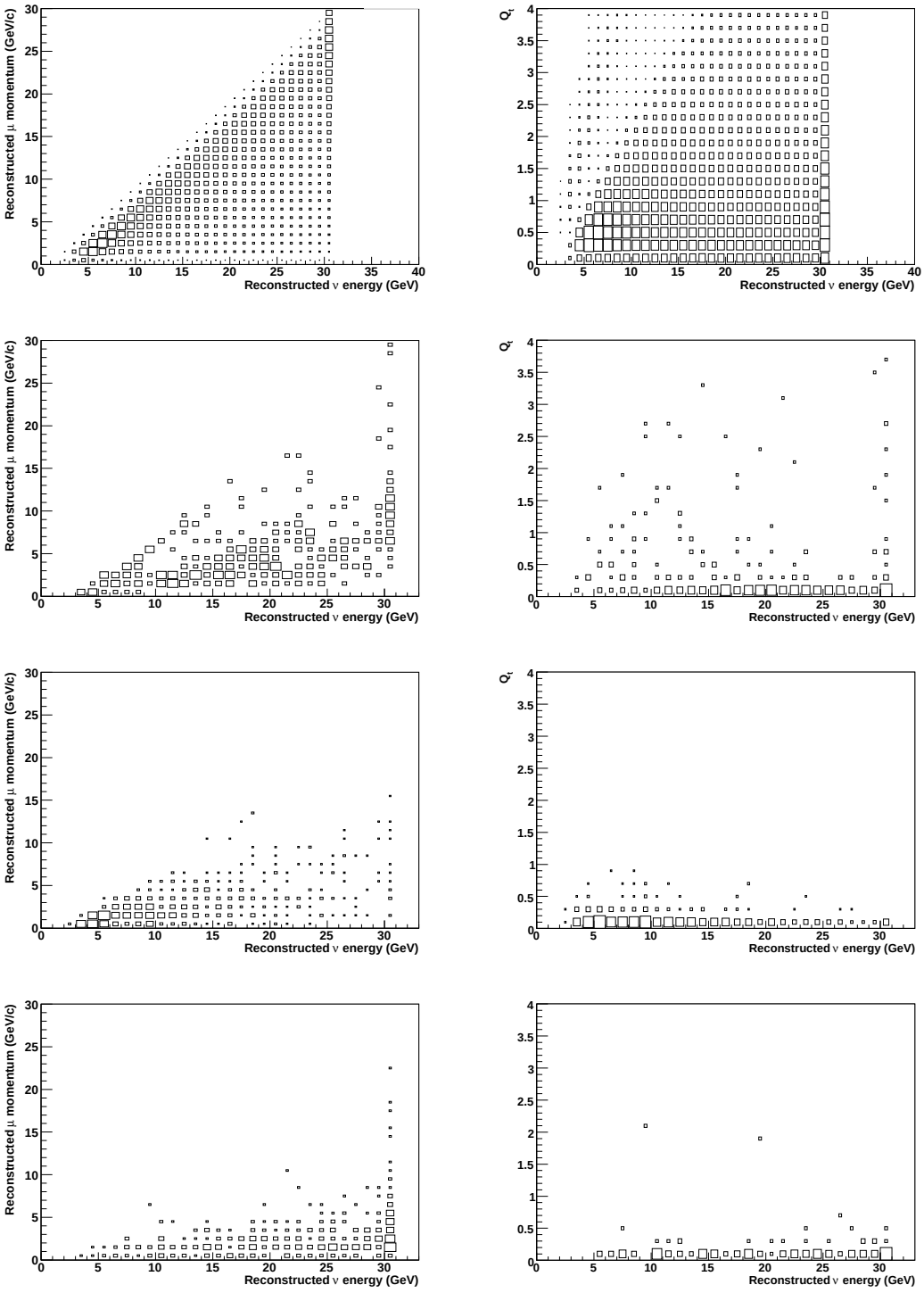


Figure 51: *Distributions of kinematic variables: Reconstructed muon momentum (left) and $Q_t$ variable in GeV/c units (right) versus reconstructed neutrino energy, for (top→bottom) signal, overline$\nu_\mu$ CC backgrounds, NC and $\nu_e$ CC.*

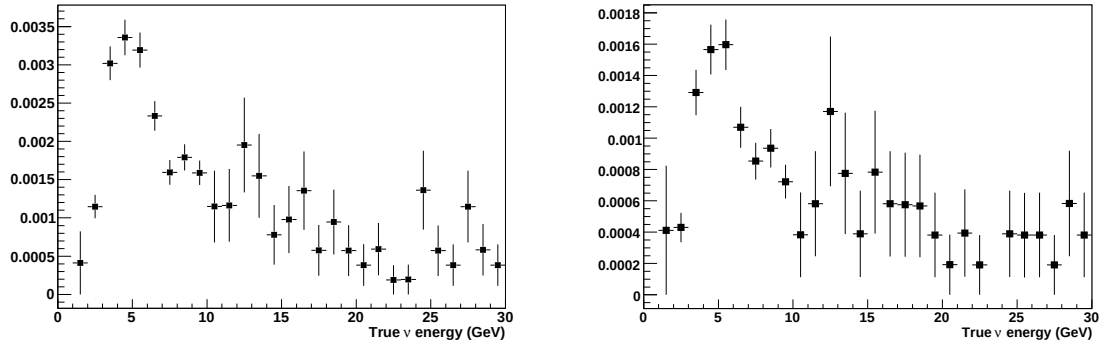


Figure 52: *Charge mis-assignment and hadron to muon mis-identification background i) with track quality cuts only and ii) including $\nu_\mu$ CC selection cuts.*

*Incorrect charge assignment*

The charge misidentification background was studied using $\overline{\nu}_\mu$ interactions where events containing hadronic decays to $\mu^-$ were excluded to be considered separately (section 4.2.5). An event is considered background if a candidate is successfully extracted and fitted with charge opposite to that of the true primary muon. Background events are mainly due to incorrect charge assignment to the true primary muon (due to multiple scattering or impurity of the candidate), but have a small contribution from penetrating hadrons (mainly pions) which are identified as muon candidates when the true primary muon has low momentum and is not correctly identified.

As shown in figure 52-(left) this background can be efficiently suppressed by cutting on the track quality variables, described in section 4.2.4. Further rejection is obtained by applying $\nu_\mu$ CC selection cuts (see figure 52-(right)).

*Wrong sign muons from hadron decays*

The production and decay of negatively charged mesons in the hadronic part of a DIS interaction has high probability to produce a $\mu^-$. Particulary mesons containing charm will decay promptly and produce high energy muons which can be selected as primary muon candidates when the true primary muon is not correctly identified (in general when it has low momentum). Suppression of this background is particulary important due to the high level of uncertainty on the value of the charm production cross section [187]. Track quality and $\nu_\mu$ CC selection cuts are effective in reducing this type of background for low neutrino energies, but the suppresion of high energy background requires further cuts, which are described below.

*Inclusive $\overline{\nu}_\mu$ background with fiducial and kinematic cuts*

Considering a set of $\overline{\nu}_\mu$ CC events generated randomly throughout the detector volume the inclusive background from this type of interaction has been studied. An additional cut on those events with a candidate failing the fiducial volume cut, defined in section 4.2.4, is used to suppress background caused by edge effects. As can be seen in figure 54-(left), the additional background introduced by edge effects is almost compensated by the fiducial cut, leading to an inclusive $\overline{\nu}_\mu$ background similar to the addition of the ones shown in Figs. 52-(right) and 53.

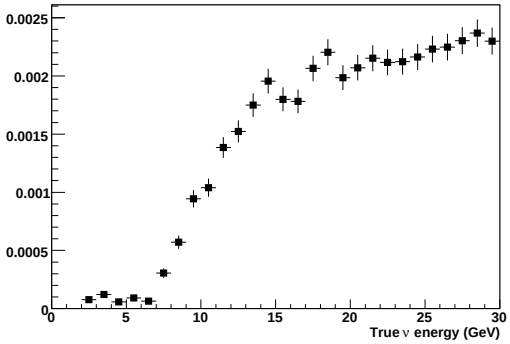


Figure 53: *Wrong sign muon decay background with track quality and $\nu_\mu$ CC selection cuts.*

The high energy background of figure 54-(left) is mainly due to very hard muons from the decay of charm mesons. Fortunately these muons, due to their decay origin, tend to be imbedded in the hadron shower unlike a true primary muon. Thus the $Q_t$ variable should be very effective in rejecting this kind of event. As can be seen in figure 54-(right) the kinematic cuts afford a sizeable suppression, particularly at higher neutrino energy.

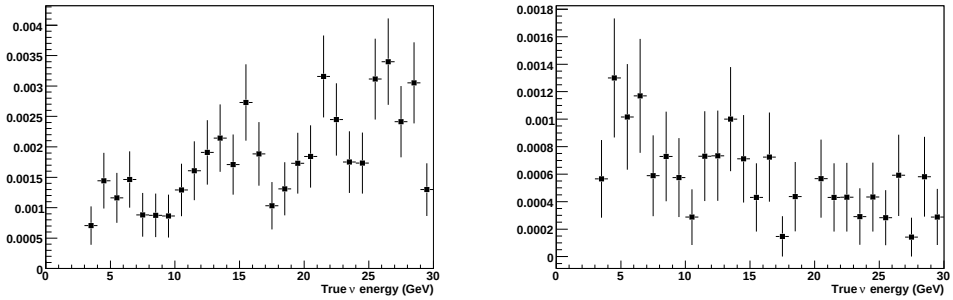


Figure 54: Expected background from $\overline{\nu}_\mu$ CC interactions when events are randomly generated in the entire detector: i) after track quality, $\nu_\mu$ CC selection and fiducial cuts, and ii) including kinematic cuts.

*Neutral current interactions*

Neutral current interactions should be of the same nature for all species. Background events will tend to originate from penetrating pions or muons from the decay of hadrons. Moreover, since there will always be missing energy in the event, those events successfully fitted will tend to be reconstructed at lower energy than the true neutrino energy. As such, and due to the large amount of NC events expected in the detector, this background must be suppressed efficiently. figure 55 shows the evolution of the NC background when different cuts are included.

*$\nu_e$ charge current interactions*

The interactions of $\nu_e$ present in the beam can also produce some background to the signal. While the electron itself will be stopped quickly and will shower far more than a muon, penetrating pions or decay muons originating in the hadronic shower can be mistaken for primary

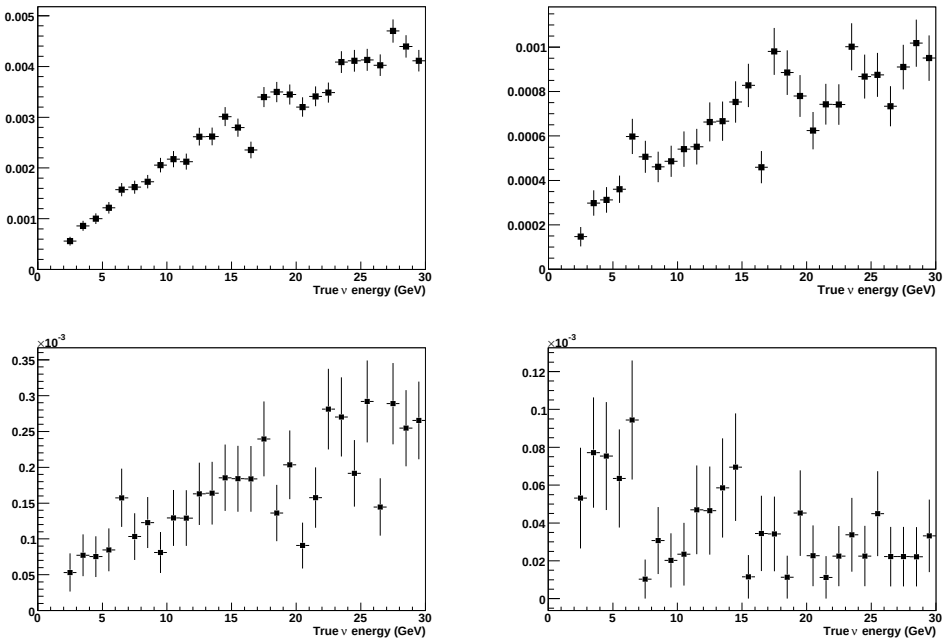


Figure 55: *Expected background from $\overline{\nu}_\mu$ NC interactions, i) with track quality cuts (equation 14) only, ii) including $\nu_\mu$ CC selection cuts, iii) substituting track quality cuts of equation 14 by those of equation 15 and iv) including kinematic cuts.*

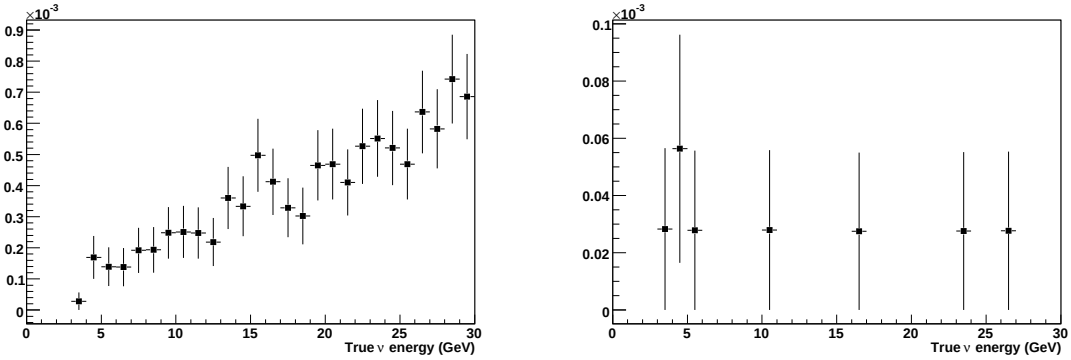


Figure 56: *$\nu_e$ CC background to golden channel signal, i) with track quality and $\nu_\mu$ CC selection cuts, and ii) including kinematic cuts.*

muons.

After application of track quality and $\nu_\mu$ CC selection cuts it can be seen in figure 56-(left) that the $\nu_e$ CC background can be reduced to a similar level as the NC background when the same cuts are applied. Moreover, excellent rejection of high energy neutrinos is obtained by applying kinematic cuts, as shown in figure 56-(right). This is because the candidate muon in $\nu_e$ events tends to have lower momentum than in NC events, as shown in figure 51 .

*Summary*

Considering all types of events mentioned above and applying the most successful analysis

| | Total | $0-5$ GeV | $5-10$ GeV | $10-30$ GeV |
|---|---|---|---|---|
| $\overline{\nu}_\mu$ CC | $5.5\times10^{-4}$ | $6.6\times10^{-4}$ | $8.2\times10^{-4}$ | $4.6\times10^{-4}$ |
| $\nu_e$ CC | $7.8\times10^{-6}$ | $2.6\times10^{-5}$ | $5.5\times10^{-6}$ | $5.5\times10^{-6}$ |
| $\overline{\nu}_\mu+\nu_e$ NC | $3.8\times10^{-5}$ | $6.8\times10^{-5}$ | $4.3\times10^{-5}$ | $3.1\times10^{-5}$ |
| $\nu_\mu$ (signal) | 0.64 | 0.25 | 0.66 | 0.69 |

Table 6: *Summary of expected fractional signal and background with true neutrino energy.*

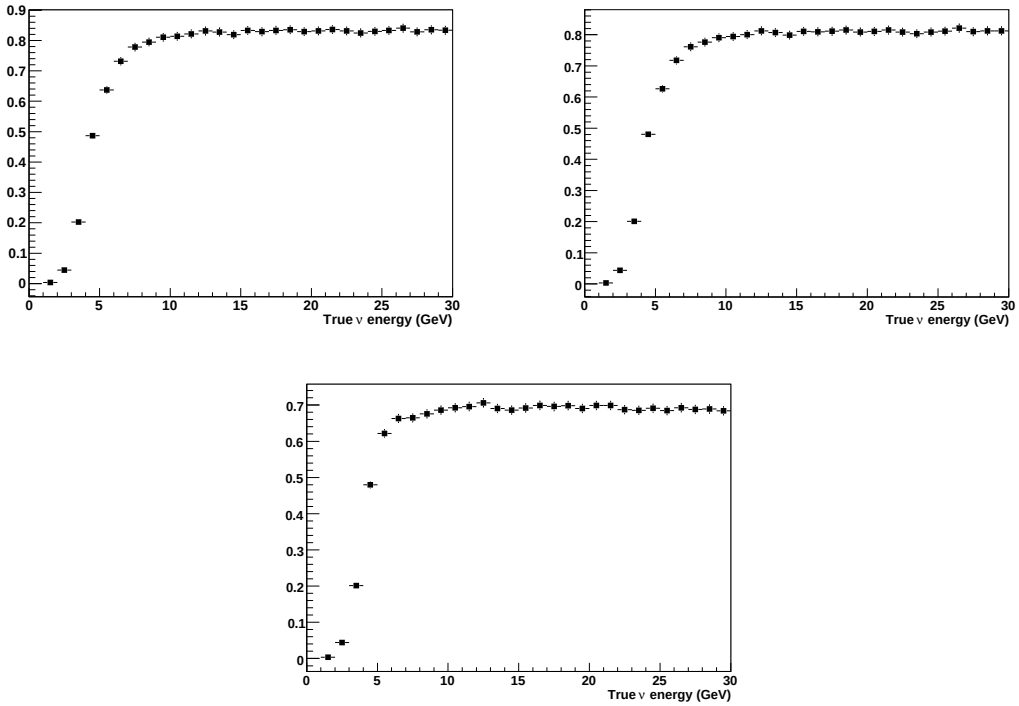


Figure 57: *Expected signal identification efficiency: i) after track quality and $\nu_\mu$ CC selection cuts, ii) including fiducial cuts, and iii) including kinematic cuts.*

chain described in table 5 the resulting signal efficiency and fractional backgrounds are those summarized in table 6. The evolution of the backgrounds for the different cuts is in Figs. 54, 55 and 56, while similar plots for the signal efficiency are those of figure 57. While it is obvious that the effect of the kinematic cuts below 7 GeV true neutrino energy is small due to their application only to events reconstructed with energy greater than this value, it is important to remark that fiducial cuts do not affect the efficiency at low energies either.

Another important question is that of the relation between the true and the reconstructed neutrino energy for the different interaction types. The response matrices are shown graphically in figure 58 and numerically in reference [174].

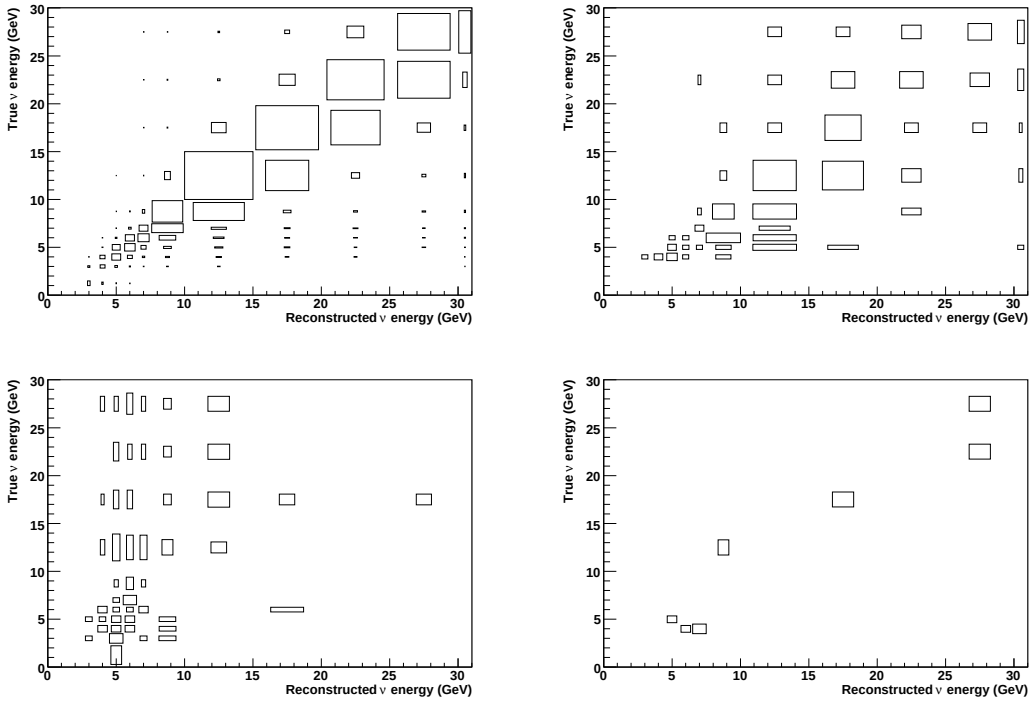


Figure 58: *Response matrix in true/reconstructed neutrino energy for signal and backgrounds: i) signal efficiency, ii) backgrounds from $\nu_\mu$ CC, iii) NC and iv) $\nu_e$ CC.*

### 4.2.6 Conclusions

Through a combination of fiducial, track quality, $\nu_\mu$ CC selection and kinematical cuts, an analysis has been applied demonstrating the power of MIND to detect and identify $\nu_\mu$ CC DIS interactions in the presence of realistic reconstruction of the primary muon. The efficiency threshold currently lies between 3 and 4 GeV, and an efficiency plateau of 70% is reached at about 6 GeV. While improved sensitivity could be achieved by lowering the threshold, as mentioned in section 4.2.2, this region would be dominated by quasi-elastic and resonance interactions which have not yet been considered. This type of interaction should contain less hadronic activity and thus the low energy pattern recognition efficiency should improve. An increased sample of successfully reconstructed events in this region should increase the efficiency of the golden channel analysis.

The powerful rejection afforded by the inclusion of the hadronic energy and direction vector highlights the importance of good hadronic reconstruction. While the hadronic energy has been reconstructed well in other similar experiments the direction vector requires careful consideration of both technology and analysis to achieve the required resolution. In a future publication we will include a re-optimisied MIND design, within a GEANT4 framework, where we will also take into account low energy quasi-elastic and resonance interactions.

Compared to the baseline MIND presented in [43], where perfect pattern recognition was assumed, these new results show some improvement. The aforementioned study considered the

charge and NC backgrounds and in both cases the results presented here are of similar level. The signal efficiency curve reaches a plateau at 70% in the bin of $6-7$ GeV. The corresponding curve in the previous study reaches approximately the same level at a similar or slightly higher energy depending on the particular analysis. Using this efficiency curve, Neutrino Factory sensitivity studies were carried out in the context of the International Scoping Study (ISS) for a future neutrino facility [188], demonstrating that a Neutrino Factory with two 50 ktonne MIND detectors at two different baselines has the largest $\theta_{13}-\delta_{CP}$ coverage out of all possible facilities. This study reinforces the conclusions from that study by showing that the pattern recognition and reconstruction of events in MIND do not degrade the selection efficiency for the oscillated signal.

### 4.3 Totally Active Scintillator Detector

A totally active scintillator detector (TASD) has been studied for a Low-Energy Neutrino Factory (LENF) and results from a first study of its expected performance were described in the recent ISStudy Detector Working Group report [43]. Using a TASD for neutrino physics is not new. Examples are KamLAND [189], which has been operating for several years, and the proposed NO$\nu$A detector [190], which is a $15-18$ Kton liquid scintillator detector that will operate off-axis to the NuMI beam line [191] at Fermilab. Note that, unlike KamLAND or NO$\nu$A, the TASD we are investigating for the low energy Neutrino Factory is magnetized and has a segmentation that is approximately 10 times that of NO$\nu$A. Magnetisation of such a large volume ($> 30,000$ m$^3$) is the main technical challenge in designing a TASD for a Neutrino Factory, although R&D to reduce the detector cost (driven in part by the large channel count, $7.5 \times 10^6$) is also needed.

The Neutrino Factory TASD we are considering consists of long plastic scintillator bars with a triangular cross-section arranged in planes which make x and y measurements (we plan to also consider an x-u-v readout scheme). Optimization of the cell cross section still needs further study since a true triangular cross section results in tracking anomalies at the corners of the triangle. The scintillator bars have a length of 15 m and the triangular cross-section has a base of 3 cm and a height of 1.5 cm. We have considered a design using liquid as in NO$\nu$A, but, compared to NO$\nu$A, the cell size is small (NO$\nu$A uses a $4 \times 6$ cm$^2$ cell) and the non-active component due to the PVC extrusions that hold the liquid becomes quite large (in NO$\nu$A, the scintillator is approximately 70% of the detector mass). Our design is an extrapolation of the MINER$\nu$A experiment [192] which in turn was an extrapolation of the D0 preshower detectors [193]. We are considering a detector mass of approximately 35 Kton (dimensions $15 \times 15 \times 150$ m). We believe that an air-core solenoid can produce the field required (0.5 Tesla) to do the physics.

As was mentioned above, magnetizing the large detector volume presents the main technical challenge for a Neutrino Factory TASD. Conventional room temperature magnets are ruled out due to their prohibitive power consumption, and conventional superconducting magnets are believed to be too expensive, due to the cost of the enormous cryostats needed in a conventional superconducting magnet design. In order to eliminate the cryostat, we have investigated a concept based on the superconducting transmission line (STL) that was developed for the Very

Large Hadron Collider superferric magnets [194]. The solenoid windings now consist of this superconducting cable which is confined in its own cryostat (figure 59). Each solenoid (10 required for the full detector) consists of 150 turns and requires 7500 m of cable. There is no large vacuum vessel and thus no large vacuum loads which make the cryostats for large conventional superconducting magnets very expensive.

The Neutrino Factory TASD response has been simulated with GEANT4 version 8.1 (figure 60). The GEANT4 model of the detector included each of the individual scintillator bars, but did not include edge effects on light collection, or the effects of a central wavelength shifting fiber. A uniform 0.5 Tesla magnetic field was simulated.

Samples of isolated muons in the range of momentum between 100 MeV/$c$ and 15 GeV/$c$ were simulated to allow the determination of the momentum resolution and charge identification capabilities. The NUANCE [195] event generator was also used to simulate 1 million $\nu_e$ and 1 million $\nu_\mu$ interactions. Events were generated in 50 mono-energetic neutrino energy bins between 100 MeV and 5 GeV. The results that follow only have one thousand events processed through the GEANT4 simulation and reconstruction.

The detector response was simulated assuming a light yield consistent with MINER$\nu$A measurements and current photo detector performance [190]. In addition, a 2 photo-electron energy resolution was added through Gaussian smearing to ensure that the energy resolution used in the following physics analysis would be a worst-case estimate. Since a complete pattern recognition algorithm was beyond the scope of our study, for our analysis the Monte Carlo information was used to aid in pattern recognition. All digitised hits from a given simulated particle where the reconstructed signal was above 0.5 photo electrons were collected. When using the isolated particles, hits in neighboring x and y planes were used to determine the 3 dimensional position of the particle. The position resolution was found to be approximately 4.5 mm RMS with a central Gaussian of width 2.5 mm [3]. These space points were then passed to the RecPack Kalman track fitting package [181].

For each collection of points, the track fit was performed with an assumed positive and negative charge. The momentum resolution and charge misidentification rates were determined by studying the fitted track in each case which had the better $\chi^2$ per degree of freedom. Figure 61 shows the momentum resolution as a function of muon momentum. The tracker achieves a resolution of better than 10% over the momentum range studied. Figure 62(a) shows the efficiency for reconstructing positive muons as a function of the initial muon momentum. The detector becomes fully efficient above 400 MeV.

The charge mis-identification rate was determined by counting the rate at which the track fit with the incorrect charge had a better $\chi^2$ per degree of freedom than that with the correct charge. Figure 62(b) shows the charge mis-identification rate as a function of the initial muon momentum.

[3] At this stage, the simulation does not take into account light collection inefficiencies in the corners of the base of the triangle.

The neutrino interactions were also reconstructed with the aid of the Monte Carlo information for pattern recognition. In an attempt to produce some of the effects of a real pattern recognition algorithm on the detector performance, only every fourth hit was collected for track fitting. Tracks were only fit if 10 such hits were found from a given particle. The Monte Carlo positions were smeared (Gaussian smearing using the 4.5 mm RMS determined previously) and passed to the Kalman track fit. The reconstruction returned:

- The total momentum vector of all fitted tracks;
- The momentum vector of the muon (muon ID from MC truth);
- The reconstructed and truth energy sum of all the hits that were not in a particle that was fitted; and
- The reconstructed energy sum of all hits in the event.

The $\nu_\mu$ CC event reconstruction efficiency as a function of neutrino energy is shown in figure 63(a). The fraction of $\nu_\mu$ CC events with a reconstructed muon is shown in figure 63(b). In this figure the bands represent the limits of the statistical errors for this analysis.

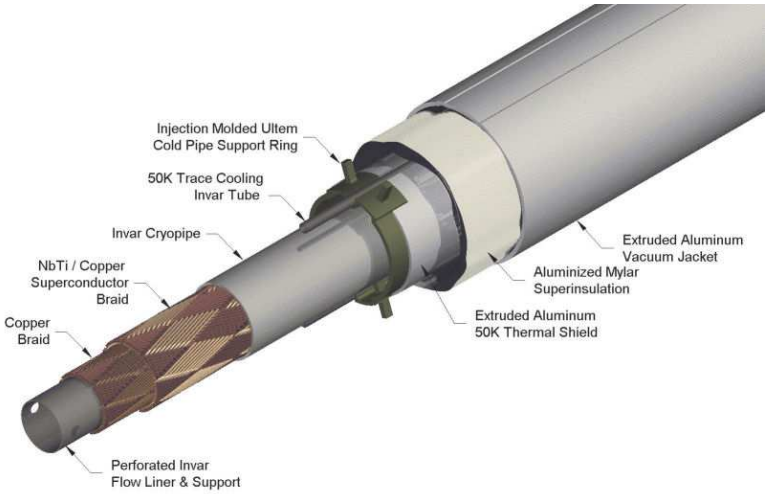


Figure 59: *Diagram of Superconducting Transmission Line design.*

Based on these initial Neutrino Factory TASD studies, in our phenomenological analysis we assume the detector has an effective threshold for measuring muon neutrino CC events at $E_\nu =$ 500 MeV, above which it has an energy independent efficiency of 73%. The 73% efficiency is primarily driven by the neutrino interaction kinematics, not by the detector tracking efficiency. No charge-ID criterion is applied here. The charge misidentification rate information is used as input into the effect of backgrounds on the analysis.

We note that, to fully understand the backgrounds in the TASD requires a simulation that includes neutrino interactions and a full event reconstruction. Although this is beyond the

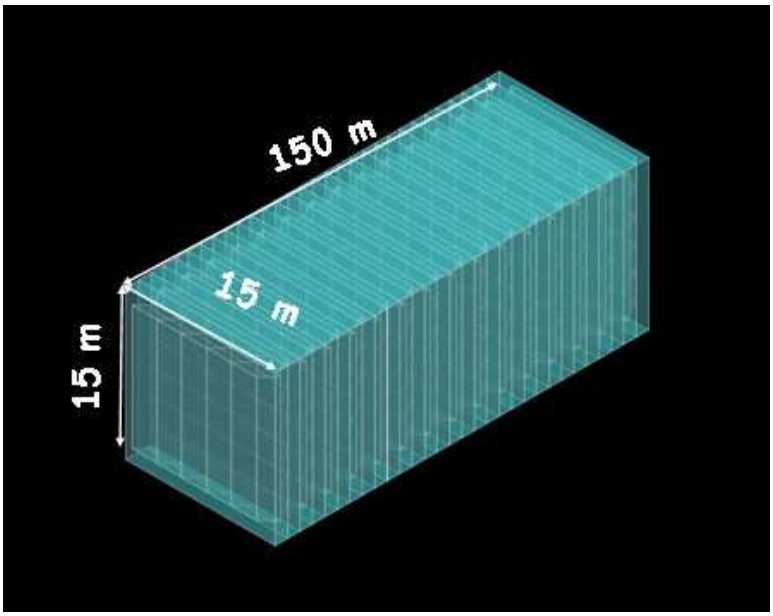


Figure 60: 04-DetWG/Figures/*Schematic of Totally Active Scintillator Detector.*

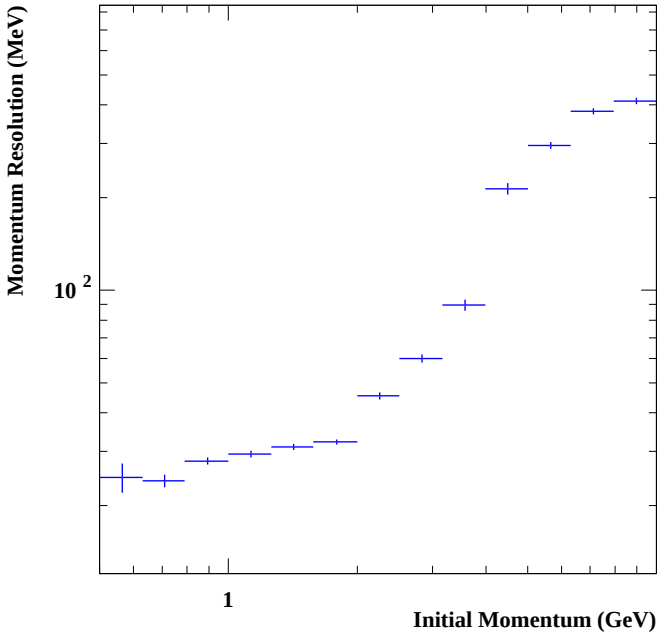


Figure 61: 04-DetWG/Figures/*Momentum resolution as a function of the muon momentum.*

scope of the present study, a consideration of backgrounds in the well studied Magnetized Fe-Scintillator detector proposed for the high-energy Neutrino Factory [68] and The International Scoping Study for a Neutrino Factory [43] motivates the $10^{-3}$ background (contamination)

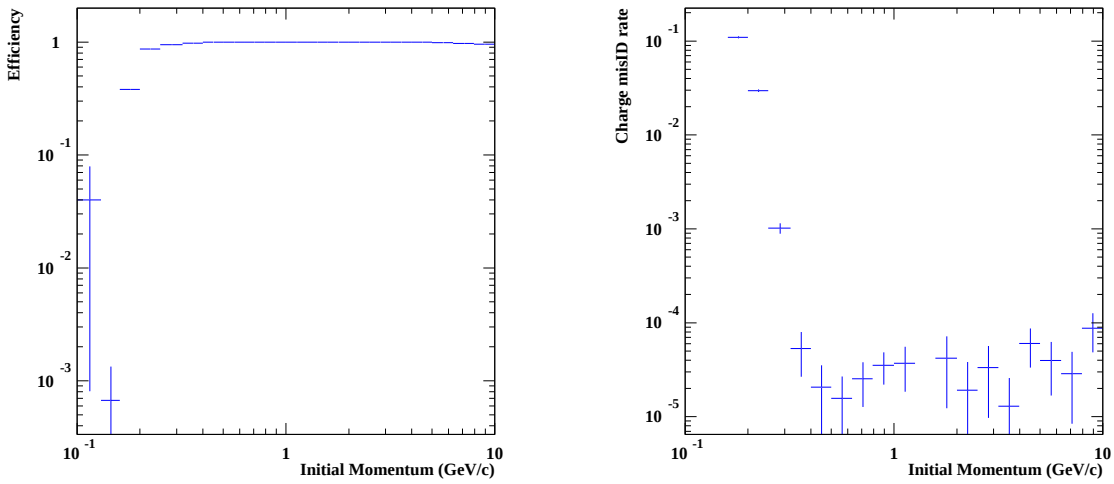


(a) (b)

Figure 62: *(a) Efficiency for reconstructing positive muons. (b) Muon charge mis-identification rate as a function of the initial muon momentum.*

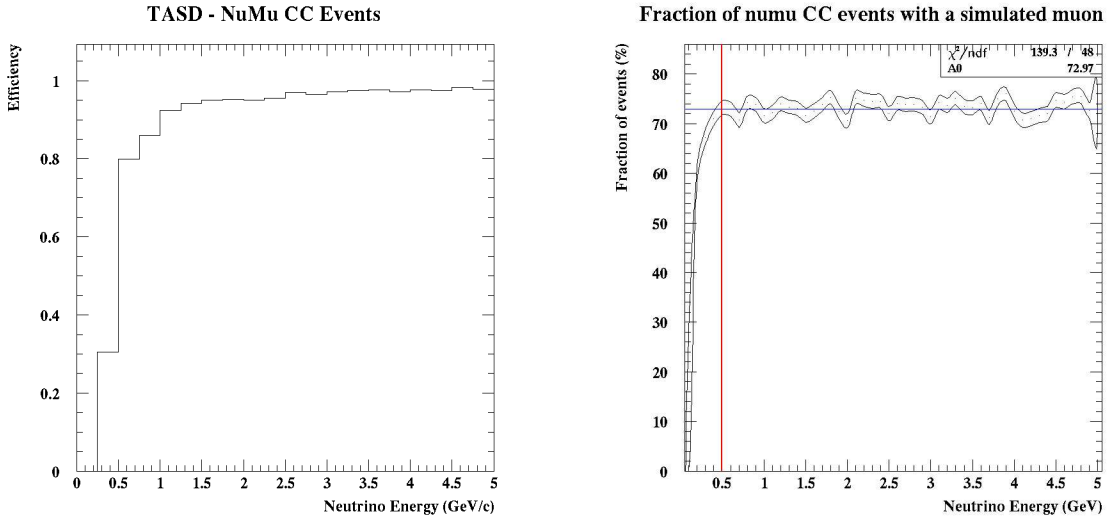


(a) (b)

Figure 63: *(a) Reconstruction efficiency of NuMu CC events as a function of neutrino interaction energy. (b) Fraction of NuMu CC events with a reconstructed muon.*

assumption used for the TASD. Before kinematic cuts, the main backgrounds for the MIND are muon charge mis-ID, charm decay, pion and kaon decay, and are all of comparable order: $1 - 5 \times 10^{-4}$. For the TASD at a low energy Neutrino Factory the muon charge mis-ID rate (figure 62(b)) and the charm decay background is suppressed (at the level $4 - 8 \times 10^{-5}$) due to the low energy beam. Pion and Kaon decay in flight become the main background concerns at

the $1 - 5 \times 10^{-4}$ level. A figure of merit for comparing the TASD to a conventional MIND is the ratio of their respective particle decay lengths to interaction lengths. For TASD the ratio is about 1; for the MIND it is approximately 8. So, naively we can conclude that the decay background in TASD will be 10 times worse than in the conventional detector ignoring any kinematic or topological cuts. However, the TASD will have vastly superior kink detection to identify decay-in-flight. For example we will typically have 40 hits on the pion track before decay. In addition TASD will have continuous $dE/dx$ measurements along the track and better overall energy resolution. We believe that these properties will allow us to control backgrounds to the $10^{-3}$ level or better.

## 4.4 Liquid Argon Detector

### 4.4.1 Introduction

In order to design and fully cost a liquid argon (LAr) TPC on the scale of 100 kton for use at a Neutrino Factory there are a number of issues that need addressed, including:

- Large underground LAr-vessel engineering;
- Site identification and main cavern design: excavation, underground construction, safety, etc.;
- LAr purity in a large non-evacuable volume: cryogenic pumps;
- Passive insulation of the vessel: thermal uniformity, stability, etc.;
- High voltage implementation for drift fields;
- Ionisation signal distortion/attenuation over very long drift distances;
- Low cost readout and electronics; and
- Magnetisation of the volume.

The status of LAr R&D in Europe, Japan, and the US to address these issues are summarised below.

### 4.4.2 Europe and Japan

Suitable underground sites around Europe and issues related to underground tank design and assembly are being studied as part of the EC FP7 LAGUNA initiative [196] which is due to produce a final report in July 2010.

Detector R&D has focused on the intermediate steps necessary to realise the final goal of a 100 kton-scale detector, capable of precise long-baseline oscillation physics while at the same

time being a discovery device for proton decay and astrophysical neutrino studies. The plan for these studies involves the phased build of prototypes of increasing size culminating in the construction of a 1 kton device from around 2012 onwards. This would be large enough to make realistic performance extrapolations to the 100 kton-scale whilst being small enough to minimise construction costs and timescales. An overview of the 'Roadmap', is presented in figure 64 and shows prototypes, some of which have already been built and studied, and others which are currently being prepared.

Moving on from the single phase wire-plane readout of the ICARUS project [197], there are two main approaches to readout in LAr currently under study that can potentially achieve the necessary signal/noise performance: (i) collecting ionisation charge in the gas phase above the LAr volume utilising Thick Electron Multiplier's (THGEM) to achieve charge gain – led by the ETHZ and KEK groups; and (ii) imaging electroluminescence light produced in the holes of a THGEM plane all in the liquid phase – studied by the UK groups.

Results from the first method, based on a 3 lt prototype and reported in [198,199], have proven the principle of extracting ionisation charge released in the LAr volume into the gas phase by a series of grids and driven into the holes of a double THGEM plane where charge amplification occurs. Cosmic ray tracks have been recorded by segmenting the upper electrode of the THGEM and the anode plane in orthogonal directions for $x - y$ readout. Similar results from a 10 lt prototype LAr vessel have been reported from a group at KEK (see [200]) who are working in close collaboration with the ETHZ group. The KEK group are currently preparing a 250 lt experiment, based on a cryostat borrowed from the MEG collaboration, which will move into the LNS (Tohoku University) electron beam in the summer of 2010 to test response to electrons in the energy range $100\,\mathrm{Mev} < \mathrm{E} < 850\,\mathrm{Mev}$. Longer term, there are plans to move this vessel into the JPARC neutrino beam (see [200]). The characterisation of LAr TPC performance in test-beams is also on the roadmap for Europe where a 3.9 ton/2.8 $\mathrm{m}^3$ instrumented volume (ePiLAr) is being proposed for exposure in the CERN SPS North Area [201] with the objective of testing the calibration, calorimetric response and particle identification capability for $e, \mu, \pi$ in the momentum range $0.5\,\mathrm{GeV/c} < \mathrm{p} < 5\,\mathrm{GeV/c}$. This project will also act as a testbed for solutions to LAr purification on large scales and to the realisation of cost effective readout electronics, perhaps functioning in the LAr volume itself [202].

Development of the second method based on electro-luminescence light readout, is at a more preliminary stage but some proof-of-concept studies have been completed. The idea is to take an image of a THGEM plane, the holes of which radiate light stimulated by the arrival of released ionisation charge in the LAr volume. Silicon photomultipliers as potential imaging devices have been shown to function in a LAr environment [203] and the first detection of such electroluminescence light from a THGEM hole has been reported [204].

Progress in general has benefitted from the development, in parallel, of the ArDM (RE18) dark matter project which is a ton-scale LAr device with a 1 $\mathrm{m}^2$ THGEM readout. This activity has pioneered use of wavelength shifting technology for light collection [205], the use of cyrogenic pumps for purity filtering and the delivery of high voltage drift fields in LAr via immersed Cockcroft-Walton voltage multipliers. The experiment was first filled with LAr in May'09 for

light readout and is due to be filled again in January'10 for tests of charge readout in double phase mode (without amplification).

In order to confirm the feasibility of extracting ionisation charge signals over many metres of drift in LAr, there two experiments which will begin in 2010: ArgonTube at the University of BERN and LANNDD-5M at CERN, both of which will drift over 5 m. There are also plans in KEK for such a project where the proposed drfit distance will be 10 m.

On the question of magnetising a large volume of LAr for charge separation, the current status remains a proof-of-principle study on a 10 lt prototype [206] and a scalable design concept for a multi-kton module based on a superconducting solenoid immersed in the LAr volume [207].

A further relevant area of activity in both Europe and the USA is the development of: i) detailed simulations of charge and light transport in LAr; and ii) software techniques to reconstruct neutrino interactions in an automated way. Advancing the simulation of LAr is work ongoing in both Europe and the US and is crucial to understand the prototype results and to extrapolate with confidence these results to larger scales. With the collection of larger data volumes in LAr, automated reconstruction has become a more pressing issue and will asist greatly the process of comparing performance of this technology with other detector options for the Neutrino Factory. Activity in the area is still very preliminary but a recent status report was given in [208].

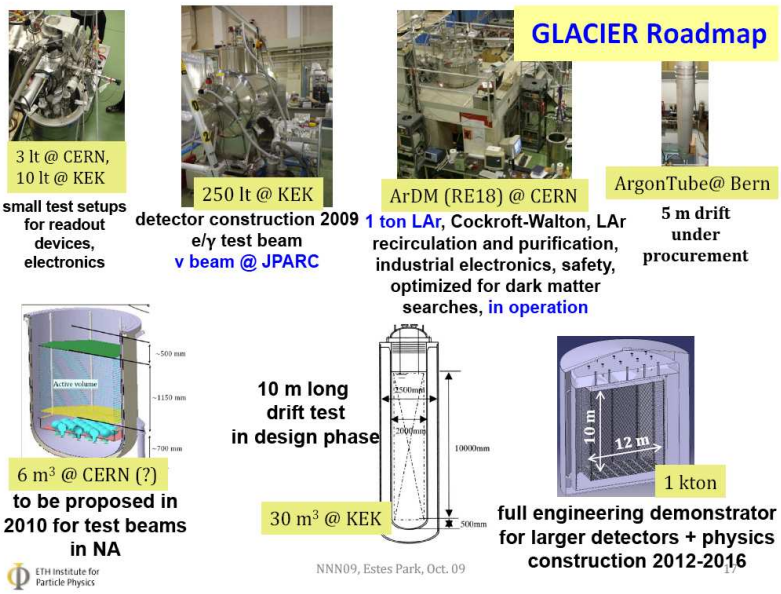


Figure 64: Roadmap for LAr detector development in Europe/Japan. From [209]

### 4.4.3 North America

A lot of progress has been made in the US over the past year. This can be seen in figure 65 which shows this progress within the context of a roadmap for LArTPC development in the US.

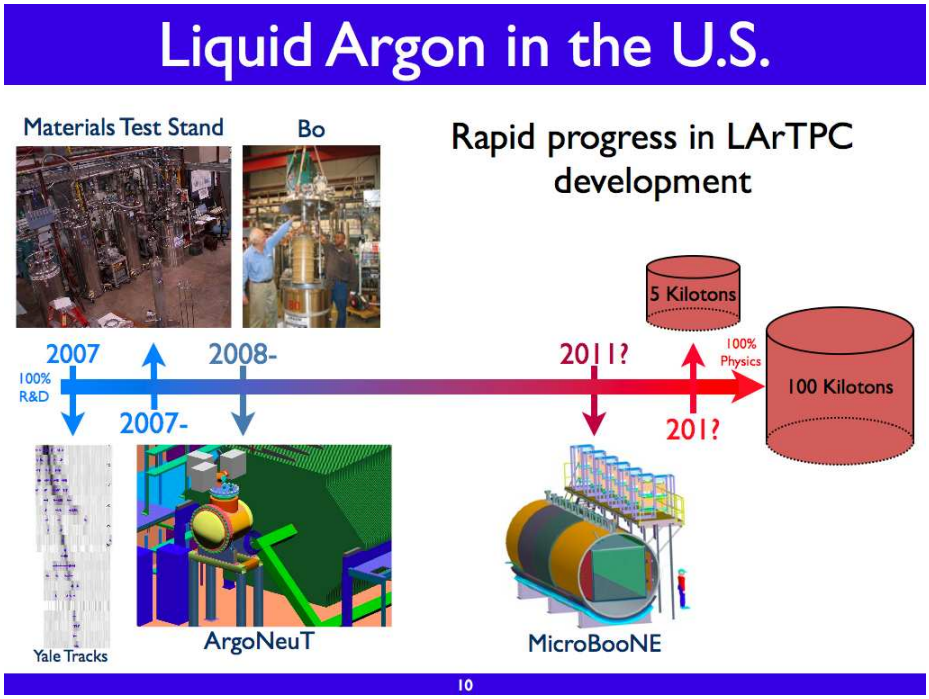


Figure 65: Roadmap for LArTPC detector development in the US

Much of the "preliminary" activities in the roadmap have now been completed. This includes a number of teststands at Fermilab to perform materials tests [210] and to develop argon purification techniques [211]. The ArgoNeuT [212] LArTPC is a 0.3 ton device that was placed in the NuMI neutrino beam in the same hall where the MINOS near detector is located. ArgoNeuT took data in the fall of 2009. The first recorded neutrino event – a candidate $\nu_\mu$ DIS event – is shown in figure 66.

The next stage is the MicroBooNE experiment [213] which is 100 ton LArTPC located along the Booster neutrino line at Fermilab. The experiment received so-called "CD0" approval from the DOE in October of last year. This will not only provide information to improve future designs but also the costing exercise will allow for much better cost estimates for the ultimate detector. Also getting "CD0" approval from the DOE was the LBNE [214] (Long Baseline Neutrino Experiment) which involves directing a new neutrino beam from Fermilab to a detector located in the DUSEL laboratory 1300 km away. A LArTPC is one of the proposed technologies for the far detector.

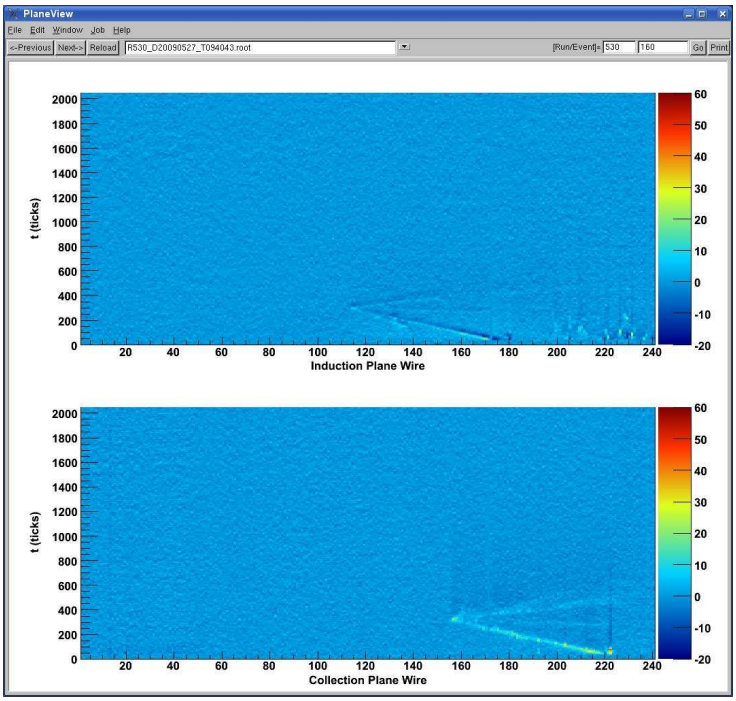


Figure 66: ArgoNeuT: First recorded neutrino event in a LArTPC in the US.

## 4.5 Near detector

The main aim of the Near Detector of the Neutrino Factory is to help minimize the systematic errors associated with the oscillation measurements at the far detector. This includes precisely measuring the absolute neutrino flux as well as the relevant neutrino cross sections needed to estimate the background to oscillation measurements at the far detector.

The importance of a Near Detector to the physics program of the Neutrino Factory was emphasised most recently by the work of Tang and Winter [215]. In figure 8, the allowed $\sin^2\theta_{13}$- $\delta_{CP}$ region for a Neutrino Factory with one and two far detectors is illustrated. As can be seen, the impact of near detectors is very large for both the one and two detector scenarios.

A secondary goal of the Near Detector is to take advantage of the large flux of neutrinos for a dedicated study of neutrino-nucleus interactions looking for new physics and non-standard interactions. It has been pointed out [215] that near detectors could be very relevant for the extraction of neutrino source non-standard interactions since these would exhibit an unambiguous *zero-distance* effect. Because there are no tau neutrinos in the beam, Tang and Winter suggest that the most interesting option may be to use near detectors to measure $\nu_{tau}$ appearence.

### 4.5.1 Beam simulation and flux measurement at the near detector

Full simulation of the neutrino beam for all neutrino flavours and including polarization states of the muon are now available [216, 217]. The energy distribution of the resulting neutrino events

for both $\nu_\mu$ and $\nu_e$ and for both polarization states of the parent muon is shown in figure 67. The vertical dotted lines are explained in the next section.

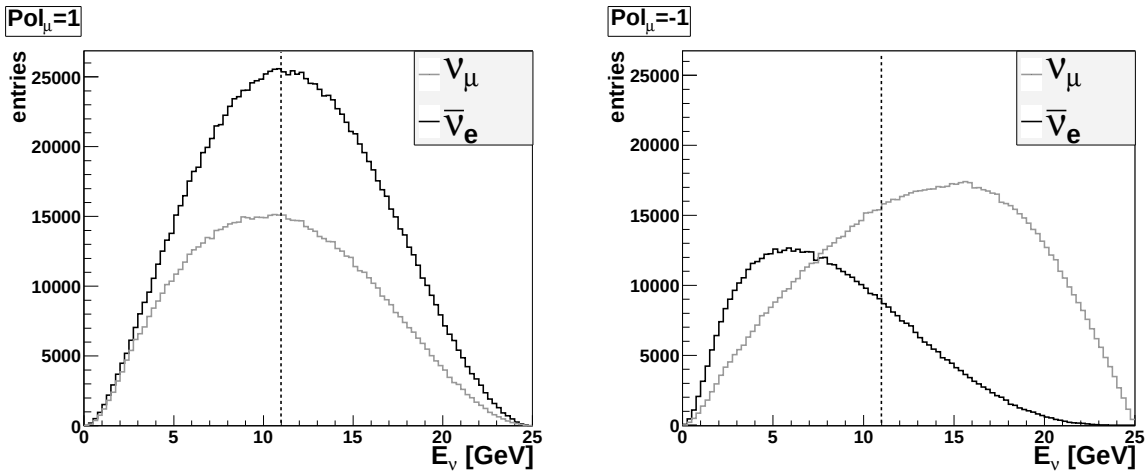


Figure 67: Distributions of the neutrino energy over a near detector of radius 1.5 m for the two polarizations of the decaying muons. Dotted lines indicate the threshold for the leptonic processes used to determine the neutrino flux.

The quasi-elastic scattering off electrons can be used to measure the flux, because its absolute cross-section can be calculated theoretically with enough confidence. The two processes of interest for neutrinos from $\mu^-$ decays are:

$$\nu_\mu + e^- \rightarrow \nu_e + \mu^-; \tag{20}$$

and

$$\bar{\nu}_e + e^- \rightarrow \bar{\nu}_\mu + \mu^-. \tag{21}$$

Both processes have a threshold at $\sim 11\ GeV$. The energy spectra of the beam neutrinos hitting the near detector are shown in figure 67, where the threshold for the two processes of interest is shown with doted line.

If we want to measure the neutrino flux by using the quasi-elastic scattering off electrons (for earlier measurements of these processes see [218, 219]), the near detector has to be able to distinguish between the leptonic events (processes (20) and (21)) and inclusive charged-current (CC) neutrino interactions with nucleus $\nu_\mu + N \rightarrow \mu^- + X$, which are a few orders of magnitude more intensive. This implies that the near detector must be able to measure the angle between the beam axis and the direction of the outgoing muon $\theta_\mu$, the momentum of the outgoing muon, thus the energy $E_\mu$, the transverse momentum $p_\perp$, and the total recoil (hadronic) energy $E_{had}$.

Different variables for suppression of the background from inclusive $\nu N$ CC reactions have been examined:

- muon scattering angle $\theta_\mu$;

- transverse momentum $p_\perp$;
- $E_\mu * \theta_\mu^2$; and
- recoil (hadronic) energy $E_{had}$.

Spectra of the events over smeared $\theta_\mu$ and $E_\mu * \theta_\mu^2$ for several resolution scenarios and for cuts on the recoil energy depicted have been performed. Examples are shown in figures 68 and 69. or a decisive choice more detailed simulation of the background with $\theta_\mu \to 0$ is needed, since it was shown earlier [220] that $\theta_\mu$ is more efficient than $p_\perp$ for signal extraction.

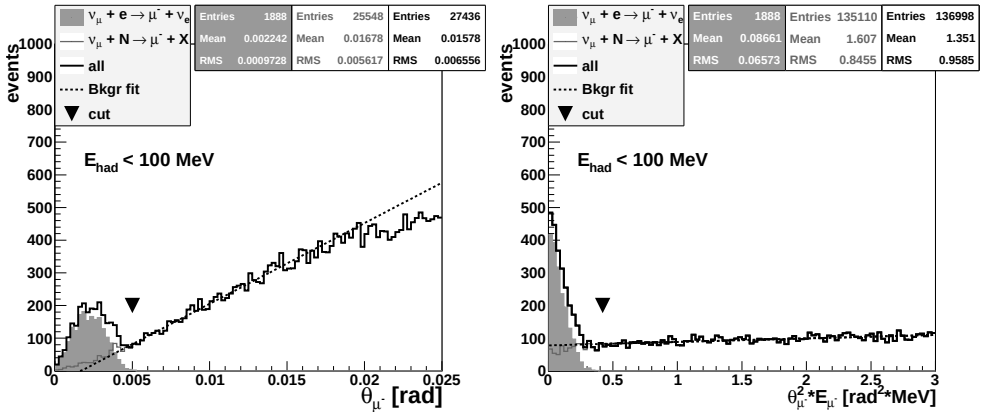


Figure 68: "Measured" distributions over the polar angle $\theta_\mu$ (left) and the variable $\theta_\mu^2 E$ (right) of the outgoing muons smeared with the following resolutions: $\sigma(\theta) = 0.1\ mrad$; $\frac{\sigma(E_\mu)}{E_\mu} = 1\%$; $\frac{\sigma(E_{had})}{E_{had}} = 1\%$. The leptonic events (1888 altogether) are filled with gray, the hadronic events (601 on the left panel and 838 on the right one) are plotted in gray and the total spectrum (2476 events on the left and 2725 events on the right) is in black. The cut value is denoted by black inverted triangle. Doted lines indicate the background extrapolation which gives, below the cut value, 455±53 events on the left and 1127±26 events on the right.

### 4.5.2 Plans for 2010

Our plans for the year 2010 include:

- Specification of detector design and size;
- Full GEANT4 simulation to obtain "true" values of the measurables;
- Implementation of some reconstruction and obtaining of "measured" values; and
- Definition of a procedure for flux determination based on statistical subtraction of the inclusive background and estimation of expected uncertainties.

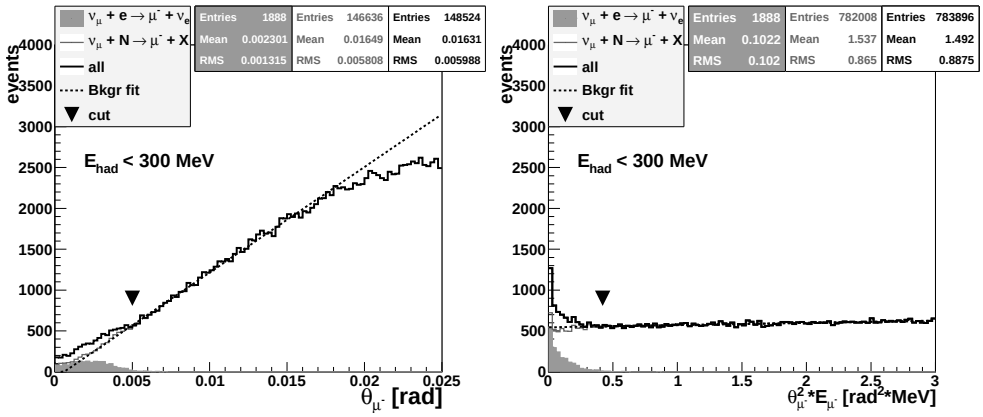


Figure 69: "Measured" distributions over the polar angle $\theta_\mu$ (left) and the variable $\theta^2_\mu E$ (right) of the outgoing muons smeared with the following resolutions: $\sigma(\theta) = 1.0\ mrad$; $\frac{\sigma(E_\mu)}{E_\mu} = 10\%$; $\frac{\sigma(E_{had})}{E_{had}} = 10\%$. The leptonic events (1888 altogether) are filled with gray, the hadronic events (642 on the left panel and 893 on the right one) are plotted in gray and the total spectrum (2424 events on the left and 2726 events on the right) is in black. The cut value is denoted by black inverted triangle. Doted lines indicate the background extrapolation which gives, below the cut value, 587±64 events on the left and 1196±26 events on the right.

# Acknowledgements

Resources for the International Design Study for the Neutrino Factory collaborations activities is provided by funding agencies from around the work, the support is gratefully acknowledged. Over the course of the study to date, plenary meetings have been held at the STFC Rutherford Appleton Laboratory, CERN, the DOE Fermi National Accelerator Laboratory, and at the Tata Institute for Fundamental Research, Mumbai. We gratefully acknowledge the warm welcome and hospitality we have received at each of these laboratories.

# References


[1] T. Schwetz, M. A. Tortola, and J. W. F. Valle, "Three-flavour neutrino oscillation update," *New J. Phys.* **10** (2008) 113011, 0808.2016.

[2] **Particle Data Group** Collaboration, C. Amsler *et al.*, "Review of particle physics," *Phys. Lett.* **B667** (2008) 1.

[3] S. Geer, "Neutrino beams from muon storage rings: Characteristics and physics potential," *Phys. Rev.* **D57** (1998) 6989–6997, hep-ph/9712290.

[4] **ISS Physics Working Group** Collaboration, A. Bandyopadhyay *et al.*, "Physics at a future Neutrino Factory and super-beam facility," *Rept. Prog. Phys.* **72** (2009) 106201, 0710.4947.

[5] **IDS-NF** Collaboration, "The International Design Study for the Neutrino Factory." https://www.ids-nf.org/wiki/FrontPage.

[6] **The Strategy Session of CERN Council** Collaboration, "The European strategy for particle physics." http://council-strategygroup.web.cern.ch/council-strategygroup/Strategy_Statement.pdf.

[7] **The International Design Study for the Neutrino Factory** Collaboration, T. I.-N. S. Group, "Principal objectives." https://www.ids-nf.org/wiki/FrontPage/Documentation?action=AttachFile&do=get&target=IDS-NF-001-v1.0.pdf.

[8] **The International Design Study for the Neutrino Factory** Collaboration, T. I.-N. S. Group, "The fourth IDS-NF plenary meeting, TIFR, Mumbai, 12-14 October 2009: discussion document." https://www.ids-nf.org/wiki/FrontPage/Documentation?action=AttachFile&do=get&target=IDS-NF-016-v1.0.pdf.

[9] **The International Design Study for the Neutrino Factory** Collaboration, T. I.-N. Physics and P. E. Group, "Flavour physics in the era of precision neutrino experiments," 2009. http://www.ippp.dur.ac.uk/Workshops/09/Coseners/.

[10] M. C. Gonzalez-Garcia, M. Maltoni, and J. Salvado, "Updated global fit to three neutrino mixing: status of the hints of theta13 ¿ 0," 1001.4524.

[11] G. L. Fogli *et al.*, "Observables sensitive to absolute neutrino masses (Addendum)," *Phys. Rev.* **D78** (2008) 033010, 0805.2517.

[12] G. L. Fogli, E. Lisi, A. Marrone, A. Palazzo, and A. M. Rotunno, "SNO, KamLAND and neutrino oscillations: theta(13)," 0905.3549.

[13] **KamLAND** Collaboration, S. Abe *et al.*, "Precision Measurement of Neutrino Oscillation Parameters with KamLAND," *Phys. Rev. Lett.* **100** (2008) 221803, 0801.4589.

[14] **SNO** Collaboration, B. Aharmim *et al.*, "An Independent Measurement of the Total Active 8B Solar Neutrino Flux Using an Array of 3He Proportional Counters at the Sudbury Neutrino Observatory," *Phys. Rev. Lett.* **101** (2008) 111301, 0806.0989.

[15] **SNO** Collaboration, B. Aharmim *et al.*, "Low Energy Threshold Analysis of the Phase I and Phase II Data Sets of the Sudbury Neutrino Observatory," 0910.2984.

[16] B. T. Cleveland *et al.*, "Measurement of the solar electron neutrino flux with the Homestake chlorine detector," *Astrophys. J.* **496** (1998) 505–526.

[17] **GNO** Collaboration, M. Altmann *et al.*, "Complete results for five years of GNO solar neutrino observations," *Phys. Lett.* **B616** (2005) 174–190, hep-ex/0504037.

[18] **Super-Kamkiokande** Collaboration, J. Hosaka *et al.*, "Solar neutrino measurements in Super-Kamiokande-I," *Phys. Rev.* **D73** (2006) 112001, hep-ex/0508053.

[19] **SAGE** Collaboration, J. N. Abdurashitov *et al.*, "Measurement of the solar neutrino capture rate with gallium metal. III: Results for the 2002–2007 data-taking period," *Phys. Rev.* **C80** (2009) 015807, 0901.2200.

[20] F. Kaether, W. Hampel, G. Heusser, J. Kiko, and T. Kirsten, "Reanalysis of the GALLEX solar neutrino flux and source experiments," *Phys. Lett.* **B685** (2010) 47–54, 1001.2731.

[21] **The Borexino** Collaboration, C. Arpesella *et al.*, "Direct Measurement of the Be-7 Solar Neutrino Flux with 192 Days of Borexino Data," *Phys. Rev. Lett.* **101** (2008) 091302, 0805.3843.

[22] A. Serenelli, S. Basu, J. W. Ferguson, and M. Asplund, "New Solar Composition: The Problem With Solar Models Revisited," 0909.2668.

[23] **MINOS** Collaboration, P. Adamson *et al.*, "Measurement of Neutrino Oscillations with the MINOS Detectors in the NuMI Beam," *Phys. Rev. Lett.* **101** (2008) 131802, 0806.2237.

[24] **K2K** Collaboration, E. Aliu *et al.*, "Evidence for muon neutrino oscillation in an accelerator- based experiment," *Phys. Rev. Lett.* **94** (2005) 081802, hep-ex/0411038.

[25] **Super-Kamiokande** Collaboration, Y. Ashie *et al.*, "A measurement of atmospheric neutrino oscillation parameters by Super-Kamiokande I," *Phys. Rev.* **D71** (2005) 112005, hep-ex/0501064.

[26] M. Maltoni, T. Schwetz, M. A. Tortola, and J. W. F. Valle, "Status of global fits to neutrino oscillations," *New J. Phys.* **6** (2004) 122, hep-ph/0405172. updated results in hep-ph/0405172 (v6).

[27] G. L. Fogli, E. Lisi, A. Marrone, and A. Palazzo, "Global analysis of three-flavor neutrino masses and mixings," *Prog. Part. Nucl. Phys.* **57** (2006) 742–795, hep-ph/0506083.

[28] M. C. Gonzalez-Garcia and M. Maltoni, "Phenomenology with Massive Neutrinos," *Phys. Rept.* **460** (2008) 1–129, 0704.1800.

[29] T. Schetz *Phys. Scripta, T* **127** (2006).

[30] **Kamiokande** Collaboration, S.-. R. Wendell *et al.*, "Atmospheric neutrino oscillation analysis with sub-leading effects in Super-Kamiokande I, II, and III," 1002.3471.

[31] M. Apollonio *et al.*, "Search for neutrino oscillations on a long base-line at the CHOOZ nuclear power station," *Eur. Phys. J.* **C27** (2003) 331–374, hep-ex/0301017.

[32] G. L. Fogli, E. Lisi, A. Marrone, A. Palazzo, and A. M. Rotunno, "Hints of $theta_{13} > 0$ from global neutrino data analysis," *Phys. Rev. Lett.* **101** (2008) 141801, 0806.2649.

[33] M. Maltoni and T. Schwetz, "Three-flavour neutrino oscillation update and comments on possible hints for a non-zero $theta_{13}$," *PoS* **IDM2008** (2008) 072, 0812.3161.

[34] **MINOS** Collaboration, P. Adamson *et al.*, "Search for muon-neutrino to electron-neutrino transitions in MINOS," *Phys. Rev. Lett.* **103** (2009) 261802, 0909.4996.

[35] S. Goswami and A. Y. Smirnov, "Solar neutrinos and 1-3 leptonic mixing," *Phys. Rev.* **D72** (2005) 053011, hep-ph/0411359.

[36] A. B. Balantekin and D. Yilmaz, "Contrasting solar and reactor neutrinos with a non-zero value of theta13," *J. Phys.* **G35** (2008) 075007, 0804.3345.

[37] M. Maltoni, T. Schwetz, M. A. Tortola, and J. W. F. Valle, "Status of three-neutrino oscillations after the SNO-salt data," *Phys. Rev.* **D68** (2003) 113010, hep-ph/0309130.

[38] **The International Design Study for the Neutrino Factory** Collaboration, T. I.-N. S. Group, "Neutrino Factory: specification of baseline." https://www.ids-nf.org/wiki/FrontPage/Documentation?action=AttachFile&do=get&target=IDS-NF-002-v1.1.pdf.

[39] C. Crisan and S. Geer, "How well do we need to know the beam properties at a neutrino factory?,". FERMILAB-TM-2101.

[40] A. Broncano and O. Mena, "Corrections to the fluxes of a neutrino factory," *Eur. Phys. J.* **C29** (2003) 197–206, hep-ph/0203052.

[41] D. Indumathi and N. Sinha, "Effect of tau neutrino contribution to muon signals at neutrino factories," *Phys. Rev.* **D80** (2009) 113012, 0910.2020.

[42] J. Tang and W. Winter, "Physics with near detectors at a neutrino factory," *Phys. Rev.* **D80** (2009) 053001, 0903.3039.

[43] **ISS Detector Working Group** Collaboration, T. Abe *et al.*, "Detectors and flux instrumentation for future neutrino facilities," *JINST* **4** (2009) T05001, 0712.4129.

[44] S. Antusch, M. Blennow, E. Fernandez-Martinez, and J. Lopez-Pavon, "Probing non-unitary mixing and CP-violation at a Neutrino Factory," *Phys. Rev.* **D80** (2009) 033002, 0903.3986.

[45] J. Kopp, M. Lindner, T. Ota, and J. Sato, "Non-standard neutrino interactions in reactor and superbeam experiments," *Phys. Rev.* **D77** (2008) 013007, 0708.0152.

[46] M. B. Gavela, D. Hernandez, T. Ota, and W. Winter, "Large gauge invariant non-standard neutrino interactions," *Phys. Rev.* **D79** (2009) 013007, 0809.3451.

[47] T. Ohlsson, T. Schwetz, and H. Zhang, "Non-standard neutrino interactions in the Zee-Babu model," *Phys. Lett.* **B681** (2009) 269–275, 0909.0455.

[48] M. Malinsky, T. Ohlsson, and H. Zhang, "Non-Standard Neutrino Interactions from a Triplet Seesaw Model," *Phys. Rev.* **D79** (2009) 011301, 0811.3346.

[49] C. Giunti, M. Laveder, and W. Winter, "Short-Baseline Electron Neutrino Disappearance at a Neutrino Factory," *Phys. Rev.* **D80** (2009) 073005, 0907.5487.

[50] "Madrid Neutrino NSI Workshop." http://www.ft.uam.es/workshops/neutrino/.

[51] D. Meloni, T. Ohlsson, W. Winter, and H. Zhang, "Non-standard interactions versus non-unitary lepton flavor mixing at a neutrino factory," 0912.2735.

[52] E. Fernandez-Martinez, M. B. Gavela, J. Lopez-Pavon, and O. Yasuda, "CP-violation from non-unitary leptonic mixing," *Phys. Lett.* **B649** (2007) 427–435, hep-ph/0703098.

[53] S. Antusch, J. P. Baumann, and E. Fernandez-Martinez, "Non-Standard Neutrino Interactions with Matter from Physics Beyond the Standard Model," *Nucl. Phys.* **B810** (2009) 369–388, 0807.1003.

[54] **The International Design Study for the Neutrino Factory** Collaboration, A. Donini and J. Kopp, "$\nu_\tau$ detection and the IDS-NF baseline." https://www.ids-nf.org/wiki/FrontPage/Documentation?action=AttachFile&do=get&target=IDS-NF-008-v1.0.pdf.

[55] P. Huber, M. Lindner, M. Rolinec, and W. Winter, "Optimization of a neutrino factory oscillation experiment," *Phys. Rev.* **D74** (2006) 073003, hep-ph/0606119.

[56] P. Huber and W. Winter, "Neutrino factories and the 'magic' baseline," *Phys. Rev.* **D68** (2003) 037301, hep-ph/0301257.

[57] J. Kopp, T. Ota, and W. Winter, "Neutrino factory optimization for non-standard interactions," *Phys. Rev.* **D78** (2008) 053007, 0804.2261.

[58] D. Meloni, "Solving the octant degeneracy with the Silver channel," *Phys. Lett.* **B664** (2008) 279–284, 0802.0086.

[59] A. Donini, E. Fernandez-Martinez, D. Meloni, and S. Rigolin, "nu/mu disappearance at the SPL, T2K-I, NOnuA and the neutrino factory," *Nucl. Phys.* **B743** (2006) 41–73, hep-ph/0512038.

[60] V. Barger, S. Geer, and K. Whisnant, "Neutral currents and tests of three-neutrino unitarity in long-baseline experiments," *New J. Phys.* **6** (2004) 135, hep-ph/0407140.

[61] A. Donini, K.-i. Fuki, J. Lopez-Pavon, D. Meloni, and O. Yasuda, "The discovery channel at the Neutrino Factory: $\nu_\mu \to \nu_\tau$ pointing to sterile neutrinos," *JHEP* **08** (2009) 041, 0812.3703.

[62] A. Bueno, M. Campanelli, and A. Rubbia, "Physics potential at a neutrino factory: Can we benefit from more than just detecting muons?," *Nucl. Phys.* **B589** (2000) 577–608, hep-ph/0005007.

[63] J. Tang and W. Winter, "Neutrino factory in stages: Low energy, high energy, off- axis," *Phys. Rev.* **D81** (2010) 033005, 0911.5052.

[64] R. Gandhi and W. Winter, "Physics with a very long neutrino factory baseline," *Phys. Rev.* **D75** (2007) 053002, hep-ph/0612158.

[65] P. Huber, M. Lindner, T. Schwetz, and W. Winter, "First hint for CP violation in neutrino oscillations from upcoming superbeam and reactor experiments," *JHEP* **11** (2009) 044, 0907.1896.

[66] N. C. Ribeiro, H. Minakata, H. Nunokawa, S. Uchinami, and R. Zukanovich-Funchal, "Probing Non-Standard Neutrino Interactions with Neutrino Factories," *JHEP* **12** (2007) 002, 0709.1980.

[67] A. Bross *et al.*, "The multi-channel low energy neutrino factory," 0911.3776.

[68] A. Cervera *et al.*, "Golden measurements at a neutrino factory," *Nucl. Phys.* **B579** (2000) 17–55, hep-ph/0002108.

[69] E. Fernández-Martínez, T. Li, O. Mena, and S. Pascoli. in preparation.

[70] C. Ankenbrandt *et al.*, "Low-energy neutrino factory design," *Phys. Rev. ST Accel. Beams* **12** (2009) 070101.

[71] J. N. Bahcall, M. Baldo-Ceolin, D. B. Cline, and C. Rubbia, "Predictions for a liquid argon solar neutrino detector," *Phys. Lett.* **B178** (1986) 324.

[72] B. Fleming. Private communication.

[73] V. Barger, P. Huber, D. Marfatia, and W. Winter, "Which long-baseline neutrino experiments are preferable?," *Phys. Rev.* **D76** (2007) 053005, hep-ph/0703029.

[74] P. Huber, M. Lindner, and W. Winter, "Simulation of long-baseline neutrino oscillation experiments with GLoBES," *Comput. Phys. Commun.* **167** (2005) 195, hep-ph/0407333.

[75] P. Huber, J. Kopp, M. Lindner, M. Rolinec, and W. Winter, "New features in the simulation of neutrino oscillation experiments with GLoBES 3.0," *Comput. Phys. Commun.* **177** (2007) 432–438, hep-ph/0701187.

[76] P. Zucchelli, "A novel concept for a anti-nu/e / nu/e neutrino factory: The beta beam," *Phys. Lett.* **B532** (2002) 166–172.

[77] J. Burguet-Castell, D. Casper, E. Couce, J. J. Gomez-Cadenas, and P. Hernandez, "Optimal beta-beam at the CERN-SPS," *Nucl. Phys.* **B725** (2005) 306–326, hep-ph/0503021.

[78] J. Burguet-Castell, D. Casper, J. J. Gomez-Cadenas, P. Hernandez, and F. Sanchez, "Neutrino oscillation physics with a higher gamma beta- beam," *Nucl. Phys.* **B695** (2004) 217–240, hep-ph/0312068.

[79] S. Choubey, P. Coloma, A. Donini, and E. Fernandez-Martinez, "Optimized Two-Baseline Beta-Beam Experiment," *JHEP* **12** (2009) 020, 0907.2379.

[80] Y. Itow *et al.*, "The JHF-Kamioka neutrino project," hep-ex/0106019.

[81] V. Barger *et al.*, "Report of the US long baseline neutrino experiment study," 0705.4396.

[82] A. M. Gago, H. Minakata, H. Nunokawa, S. Uchinami, and R. Zukanovich Funchal, "Resolving CP Violation by Standard and Nonstandard Interactions and Parameter Degeneracy in Neutrino Oscillations," *JHEP* **01** (2010) 049, 0904.3360.

[83] M. Blennow and E. Fernandez-Martinez, "Neutrino oscillation parameter sampling with MonteCUBES," *Comput. Phys. Commun.* **181** (2010) 227–231, 0903.3985.

[84] C. Biggio, M. Blennow, and E. Fernandez-Martinez, "General bounds on non-standard neutrino interactions," *JHEP* **08** (2009) 090, 0907.0097.

[85] J. Aysto *et al.*, "Physics with low-energy muons at a neutrino factory complex," hep-ph/0109217.

[86] M. B. Gavela, T. Hambye, D. Hernandez, and P. Hernandez, "Minimal Flavour Seesaw Models," *JHEP* **09** (2009) 038, 0906.1461.

[87] A. Abada, C. Biggio, F. Bonnet, M. B. Gavela, and T. Hambye, "$\mu \to e\gamma$ and $\tau \to l\gamma$ decays in the fermion triplet seesaw model," *Phys. Rev.* **D78** (2008) 033007, 0803.0481.

[88] A. De Gouvea, G. F. Giudice, A. Strumia, and K. Tobe, "Phenomenological implications of neutrinos in extra dimensions," *Nucl. Phys.* **B623** (2002) 395–420, hep-ph/0107156.

[89] A. de Gouvea, "GeV Seesaw, Accidentally Small Neutrino Masses, and Higgs Decays to Neutrinos," 0706.1732.

[90] G. Perez and L. Randall, "Natural Neutrino Masses and Mixings from Warped Geometry," *JHEP* **01** (2009) 077, 0805.4652.

[91] A. Azatov, M. Toharia, and L. Zhu, "Higgs Mediated FCNC's in Warped Extra Dimensions," *Phys. Rev.* **D80** (2009) 035016, 0906.1990.

[92] L. Calibbi, M. Frigerio, S. Lavignac, and A. Romanino, "Flavour violation in supersymmetric SO(10) unification with a type II seesaw mechanism," *JHEP* **12** (2009) 057, 0910.0377.

[93] S. Davidson, J. Garayoa, F. Palorini, and N. Rius, "CP Violation in the SUSY Seesaw: Leptogenesis and Low Energy," *JHEP* **09** (2008) 053, 0806.2832.

[94] M. Raidal *et al.*, "Flavour physics of leptons and dipole moments," *Eur. Phys. J.* **C57** (2008) 13–182, 0801.1826.

[95] W. Altmannshofer, A. J. Buras, S. Gori, P. Paradisi, and D. M. Straub, "Anatomy and Phenomenology of FCNC and CPV Effects in SUSY Theories," *Nucl. Phys.* **B830** (2010) 17–94, 0909.1333.

[96] L. Calibbi *et al.*, "FCNC and CP Violation Observables in a SU(3)-flavoured MSSM," *Nucl. Phys.* **B831** (2010) 26–71, 0907.4069.

[97] T. Fukuyama, H. Sugiyama, and K. Tsumura, "Constraints from muon g-2 and LFV processes in the Higgs Triplet Model," *JHEP* **03** (2010) 044, 0909.4943.

[98] S. Davidson, "CP violating phases in mu-e conversion," 0809.0263.

[99] S. Y. Ayazi and Y. Farzan, "A Window on the CP-violating Phases of MSSM from Lepton Flavor Violating Processes," *JHEP* **01** (2009) 022, 0810.4233.

[100] Y. Farzan, "Measuring CP-violating phases through studying the polarization of the final particles in $\mu \to eee$," *Phys. Lett.* **B677** (2009) 282–290, 0902.2445.

[101] Y. Farzan and S. Najjari, "Extracting the CP-violating phases of trilinear R-parity violating couplings from $\mu \to eee$," 1001.3207.

[102] V. Cirigliano, R. Kitano, Y. Okada, and P. Tuzon, "On the model discriminating power of mu -¿ e conversion in nuclei," *Phys. Rev.* **D80** (2009) 013002, 0904.0957.

[103] **MEG** Collaboration, J. Adam *et al.*, "A limit for the mu -¿ e gamma decay from the MEG experiment," 0908.2594.

[104] **Mu2e** Collaboration, R. M. Carey *et al.*, "Proposal to search for $\mu^- N \to e^- N$ with a single event sensitivity below $10^{-16}$,". FERMILAB-PROPOSAL-0973.

[105] **COMET** Collaboration, Y. G. Cui *et al.*, "Conceptual design report for experimental search for lepton flavor violating mu- - e- conversion at sensitivity of 10**(-16) with a slow-extracted bunched proton beam (COMET),". KEK-2009-10.

[106] A. de Gouvea, S. Lola, and K. Tobe, "Lepton flavor violation in supersymmetric models with trilinear R-parity violation," *Phys. Rev.* **D63** (2001) 035004, `hep-ph/0008085`.

[107] **BaBar** Collaboration, J. P. Lees *et al.*, "Limits on tau Lepton-Flavor Violating Decays in three charged leptons," `1002.4550`.

[108] **BELLE** Collaboration, Y. Miyazaki *et al.*, "Search for Lepton Flavor and Lepton Number Violating tau Decays into a Lepton and Two Charged Mesons," *Phys. Lett.* **B682** (2010) 355–362, `0908.3156`.

[109] **BABAR** Collaboration, B. Aubert *et al.*, "Improved limits on lepton flavor violating tau decays to l phi, l rho, l K* and l K*bar," *Phys. Rev. Lett.* **103** (2009) 021801, `0904.0339`.

[110] **BaBar** Collaboration, B. Aubert *et al.*, "Search for Lepton Flavour Violating Decays $\tau \to \ell K^0_S$ with the BaBar Experiment," *Phys. Rev.* **D79** (2009) 012004, `0812.3804`.

[111] **Belle** Collaboration, Y. Miyazaki *et al.*, "Search for Lepton-Flavor-Violating tau Decays into Lepton and f0(980) Meson," *Phys. Lett.* **B672** (2009) 317–322, `0810.3519`.

[112] **Belle** Collaboration, Y. Nishio *et al.*, "Search for lepton-flavor-violating $\tau \to \ell V^0$ decays at Belle," *Phys. Lett.* **B664** (2008) 35–40, `0801.2475`.

[113] P. Minkowski, "Mu → e gamma at a rate of one out of 1-billion muon decays?," *Phys. Lett.* **B67** (1977) 421.

[114] M. Gell-Mann, P. Ramond, and R. Slansky *Supergravity* (1979) 315. edited by F. Nieuwenhuizen and D. Friedman, North Holland, Amsterdam.

[115] T. Yanagida. Proceedings of the Workshop on Unified Theories and the Baryon Number of the Universe, edited by O. Sawada and A. Sugamoto, KEK, Japan 1979.

[116] R. N. Mohapatra and G. Senjanovic, "Neutrino masses and mixings in gauge models with spontaneous parity violation," *Phys. Rev.* **D23** (1981) 165.

[117] J. Lesgourgues and S. Pastor, "Massive neutrinos and cosmology," *Phys. Rept.* **429** (2006) 307–379, `astro-ph/0603494`.

[118] S. Hannestad, T. Haugboelle, and B. Thomsen, "Precision measurements of large scale structure with future type Ia supernova surveys," *JCAP* **0802** (2008) 022, `0705.0979`.

[119] S. M. Bilenky and S. T. Petcov, "On a Possible Suppression of the Parity Violation Effects in Heavy Atoms," *Sov. J. Nucl. Phys.* **25** (1977) 649.

[120] F. Borzumati and A. Masiero, "Large muon and electron number violations in supergravity theories," *Phys. Rev. Lett.* **57** (1986) 961.

[121] J. R. Ellis, J. Hisano, S. Lola, and M. Raidal, "CP violation in the minimal supersymmetric seesaw model," *Nucl. Phys.* **B621** (2002) 208–234, hep-ph/0109125.

[122] J. A. Casas and A. Ibarra, "Oscillating neutrinos and mu → e, gamma," *Nucl. Phys.* **B618** (2001) 171–204, hep-ph/0103065.

[123] M. Fukugita and T. Yanagida, "Baryogenesis without grand unification," *Phys. Lett.* **B174** (1986) 45.

[124] M. A. Luty, "Baryogenesis via leptogenesis," *Phys. Rev.* **D45** (1992) 455–465.

[125] M. Flanz, E. A. Paschos, and U. Sarkar, "Baryogenesis from a lepton asymmetric universe," *Phys. Lett.* **B345** (1995) 248–252, hep-ph/9411366.

[126] L. Covi, E. Roulet, and F. Vissani, "CP violating decays in leptogenesis scenarios," *Phys. Lett.* **B384** (1996) 169–174, hep-ph/9605319.

[127] A. Pilaftsis, "CP violation and baryogenesis due to heavy Majorana neutrinos," *Phys. Rev.* **D56** (1997) 5431–5451, hep-ph/9707235.

[128] W. Buchmuller and M. Plumacher, "CP asymmetry in Majorana neutrino decays," *Phys. Lett.* **B431** (1998) 354–362, hep-ph/9710460.

[129] A. Abada, S. Davidson, F.-X. Josse-Michaux, M. Losada, and A. Riotto, "Flavour Issues in Leptogenesis," *JCAP* **0604** (2006) 004, hep-ph/0601083.

[130] S. Pascoli, S. T. Petcov, and A. Riotto, "Connecting low energy leptonic CP-violation to leptogenesis," *Phys. Rev.* **D75** (2007) 083511, hep-ph/0609125.

[131] S. Pascoli, S. T. Petcov, and A. Riotto, "Leptogenesis and low energy CP violation in neutrino physics," *Nucl. Phys.* **B774** (2007) 1–52, hep-ph/0611338.

[132] **ISS Accelerator Working Group** Collaboration, J. S. Berg *et al.*, "Accelerator design concept for future neutrino facilities," *JINST* **4** (2009) P07001, 0802.4023.

[133] R. Garoby *et al.*, "Linac-based Proton Driver for a Neutrino Factory," 2009. CERN-NEUTRINO-FACTORY-NOTE-157.

[134] http://projectx.fnal.gov/.

[135] C. Prior *et al.*, "RAL Proton Driver Studies for a Neutrino Factory,". Proceedings of NUFACT00, Monterey, California, 2000.

[136] G. Rees, "An FFAG Proton Driver for a Neutrino Factory,". ICFA Beam Dynamics Newsletter 43, August 2007.

[137] E. Benedetto, "Beam stability in the SPL proton driver accumulator for a Neutrino Factory at CERN." To be published in the proceedings of the 11$^{\text{th}}$ International Workshop on Neutrino Factories, Superbeams and Beta Beams, July 20–25, 2009, Illinois Institute of Technology, Chicago.

[138] M. Aiba, "Feasibility Study of Accumulator and Compressor for the 6-bunches SPL based Proton Driver." CERN-AB-2008-060.

[139] J. Pasternak, "FEASIBILITY OF A COMMON PROTON DRIVER FOR A NEUTRON SPALLATION SOURCE AND A NEUTRINO FACTORY," *Proceedings of PAC09, Vancouver, BC, Canada* (2009). http://appora.fnal.gov/pls/pac09.

[140] A. Blondel (Ed. ) *et al.*, "ECFA/CERN studies of a European neutrino factory complex." CERN-2004-002.

[141] A. Perrin, "Travel user manual." Unpublished.

[142] M. BastaniNejad *et al.*, "Studies of Breakdown in a Pressurized RF Cavity,". EPAC'08, 11th European Particle Accelerator Conference, 23- 27 June 2008, Genoa, Italy.

[143] J. C. Gallardo and M. S. Zisman, "Thoughts on Incorporating HPRF in a Linear Cooling Channel," `0908.3152`.

[144] S. Bogacz *J. Phys. G: Nucl. Part. Phys.* **29** (2003) 1723.

[145] B. Autin *et al. J. Phys. G: Nucl. Part. Phys.* **29** (2003) 1637.

[146] J. Berg *Phys. Rev. ST Accel. Beams* **9** (2006) 011001.

[147] S. Bogacz *Nucl. Phys. B* **149** (2005) 309.

[148] S. Bogacz *Nucl. Phys. B* **155** (2006) 324.

[149] R. K. Cooper, "Release notes for POISSON / SUPERFISH 4.0,". LA-UR-92-3397.

[150] M. Menzel and H. Stokes, "User's Guide for the POISSON / SUPERFISH group of codes,". LA-UR-87-115.

[151] "Die Software f ur Multiphysik-Simulationen." http://www.ch.comsol.com/.

[152] "General Particle Tracer." http://www.pulsar.nl/gpt.

[153] H. Wiedemann, "Particle Accelerator Physics." Springer-Verlag, Berline, 1993.

[154] Y. Kuno *et al.*, "A feasibility study of a neutrino factory in Japan," *KEK report* (2001). `http://www-prism.kek.jp/nufactj/index.html`.

[155] Y. Mori, "FFAG accelerators and their applications,". Presented at European Particle Accelerator Conference (EPAC 06), Edinburgh, Scotland, 26-30 Jun 2006, paper TUXFI01.

[156] T. Nakamoto *et al.*, "Design of superconducting combined function magnets for the 50-GeV proton beam line for the J-PARC neutrino experiment," *IEEE Trans. Appl. Supercond.* **14** (2004) 616–619.

[157] H. Enge, "Deflecting magnets," 1967. Focussing of charged particles, Vol. 2, Academic Press, New York, London.

[158] J. Berg and S. Machida, "FFAG DESIGNS FOR THE INTERNATIONAL DESIGN STUDY FOR THE NEUTRINO FACTORY," *Proceedings of PAC09, Vancouver, BC, Canada* (2009). http://trshare.triumf.ca/ pac09proc/Proceedings/papers/tu1grc04.pdf.

[159] J. Pasternak *et al.*, "FEASIBILITY OF INJECTION/EXTRACTION SYSTEMS FOR MUON FFAG RINGS IN THE NEUTRINO FACTORY," *Proceedings of PAC09, Vancouver, BC, Canada* (2009). http://appora.fnal.gov/pls/pac09/JACoW.view_abstract?abs_id=3804.

[160] P. Brindza *et al.*, "Superconducting septum magnet design for Jefferson Lab Hall A," *IEEE Trans. Appl. Supercond.* **11** (1981) 1594–1596.

[161] F. Schmidt, "Mad-X a worthy successor for MAD8?," *Nucl. Instrum. Meth.* **A 558** (2006) 47.

[162] T. J. Roberts *et al.*, "G4Beamline Particle Tracking in Matter-dominated Beam Lines,". EPAC'08, 11th European Particle Accelerator Conference, 23- 27 June 2008, Genoa, Italy.

[163] F. Meot, "6-D beam dynamics simulations in FFAGs using the ray- tracing code Zgoubi," *ICFA Beam Dyn. Newslett.* **43** (2007) 44–50.

[164] Y. Hayato *et al.*, "Letter of Intent: Neutrino Oscillation Experiment at JHF," 2003.

[165] J. e. Morfin, "The Miner$\nu$a Technical Design Report," 2006.

[166] A. De Rujula, M. B. Gavela, and P. Hernandez, "Neutrino oscillation physics with a neutrino factory," *Nucl. Phys.* **B547** (1999) 21–38, `hep-ph/9811390`.

[167] B. Pontecorvo, "Mesonium and antimesonium," *Sov. Phys. JETP* **6** (1957) 429.

[168] B. Pontecorvo, "Inverse beta processes and nonconservation of lepton charge," *Sov. Phys. JETP* **7** (1958) 172–173.

[169] Z. Maki, M. Nakagawa, and S. Sakata, "Remarks on the unified model of elementary particles," *Prog. Theor. Phys.* **28** (1962) 870.

[170] "EUROnu: A High Intensity Neutrino Oscillation Facility in Europe."

[171] A. Cervera, F. Dydak, and J. Gomez Cadenas, "A large magnetic detector for the neutrino factory," *Nucl. Instrum. Meth.* **A451** (2000) 123–130.

[172] A. Cervera-Villanueva, "MIND performance and prototyping," *AIP Conf. Proc.* **981** (2008) 178–180.

[173] **MINOS** Collaboration, D. G. Michael *et al.*, "The magnetized steel and scintillator calorimeters of the MINOS experiment," *Nucl. Instrum. Meth. A* **596** (2008) 190.

[174] A. Cervera, A. Laing, J. Martin-Albo, and F. P. Soler, "Performance of the MIND detector at a Neutrino Factory using realistic muon reconstruction," 1004.0358.

[175] "Geant 3.21 CERN Program Library."

[176] A. Cervera and A. Laing, "Status of MIND," *PoS* **Nufact08** (2008) 042.

[177] A. M. Dziewonski and D. L. Anderson, "Preliminary reference earth model," *Phys. Earth Planet. Interiors* **25** (1981) 297–356.

[178] J. Burguet-Castell, M. B. Gavela, J. J. Gomez-Cadenas, P. Hernandez, and O. Mena, "Superbeams plus neutrino factory: The golden path to leptonic CP violation," *Nucl. Phys.* **B646** (2002) 301–320, hep-ph/0207080.

[179] V. Barger, D. Marfatia, and K. Whisnant, "Breaking eight-fold degeneracies in neutrino CP violation, mixing, and mass hierarchy," *Phys. Rev.* **D65** (2002) 073023, hep-ph/0112119.

[180] G. Ingelman, A. Edin, and J. Rathsman, "LEPTO 6.5 - A Monte Carlo generator for deep inelastic lepton-nucleon scattering," *Computer Physics Communications* **101** (1997) 108–134(27).

[181] A. Cervera-Villanueva, J. J. Gomez-Cadenas, and J. A. Hernando, "'RecPack' a reconstruction toolkit," *Nucl. Instrum. Meth.* **A534** (2004) 180–183.

[182] D. Emeliyanov, I. Gorbounov, and I. Kisel, "OTR/ITR-CATS: Tracking Based on Cellular Automaton and Kalman Filter," 2001. HERA-B note 01-137.

[183] P. Adamson *et al.*, "The MINOS calibration detector," *Nucl. Instrum. Meth.* **A556** (2006) 119–133.

[184] G. Bari *et al.*, "Analysis of the performance of the MONOLITH prototype," *Nucl. Instrum. Meth.* **A508** (2003) 170–174.

[185] R. Brun and F. Rademakers, "ROOT: An object oriented data analysis framework," *Nucl. Instrum. Meth.* **A389** (1997) 81–86.

[186] **MINOS** Collaboration, P. Adamson *et al.*, "A Study of Muon Neutrino Disappearance Using the Fermilab Main Injector Neutrino Beam," *Phys. Rev.* **D77** (2008) 072002, 0711.0769.

[187] **CHORUS** Collaboration, A. Kayis-Topaksu *et al.*, "Leading order analysis of neutrino induced dimuon events in the CHORUS experiment," *Nucl. Phys.* **B798** (2008) 1–16, 0804.1869.

[188] A. Donini, P. Huber, S. Pascoli, W. Winter, and O. Yasuda, "Physics and Performance Evaluation Group," *AIP Conf. Proc.* **981** (2008) 43–45, 0712.0909.

[189] **KamLAND** Collaboration, K. Eguchi *et al.*, "First results from KamLAND: Evidence for reactor anti- neutrino disappearance," *Phys. Rev. Lett.* **90** (2003) 021802, hep-ex/0212021.

[190] **NOvA** Collaboration, D. S. Ayres *et al.*, "NOvA proposal to build a 30-kiloton off-axis detector to study neutrino oscillations in the Fermilab NuMI beamline," hep-ex/0503053.

[191] J. Hylen *et al.*, "Conceptual design for the technical components of the neutrino beam for the main injector (NuMI),". FERMILAB-TM-2018.

[192] K. S. McFarland, "The MINERvA experiment at FNAL," *Eur. Phys. J.* **A24S2** (2005) 187.

[193] **D0** Collaboration, P. S. Baringer *et al.*, "Cosmic ray tests of the D0 preshower detector," *Nucl. Instrum. Meth.* **A469** (2001) 295–310, hep-ex/0007026.

[194] **VLHC Design Study Group** Collaboration, G. Ambrosio *et al.*, "Design study for a staged very large hadron collider,". SLAC-R-591.

[195] D. Casper, "The nuance neutrino physics simulation, and the future," *Nucl. Phys. Proc. Suppl.* **112** (2002) 161–170, hep-ph/0208030.

[196] **LAGUNA** Collaboration, D. Angus *et al.*, "The LAGUNA design study- towards giant liquid based underground detectors for neutrino physics and astrophysics and proton decay searches," 1001.0077.

[197] **ICARUS** Collaboration, S. Amerio *et al.*, "Design, construction and tests of the ICARUS T600 detector," *Nucl. Instrum. Meth.* **A527** (2004) 329–410.

[198] A. Badertscher *et al.*, "Construction and operation of a Double Phase LAr Large Electron Multiplier Time Projection Chamber," 0811.3384.

[199] A. Badertscher *et al.*, "Operation of a double-phase pure argon Large Electron Multiplier Time Projection Chamber: comparison of single and double phase operation," 0907.2944.

[200] T. Murayama, "LAr detector R&D in Japan." Talk given at the NNN09 workshop, Colorado (2009).

[201] A. Rubbia *et al.*, "Test beam exposure of a liquid argon TPC detector at the CERN SPS North Area (ePiLAr)." Abstract 82 submitted to the, New Opportunities in the Physics Lanscape workshop, CERN May 2009.

[202] E. Bechetoille and H. Mathez, "CMOS charge amplifier for liquid argon time projection chamber detectors." WOLTE 8, Workshop on low temeperature electronics, Jena (2008).

[203] P. K. Lightfoot, G. J. Barker, K. Mavrokoridis, Y. A. Ramachers, and N. J. C. Spooner, "Characterisation of a silicon photomultiplier device for applications in liquid argon based neutrino physics and dark matter searches," *JINST* **3** (2008) P10001, 0807.3220.

[204] P. K. Lightfoot, G. J. Barker, K. Mavrokoridis, Y. A. Ramachers, and N. J. C. Spooner, "Optical readout tracking detector concept using secondary scintillation from liquid argon generated by a thick gas electron multiplier," *JINST* **4** (2009) P04002, 0812.2123.

[205] **The ArDM** Collaboration, V. Boccone *et al.*, "Development of wavelength shifter coated reflectors for the ArDM argon dark matter detector," *JINST* **4** (2009) P06001, 0904.0246.

[206] A. Badertscher, M. Laffranchi, A. Meregaglia, A. Muller, and A. Rubbia, "First results from a liquid argon time projection chamber in a magnetic field," *Nucl. Instrum. Meth.* **A555** (2005) 294–309, physics/0505151.

[207] A. Ereditato and A. Rubbia, "Conceptual design of a scalable multi-kton superconducting magnetized liquid argon TPC," *Nucl. Phys. Proc. Suppl.* **155** (2006) 233–236, hep-ph/0510131.

[208] B. Morgan, "Preliminary studies of liquid argon simulation and reconstruction." Talk given at the fourth plenary meeting of IDS-NF, Mumbai (2009).

[209] A. Marchionni, "LAr detector R&D in Europe." Talk given at the NNN09 workshop, Colorado (2009).

[210] R. Andrews *et al.*, "A system to test the effects of materials on the electron drift lifetime in liquid argon and observations on the effect of water," *Nucl. Instrum. Meth.* **A608** (2009) 251–258.

[211] A. Curioni *et al.*, "A Regenerable Filter for Liquid Argon Purification," *Nucl. Instrum. Meth.* **A605** (2009) 306–311, 0903.2066.

[212] **ArgoNeuT** Collaboration, J. Spitz, "ArgoNeuT, a liquid argon time projection chamber in a low energy neutrino beam," *J. Phys. Conf. Ser.* **203** (2010) 012108, 0910.2650.

[213] **MicroBooNE** Collaboration, M. Soderberg, "MicroBooNE: A New Liquid Argon Time Projection Chamber Experiment," *AIP Conf. Proc.* **1189** (2009) 83–87, 0910.3497.

[214] **LBNE DUSEL** Collaboration, J. Maricic, "The Long Baseline Neutrino Oscillation Experiment at DUSEL," *J. Phys. Conf. Ser.* **203** (2010) 012109.

[215] J. Tang and W. Winter, "On near detectors at a neutrino factory," *Phys. Rev.* **D80** (2009) 053001.

[216] **GENIE** Collaboration, "GENIE web site." http://www.genie-mc.org.

[217] **GENIE** Collaboration, C. Andreopoulos *et al.*, "The GENIE Neutrino Monte Carlo Generator." arXiv:0905.2517v1.

[218] **CHARM II** Collaboration, P. Vilain *et al. Phys. Lett.* **B 364** (1995) 121.

[219] S. Mishra *et al. Phys. Lett.* **B 252** (1990) 170.

[220] Y. Karadzhov. Poster No. 56 at NuFact09, Chicago, July 20-25, 2009.